Performance and thermal-vacuum testing of terrestrial cameras in pocketqubes

R.J. Meesen

Delft University of Technology

Performance and thermal-vacuum testing of terrestrial cameras in pocketqubes

by

R.J. Meesen

to obtain the degree of Master of Science
at the Delft University of Technology.

Student number	4136349		
Thesis Defense	09-01-2020		
Thesis committee:	Prof. E.K.A. Gill,	TU Delft	Space Systems Engineering
	Ir. J. Bouwmeester,	TU Delft	Space Systems Engineering
	Dr. D.M. Stam,	TU Delft	Astrodynamics and Space Missions
	M.Ş. Uludağ	TU Delft	Space Systems Engineering

Abstract

Due to their low mass pocketqubes are relatively inexpensive to launch. This makes them ideal for the creation of large constellations in low Earth orbit and a sufficiently large constellation would be able to perform measurements over the same area multiple times per day. Equipping these pocketqubes with cameras would increase the chance of cloud free images and would allow scientists to study dynamic processes which happen on sub-daily timescales. A camera in a pocketqube would have a spatial resolution of about 40 meters which would be sufficient for, for example, ocean color measurements or measuring land related variables, such as vegetation extent or land use, which allows biologists to better study conservation efforts. The economics of pocketqubes requires that the development cost and production cost per pocketqube must be comparable to the launch cost. For this reason it is preferable to use commercial off the shelf over purpose built cameras.

To test whether or not those commercial off the shelf cameras would survive in space, environmental testing is required. The launch environment, consisting of the accelerations and vibrations experienced during launch, and the thermal-vacuum environment potentially have the largest immediate impact on a camera and should be tested for. Other environmental effects in low Earth orbit, such as atomic oxygen, UV radiation, ionizing radiation, et cetera, are damaging over time but might only require analysis rather than extensive testing. Due to limited resources only a thermal-vacuum test was conducted. For this test two cameras, the See3CAM_CU30 and a generic ELP H264 720p usb camera, were selected. These cameras were subjected to a thermal-vacuum test by placing the cameras inside a vacuum-oven in which the cameras were exposed to a vacuum while being heated to a temperature of $50°C$. Because the vacuum-oven was not suitable to test the cameras at temperature below room temperature a thermal-ambient test was also conducted in which the cameras experienced four cycles of heating up and cooling down to the expected in-orbit temperature extremes of $50°C$ and $-5°C$ respectively. Before, in between, and after the thermal-ambient and thermal-vacuum tests a performance test was conducted to identify changes to the cameras. These performance tests measured the modulation transfer function, change in color representation, change in full well capacity, change in average dark signal, change in chromatic aberrations, and change in image distortion.

Both cameras still functioned after the thermal-ambient and thermal-vacuum tests and showed no significant outgassing. Both cameras also showed no change in the distortion and chromatic aberration after the conducted tests indicating that the lenses survived the thermal-vacuum environment without detectable changes. After the thermal-ambient test, conducted prior to the thermal-vacuum test, only the See3CAM_CU30 showed some minor changes in its color representation. The ELP camera was unaffected. After the thermal-vacuum test the See3CAM_CU30 only showed again some minor changes in the color representation. The ELP camera became unusable. It experienced a large change in color representation and showed significant performance deterioration in the full well capacity and average dark signal. This indicates the camera overexposing all its images. However, a test measuring the effective integration time at various camera settings before and after the experiments showed that the camera integration time is unlikely to have been affected.

Both cameras still functioned after the thermal-vacuum experiments. However, the fact that the ELP camera, and to a lesser extent the See3CAM_CU30, experienced performance degradation shows the necessity for good and rigorous performance testing of commercial off the shelf cameras before using them in pocketqubes. Although the See3CAM_CU30 showed potential it is too early to conclude whether or not it can survive in space for any length of time. In order to determine this at least a test is required demonstrating its ability to survive the mechanical environment experienced during launch.

Preface

This thesis documents the results of my research into the use of cameras in pocketqubes. The basis of this research is found in thinking about what kinds of commercial off the shelf payloads would be useful in pocketqubes. Because investigating many different types of payloads would be too broad and impractical, I narrowed this down to cameras during my literature research. My original intention was to conduct at least a vibration test and thermal-vacuum test on multiple cameras. However, arranging the vibration test proved not possible within the given time leaving only the thermal-vacuum test. This makes my conclusion not very conclusive on the question whether or not the cameras would actually survive. However, in terms of project duration this was probably better because it took considerably longer to develop a rigorous performance test than initially anticipated. Even though in my original planning I had already doubled the time I expected to need for that. Conducting this research was an interesting and valuable learning experience. I had fun fully designing and conducting practical experiments.

Finally, I would be remiss if I missed this opportunity to thank a couple of people. I would like to thank Jasper for his guidance and supervision. Thank you for the opportunity to conduct this research and for the advice and support throughout the entire project. I would also like to thank Şevket for helping me prepare the thermal-vacuum experiments. I would like to thank Erik, Harriët, Peter, and Willem for their insightful feedback on both the style and substance of this thesis. Finally, I would like to thank my friends and family for their support, creative ideas, solicited and unsolicited advice, and for helping me keep motivated to finish my thesis. Thank you all!

R.J. Meesen
Delft, December 2019

Cover image: The Netherlands as seen from the ISS (image source: [1])

Contents

List of symbols **vi**

List of abbreviations **vii**

1 Introduction **1**
1.1 Background . . . 1
1.2 Objective and scope . . . 3
1.3 Organization . . . 4

2 Operational context **5**
2.1 Pocketqubes . . . 5
2.2 The launch environment . . . 7
2.2.1 Accelerations . . . 7
2.2.2 Vibrations . . . 8
2.2.3 Shocks . . . 10
2.2.4 Aerothermal flux . . . 11
2.3 The low Earth orbit environment . . . 11
2.3.1 Thermal-vacuum . . . 11
2.3.2 Ionizing radiation . . . 11
2.3.3 Micro meteorites and other debris . . . 12
2.4 Experiment selection . . . 12
2.4.1 Functional and performance test . . . 14
2.4.2 Physical properties . . . 14
2.4.3 Thermal testing . . . 14
2.5 Discussion . . . 15

3 Commercial off the shelf cameras **16**
3.1 Available board level camera modules . . . 16
3.2 Available lenses . . . 19
3.3 COTS camera evaluation and selection . . . 19
3.3.1 Spatial resolution . . . 20
3.3.2 Signal to noise ratio . . . 21
3.3.3 Camera selection . . . 23
3.4 Discussion . . . 25

4 Camera performance metrics **26**
4.1 Modulation transfer function . . . 27
4.2 Color distance . . . 28
4.3 Signal to noise ratio . . . 29
4.4 Full well capacity . . . 29
4.5 Average dark signal . . . 29
4.6 Chromatic aberration . . . 29
4.7 Distortion . . . 30
4.8 Discussion . . . 31

5 Materials and method **32**
5.1 Integration time characterization . . . 33
5.2 Power . . . 33
5.3 Performance testing . . . 34
5.3.1 Setup . . . 34
5.3.2 Data gathering and analysis . . . 35

5.4 Thermal-ambient experiment . . . 37
5.4.1 Setup . . . 37
5.4.2 Data gathering and analysis . . . 38
5.5 Thermal-vacuum experiment . . . 38
5.5.1 Setup . . . 38
5.5.2 Data gathering and analysis . . . 40
5.6 Additional average dark signal measurement . . . 40
5.7 Discussion . . . 40

6 Results **42**
6.1 Power and integration time characterization . . . 42
6.2 Performance test I . . . 45
6.3 Thermal-ambient experiment . . . 47
6.4 Performance test II . . . 49
6.5 Thermal-vacuum experiment . . . 49
6.6 Additional measurement of average dark signal . . . 51
6.7 Performance test III . . . 51
6.8 Discussion . . . 56

7 Conclusion and future work **58**

Bibliography **61**

A Signal to noise ratio calculation **64**

B Color distance calculation **66**

C Temperature measurements **68**

D Performance test setup verification **70**
D.1 Image processing. . . . 70
D.2 Consistency. . . . 71
D.3 MTF Mapper verification . . . 76

E Supplementary figures **78**

List of symbols

α	Albedo
η	Quantum efficiency
λ	Wavelength
μ	Mean value
σ	Standard deviation
τ	Optical transmissivity
Ω	Solid angle

$\Delta C'$	Change in chroma
D	Aperture
$D_d ist$	Distortion
d	Pixel pitch
d_a	Undistorted distance center-corner
d_p	Distorted distance center-corner
ΔE_{2000}	Distance in HCL color space
E_f	Energy per photon
f	Focal length
$F\#$	F-number
fps_e	Effective framerate
H	Altitude
$\Delta H'$	Change in Hue
K_C	Chroma parametric factor
K_H	Hue parametric factor
K_L	Luminance parametric factor
$\Delta \ell$	Rayleigh criterion
$\Delta L'$	Change in luminance
L_{target}	Power of Lambertian radiator
R_T	Hue-chroma interaction factor
S	Signal
S_C	Chroma-difference dependent function
S_H	Hue-difference dependent function
S_L	Lightness-difference dependent function
t	Time
t_i	Integration time

List of abbreviations

ADCS	Attitude determination and control system
CA	Chromatic aberration
COMM	Communication system
COTS	Commercial off the shelf
CSI	Camera serial interface
DIY	Do it yourself
ECSS	European cooperation for space standardization
EM	Electromagnetic (radiation)
EPS	Electrical power system
ESF	Edge spread function
fps	Frames per second
FWC	Full well capacity
GNSS	Global navigation satellite system
GSD	Ground sampling distance
HCL	Hue, chroma, luminance
IC	Infinite conjugate
IR	Infrared
LEO	Low Earth orbit
LSF	Line spread function
MTF	Modulation transfer function
NTC	Negative temperature coefficient
OBC	On-board computer and data handling system
PC	Polycarbonate
pcb	Printed circuit board
PLA	Polyactic acid
PSD	Power spectral density
PT	Performance test
ROI	Region of interest
SEB	Single event burnout
SEE	Single event effect
SEL	Single event latch-up
SEU	Single event upset
SNR	Signal to noise ratio
SSO	Sun-synchronous orbit
TDI	Time delayed integration
TC	Telecommand
TML	Total mass loss
UHF	Ultra high frequency (0.3-3 GHz)
VHF	Very high frequency (30-300 MHz)

1

Introduction

Ever since the first image was taken from outside our atmosphere on October 24, 1946 by a modified V-2 rocket [2], pictures taken of the Earth from space have been a staple of spaceflight. Images such as the Pale Blue Dot or just simple images of our oceans, lands, and cities inspire as well as provide valuable data to students, scientists, and anyone who is interested. Although such pictures have been around for over 70 years there is still research to be done in the field of optical Earth observation. This thesis dives into that topic and investigates the use of commercial off the shelf cameras, initially designed for applications here on Earth, in combination with the new pocketqube satellite platform.

1.1. Background

Since their introduction in 1999 cubesats have matured from a new concept being primarily developed by universities to an established platform that is being embraced by major space agencies as well as companies seeking affordable access to space. There are well over a thousand cubesats currently in orbit performing a plethora of tasks, some individually and others as part of large constellations [3]. The NASA even brought cubesats on interplanetary missions [4]. One of the major advantages of cubesats compared to more traditional satellites is that they are relatively inexpensive to launch. This makes them interesting for companies and universities looking to develop their own satellite or constellation. The cubesat platform is a successful example of the effort to miniaturize and standardize spacecraft and their components. The Delft University of Technology is, together with and alongside other organizations, pursuing the next step in this ongoing miniaturization process in the form of pocketqubes. A new satellite platform with units eight times smaller than a cubesat unit [5].

Similar to a cubesat a pocketqube consists of small units, indicated with the suffix p, where the outer dimensions of a single unit measure 50x50x50 mm. Because of the deployment mechanism the 2p and 3p units are slightly larger with outer dimensions of 50x50x114 mm and 50x50x178 mm respectively [6]. Because volume is at a premium inside pocketqubes, payloads would have to be small. Preferably the volume of a payload would already be small enough to fit inside a pocketqube. Downsizing an instrument to fit within the constrained volume might be possible but would not always make economic sense [7]. With the current state of technology the utility of a single pocketqube is less than that of a single cubesat. Because of this, pocketqubes are only a reasonable option when the total cost of development, production, and operation is comparable to the launch cost. That is, if the cost of development, production, and operation is much greater than the cost to launch, it might be better to develop a slightly larger spacecraft which would have a higher utility increasing the utility per cost. An effective way to bring down development cost is to produce a large quantity of identical satellites which would lower the development cost per satellite significantly. Similarly, in a constellation the production cost per pocketqube can be reduced by using components that are very easy to integrate. Ideally these would be commercial off the shelf components which can simply be mounted in place and plugged into the rest of the systems without any additional modifications [8].

One of the possible application fields of the pocketqube is in Earth observation. Earth observation is one of the most common applications of satellites and a vast number of satellites is currently measuring a plethora of parameters about Earth. Pocketqubes can add to this already existing network by enabling measurements with a very high temporal resolution [8]. Because of their small size, pocketqubes can only supply a very limited amount of power to its payload. Passive payloads are therefore currently the only realistic option. Even considering the small volume available for payloads, there still is variety in possible passive payloads. These include optical cameras, uncooled micro-bolometers, GNSS receivers, magnetometers, accelerometers, and radiation detectors. The feasibility and scientific return of each of those types of payloads depend on the current state of technology for that payload and whether or not the scientific return of the type of measurements they perform can benefit from short revisit times.

Optical cameras are a very common type of payload due to their wide range of uses. Due to the diffraction limit the performance cameras can achieve in pocketqubes is fundamentally lower than what can be achieved with cubesats or larger satellites. A constellation of pocketqubes equipped with optical cameras should therefore not compete with the existing array of cameras but, instead, should complement it. Pocketqubes would be particularly suited for applications which require a very high temporal resolution with only modest spatial resolution requirements [8]. A good and relevant example of where there is a need for such a system is in biodiversity monitoring.

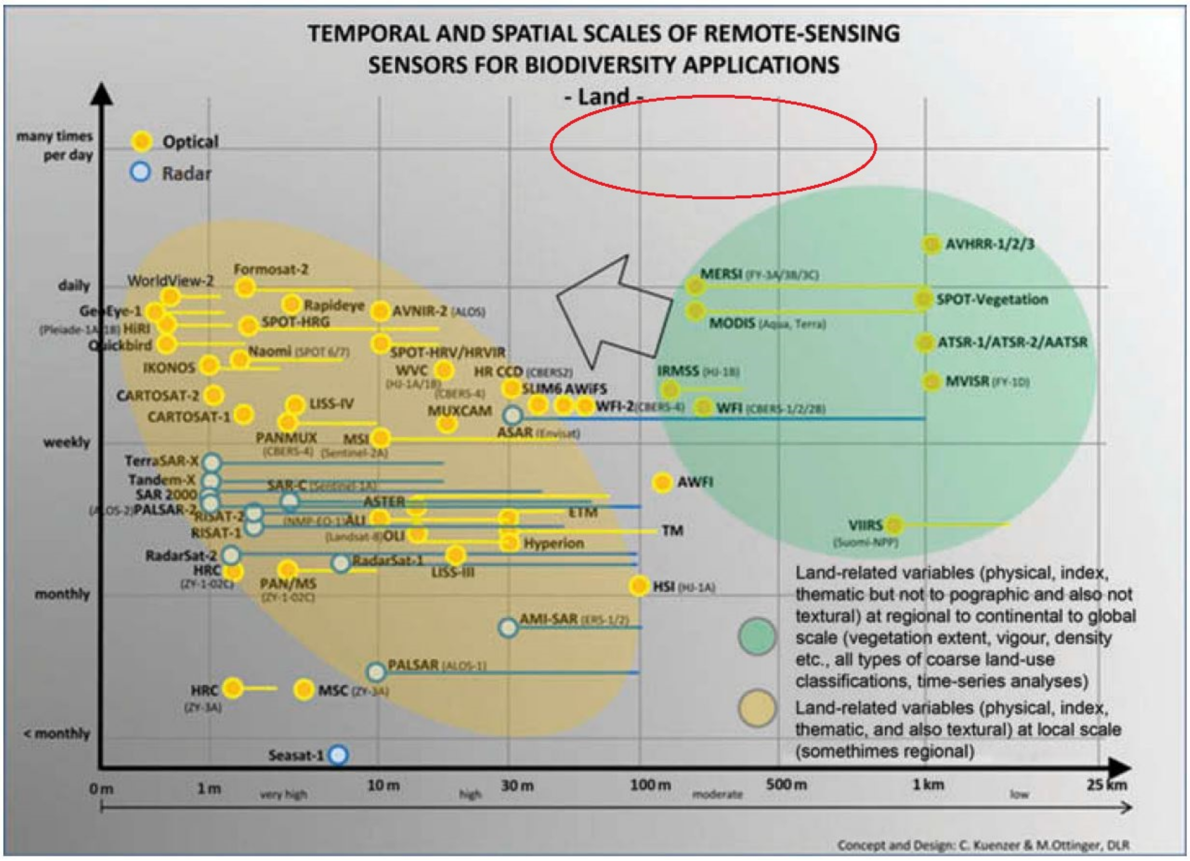

Figure 1.1: Optical/infrared (yellow) and radar (blue) sensors in orbit in 2014. The arrow indicates where [9] identified a useful combination of spatial (X-axis) and temporal (Y-axis) resolutions for new sensors. The red circle identifies the regime in which a constellation of pocketqubes equipped with optical sensors could potentially operate. (Image source: [9])

Figure 1.1 shows radar and optical sensors that can be used for land related biodiversity monitoring applications. The green ellipse indicates satellites that provide low spatial resolution global coverage which can be used for mapping large scale animal habitat boundaries using indicators such as land use, proximity to urban areas or infrastructure et cetera. The yellow ellipse indicates sensors with a high enough spatial resolution that it can allow for the indirect identification of species within those habitats based on, for example, vegetation specification. The arrow indicates an identified need for daily global coverage with higher spatial resolutions [9]. In Figure 1.1 (and Figure 1.2) the constellation of cubesats fielded by Planet which provides daily global coverage is not yet included. This constellation already fills some of the needs identified in Figure 1.1. However, a constellation of pocketqubes with an even higher temporal resolution would both increase the chance of cloud-free images and could prove useful in the analysis of processes which could occur within a single day. This is also true for ocean and waterbody applications shown in Figure 1.2. High temporal resolutions allow for the analysis of highly dynamic processes caused by, for example, tidal circulation, pollution, or severe storms [10].

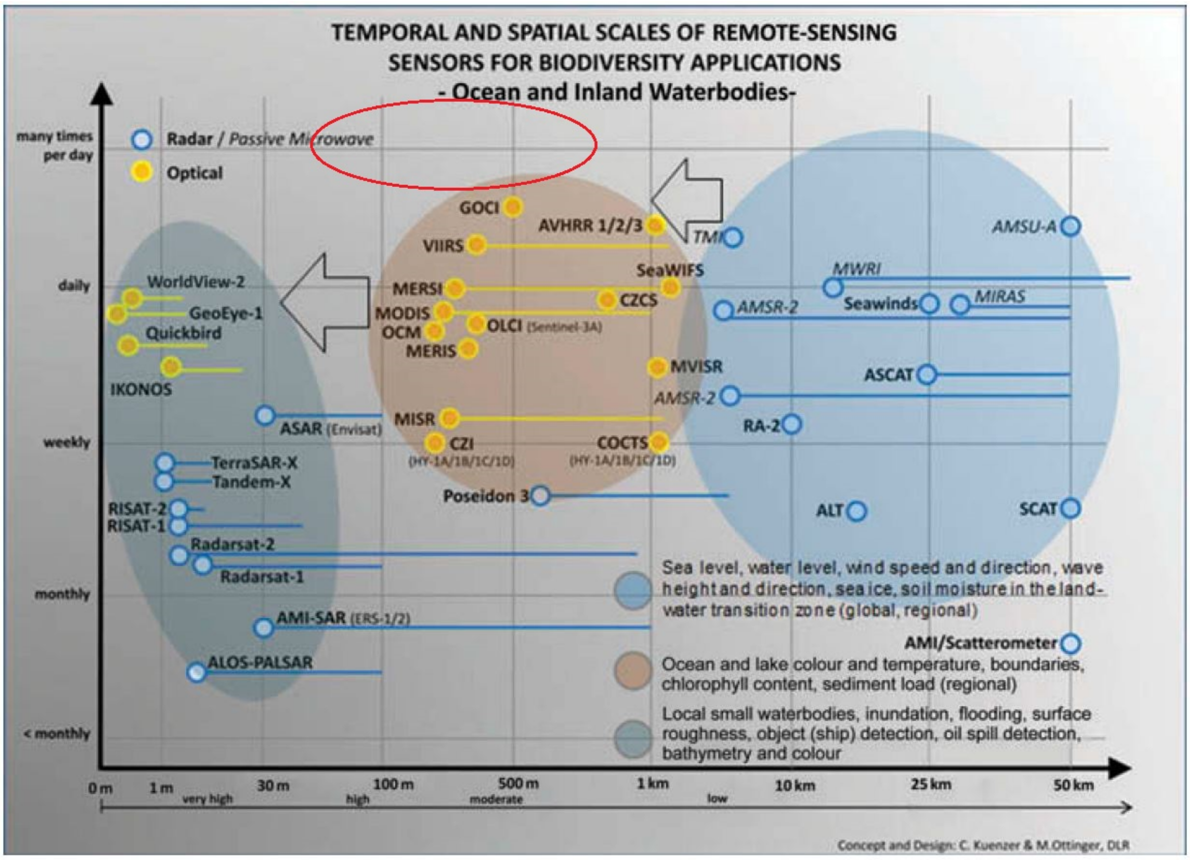

Figure 1.2: Optical/infrared (yellow) and radar (blue) sensors in orbit in 2014 which are useful for different applications depending on their spatial and temporal resolution as well as whether or not they provide global coverage. The arrows indicate identified gaps in the current network. The red circle indicates the combination of spatial and temporal resolution that can be reasonably achieved by pocketqubes. (Image source: [9])

1.2. Objective and scope

Commercial off the shelf cameras have been a relatively common payload for cubesats for some time. However, these commercial off the shelf cameras usually are either designed for space cameras, such as the SCS Gecko Imager on-board the nSight-1 [11] [12], or commercial off the shelf camera components integrated into a payload, such as with the CUMULOS payload [13]. This thesis will focus on existing 'plug and play' commercial off the shelf cameras that were designed for terrestrial applications.

During the literature study, which was conducted prior to this thesis and is summarized in Section 1.1, it was determined that commercial off the shelf camera can contribute useful new data to the scientific community provided that they are inexpensive, easy to integrate, and can survive the space and launch environment. The next in this investigation forms the objective of this thesis and is to determine whether or not they can survive the space environment. To answer this the following research question has been formulated.

R1 Can commercial off the shelf cameras, that are fit for use in pocketqubes, survive the space environment?

In order to answer this question the following sub-questions have been formulated. Based on the answers it should be possible to answer the research question.

R1.1 Which of the environmental conditions that a commercial off the shelf camera would experience can damage the camera?

R1.2 With which metrics can the effects of the environmental tests on the cameras be quantified?

R1.3 What are the effects of the environmental tests on the selected cameras?

1.3. Organization

In the literature study, summarized in Section 1.1, it was found that cameras would be useful payloads for a constellation of pocketqubes which has a high temporal resolution. Economically these cameras are preferred to be both commercial off the shelf and easy to integrate. This thesis builds on that by investigating the operational context of these cameras. **Chapter 2** details how such a camera will interact with the pocketqube as well as how it can be influenced by its environment in space and during launch. Based on these environmental considerations and on what was achievable a list of experiments was selected. The key experiment that was selected is a thermal-vacuum experiment. In **Chapter 3** a rationale is given for selecting the cameras for experimentation. From a list of currently available commercial off the shelf cameras two were selected based on a first order analysis. In order to determine the effects of the experiments on the cameras certain metrics must be measured. **Chapter 4** describes which metrics have been used based on relevance and feasibility. The tools necessary to measure these metrics were, out of necessity, build from the ground up. **Chapter 5** describes how those tools work as well as the setup of the experiments that were performed. The results of the experiments are discussed in **Chapter 6**. These results demonstrate that not every camera will be able to survive in space. However, the results also demonstrate that there is reason to believe that there are cameras that will. These conclusions are elaborated upon in the conclusion presented in **Chapter 7**. The conclusion also contains suggestions for further research into the topics.

2

Operational context

A satellite in orbit, and by extension its payload, always operates within a larger context. In Section 2.1 some details about the Delfi-PQ are given as well as how a camera would function within this system. The external operational context is primarily governed by the environmental conditions. These conditions are unlike typical operating conditions for cameras on Earth. In order to determine the tests required for qualifying the selected cameras for space applications it is important to understand the conditions the cameras will be subjected to. The most extreme environmental conditions take place in two important phases of the satellite's life: Launch and operation in space. The conditions that need to be considered are first discussed in Section 2.2 which deals with the launch environment and in Section 2.3 which details the space environment. In Section 2.4 a number of tests are proposed for this thesis taking into account some practical considerations. Finally, in Section 2.5 the results of this chapter are discussed.

2.1. Pocketqubes

The Delft University of Technology is currently developing its own pocketqube called the Delfi-PQ. The goal of this project is to further develop the new standard for pocketqubes and allow students experience with the development of (sub)systems for the satellite [6]. The 3p Delfi-PQ intends to have an integrated 1p bus, a 1p attitude determination and control (ADCS) and propulsion system, and a 1p payload. In the 3p configuration the external dimensions of the pocketqube are 50x50x178 mm attached to a 56x192 mm backplate. This backplate is part of the deployment mechanism by allowing the pocketqube to slide out of the launch pod in a controlled way [6]. Figure 2.1 shows the design of the outer shell of the Delfi-PQ.

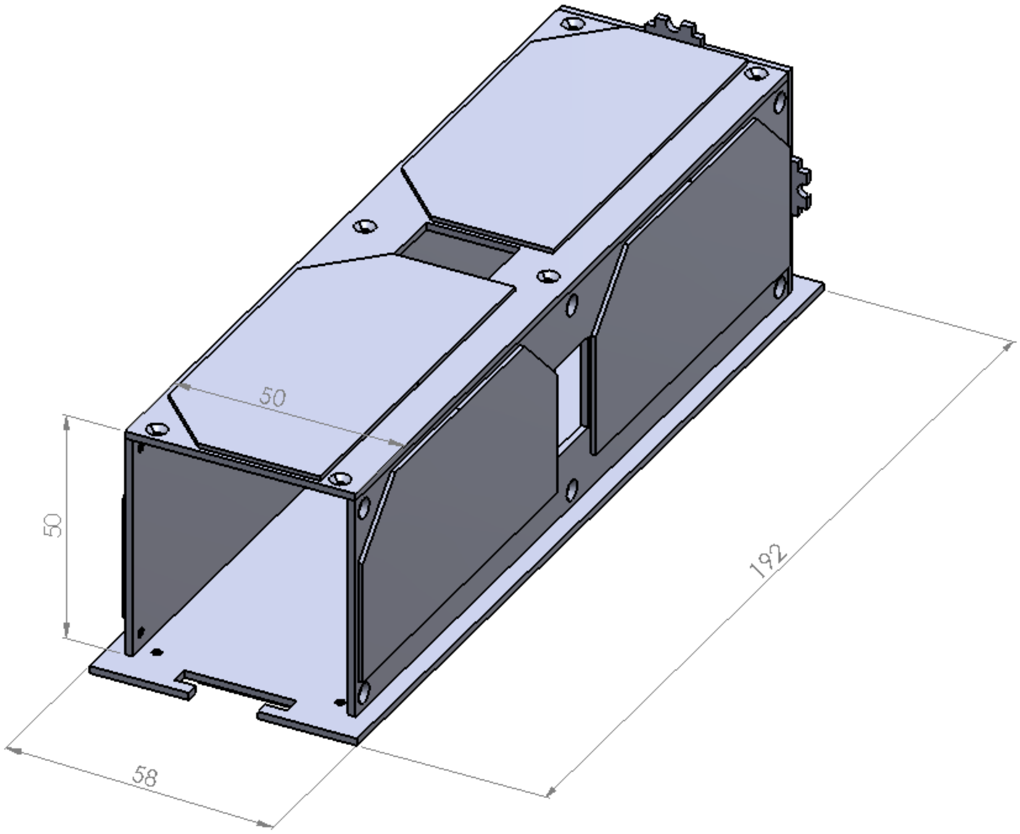

Figure 2.1: Delfi-PQ with outer dimensions in mm.

For the Delfi-PQ the outer area is covered in solar panels to provide power. The thickness of the panels, together with the printed circuit board to which they are attached, leaves an internal cross-sectional area of about 42x42 mm [6]. The solar panels provide an average power of about 1 W over a single orbit. The electrical power system (EPS) also contains lithium-ion batteries for power storage [14].

Communication is handled by the communication subsystem (COMM) which utilizes UHF for downlink and VHF for uplink with data rates up to 300 kbit/s [6] [15]. Whether this data rate is sufficient depends somewhat on the application and mission camera duty cycle as well as the used compression techniques. Compression ratios of 10:1 or even higher should be possible without any real image quality loss [16]. For example, a single image of 1280x720 pixels with a bit depth of 10 bits per color channel per pixel and a compression ratio of 10:1 would take 3 seconds to transmit at 300 kbit/s. For a first demonstration of the use of such cameras in combination with pocketqube this is sufficient. For larger constellations dealing with a lot more data the data rate should increase. This is something that should be achievable when the pocketqube platform matures and technological development allows for better attitude control and directional antennas.

An optical payload inside a pocketqube would interact, either directly or indirectly, with other systems inside the pocketqube. Most notably it would receive power from the electrical power system, receive instructions from and provide data to the on-board computer (OBC), and transmit data to Earth via the communications system. This is illustrated in Figure 2.2.

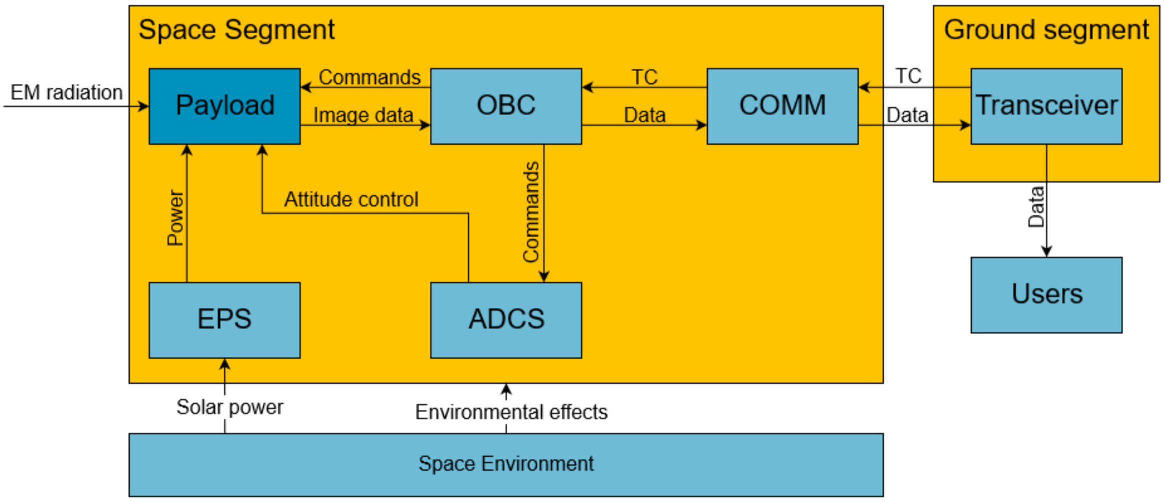

Figure 2.2: Payload interfaces within an operational context.

2.2. The launch environment

During launch a satellite experiences strong accelerations, vibrations, and shocks in both longitudinal and lateral directions. How strong these mechanical forces are depends on the used launch vehicle. In order to get an overview of some typical figures the environmental conditions of the Electron, Vega, Falcon 9, and Soyuz ST during launch are compared. The first two have been used to, or are scheduled to launch pocketqubes [3]. Table 2.1 shows some basic information about the rockets and shows that they span the full range of relatively small to massive launch systems. Since pocketqubes might commonly be launched by piggybacking off of different launches it is not inconceivable that they will be launched using rather heavy launch vehicles.

Table 2.1: Basic information about the Electron, Vega, Soyuz ST, and Falcon 9 launch systems [17][18][19][20].

	Electron	**Vega**	**Soyuz ST**	**Falcon 9**
Manufacturer	Rocket Lab	Avio	TsSKB-Progress	SpaceX
Mass [kg]	13000	137000	312000	330400
Length [m]	17	30	46.3	55
Payload to SSO (400 km) [kg]	168	1450	4900	7949
Stages	3 or 4	4	2 or 3	2

2.2.1. Accelerations

During launch a payload experiences accelerations that can be both quasi static and dynamic. The combinations between the two that form the maximum accelerations in any given direction form the limit loads. For the Electron, Vega, Soyuz ST, and Falcon 9 these are illustrated in Figure 2.3.

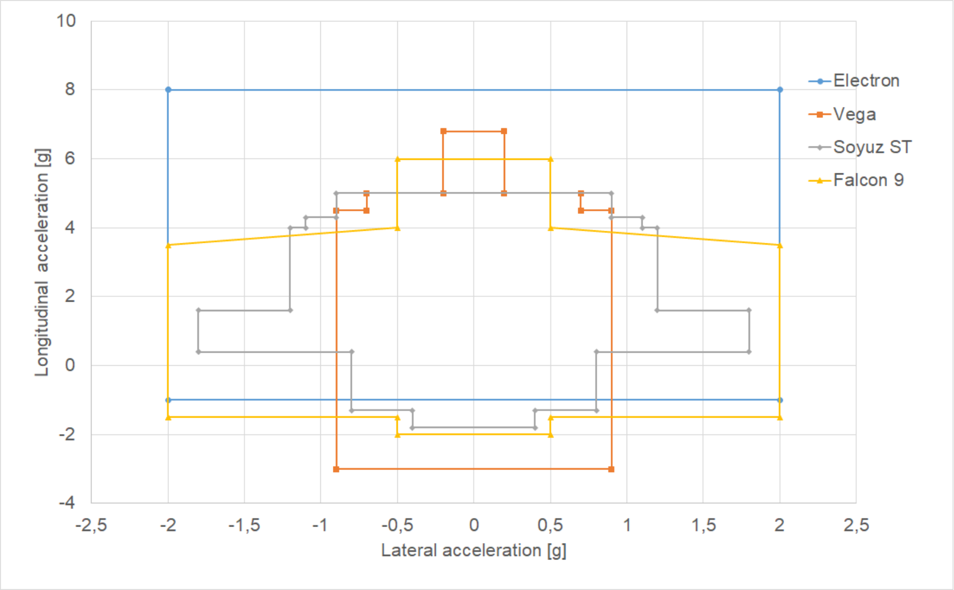

Figure 2.3: Limit loads for the Electron, Vega, Soyuz ST and Falcon 9 launchers (Positive loads are compressive) [17][18][19][20].

The limit loads within the figure form an envelope within which all the accelerations will fall. The payload's survivability of these accelerations can be experimentally demonstrated using an acceleration test [21].

2.2.2. Vibrations

The vibrations experienced during launch come in three forms and together form the most destructive aspect of the mechanical launch environment.

During lift-off the exhaust plume interacts with the pad creating strong acoustic vibrations. This decreases during the ascent. The unsteady flow around the launcher is also a significant contributor to acoustic vibrations. This type of vibration reaches a peak during transonic flight [20][22]. Figure 2.4 show the acoustic profiles of the four launch vehicles.Acoustic testing is mostly relevant for parts with large surface areas [21].

An acoustic test is done by subjecting the part to the expected acoustic sound pressure levels. To determine if significant changes in the resonant frequencies of the part happened during the test the results from pre-test and post-test measurements are compared.

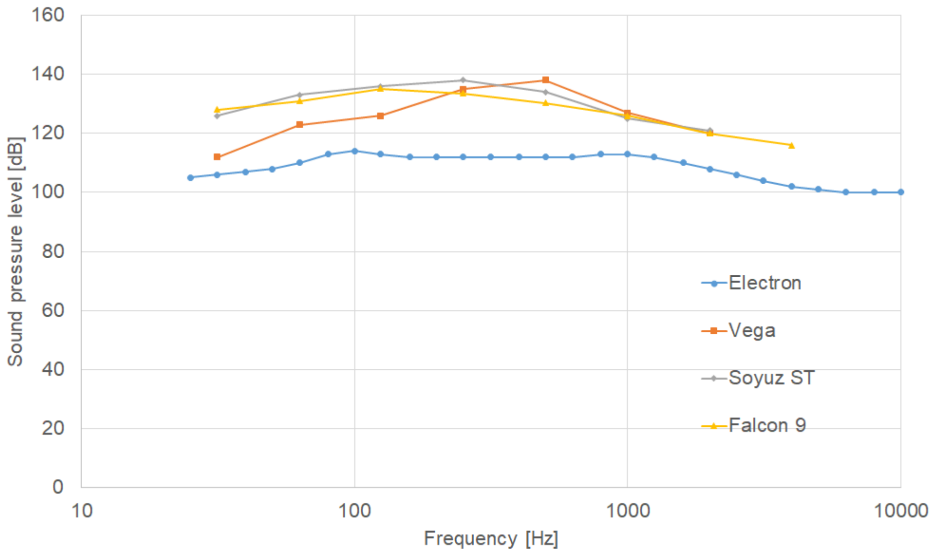

Figure 2.4: Acoustic noise spectrum of the Electron, Vega, Soyuz ST, and Falcon 9 [17][18][19][20].

Random vibrations are mainly caused by the rocket's propulsion system. The power spectral density (PSD) of the vibrations experienced by the payload strongly depends on the properties of the structure by which it is attached to the satellite and with which the satellite is attached to the adapter. The same is true for sine-equivalent vibrations. Detailed coupled loads analysis are required to determine the vibrations at the satellites level [18][20]. Figure 2.5 shows random vibration PSD for first stage flight at the adapter for the Electron, Soyuz ST, and Vega launch systems [17][19][20].

A parts ability to survive the random vibrations is tested by subjecting the part to spectrum associated with the launch vehicle. A part typically passes the test if there is no significant shift in the resonance frequencies before and after the test [21]. Testing for sine-equivalent vibrations is done similarly to testing for random vibrations with the only different being the type of vibration the part is subjected to [21].

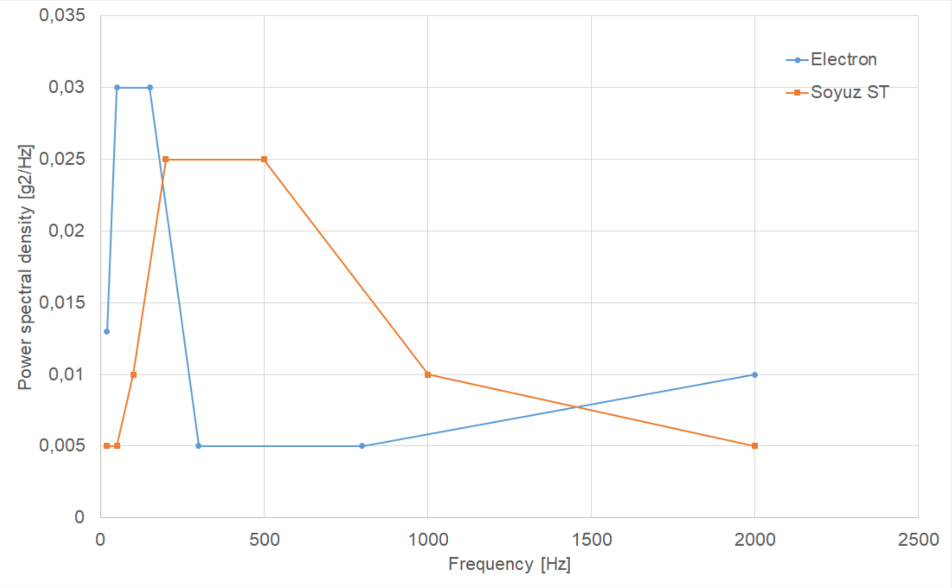

Figure 2.5: Power spectral density functions for the random vibrations at the adapter of the Electron and Soyuz ST launch systems [17][19]. Data on the Vega and Falcon 9 was unavailable.

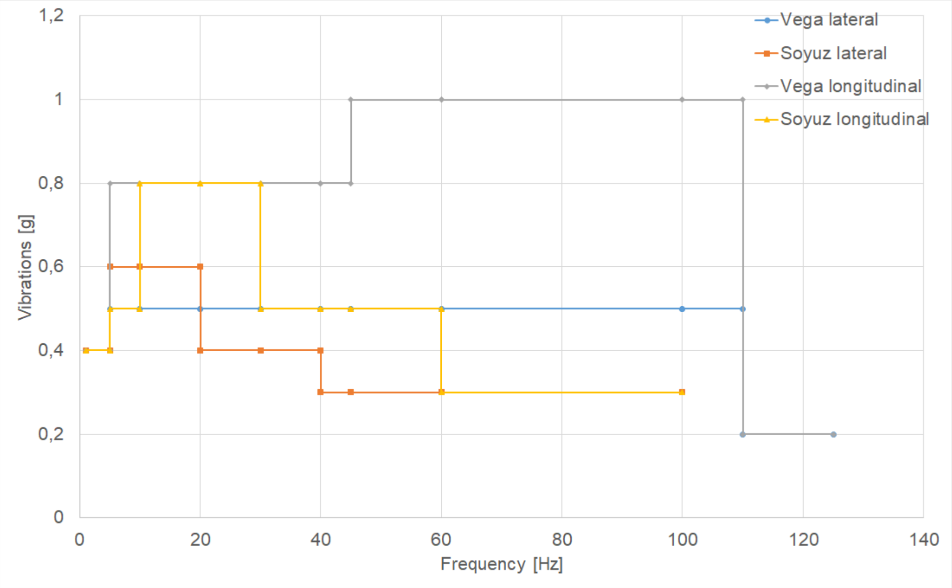

Figure 2.6: Sine-equivalent vibrations at the adapter for the Vega and Soyuz ST [19][20]. Data on the Electron and Falcon 9 was unavailable.

2.2.3. Shocks

Shocks occur during stage separation, fairing jettisoning, and satellite deployment. The shocks are caused by explosive bolts, latches, or the ignition of a stage. The accelerations are short-lived but very high [22]. Figure 2.7 shows the shock response spectrum for each of the four launchers.

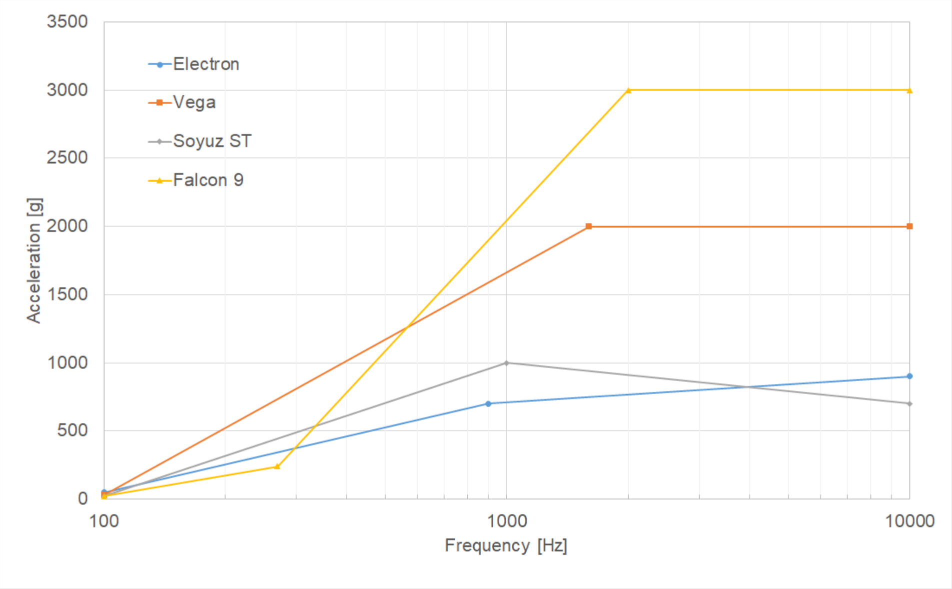

Figure 2.7: Shock response spectrum for the Electron, Vega, Soyuz ST, and Falcon 9 [17][18][19][20].

Whether a pocketqube or payload can survive the shocks it will experience can experimentally be demonstrated. This can be done by subjecting the part to the expected shocks, including a safety margin, in combination with a detailed pre- and post-visual examination and a performance test to verify the integrity of the hardware. [21].

2.2.4. Aerothermal flux

Apart from the mechanical forces a satellite also experiences heating due to aerothermal flux due to friction of the fairing, and after jettisoning the satellite, with the atmosphere [22]. However, considering that pocketqubes are launched inside pods and given that the aerothermal flux typically does not exceed the solar flux in orbit around the Earth, it is assumed that a pocketqube and its payload can withstand these conditions if they are capable of withstanding the thermal-vacuum environment described in Section 2.3 [19][20].

2.3. The low Earth orbit environment

Space is a hostile environment to both humans and machines alike. The environment in low Earth orbit (LEO, which is typically understood to be orbits with an altitude of less than 500 km) is influenced by an extensive amount of factors. This section limits itself to the most damaging aspects: The thermal-vacuum environment, ionizing radiation, and micro meteorites and other debris.

2.3.1. Thermal-vacuum

It is a well known fact that in space there is a vacuum. It is less well known that this does not mean that there are no particles interacting with the spacecraft. The Earth's atmosphere extends many hundreds of kilometers from the surface. In LEO satellites orbit inside the thermosphere, a region between approximately 85 km and 500 km altitude [23]. Inside the thermosphere, at an altitude of, for example, 500 km the atmospheric pressure is somewhere between $5 \cdot 10^{-8} mBar$ and $1 \cdot 10^{-10} mBar$ which is many orders of magnitude lower than the pressure at sea level which is approximately $1 \cdot 10^{3} mBar$ [24]. Although the atmosphere has a low density at this altitude, $4.1 \cdot 10^{-16} g/cm^3$ compared to $1.3 \cdot 10^{-3} g/cm^3$ at sea level [25], accumulated drag still causes the spacecraft to slow down over time. The atmosphere in LEO also contains ample amounts of atomic oxygen which reacts aggressively with various materials causing erosion [22][23].

The low pressures in space, compared to sea level, can cause outgassing issues. Outgassing occurs when atoms at the surface of a material evaporate out of it. Although this generally does not cause structural issues, it can affect, for example, the thermal properties of surfaces. Another issue with outgassing is deposition which can adversely influence optical surfaces or sensitive electronic components [22].

Because of the rarefied atmosphere in LEO the only method of heat transfer is by means of radiation. The sun contributes about 1330 W/m^2 to the radiative heat input in LEO while the Earth contributes about 200 W/m^2 in the form of directed reflected sunlight and infrared (IR) radiation [22]. The temperature reached by pocketqube will vary during the orbit where a maximum temperature is reached while in direct sunlight and a minimum is reached when it is eclipsed by the Earth and only receiving the Earth's IR input. A thesis conducting a thermal analysis of the Delfi-PQ found that external panels of the pocketqube reached a maximum temperature of about $50°C$ and a minimum temperature of approximately $-20°C$. The internal components are found to experience a less dramatic temperature change. Depending on the thermal capacity and on the heat dissipation of components the internal boards of the Delfi-PQ are found to have a maximum temperature between $30°C$ and $50°C$ and a minimum temperature at around $-5°C$ although some structural elements were found to reach $-20°C$ [26].

2.3.2. Ionizing radiation

The surface of the Earth is reasonably well protected from ionizing radiation originating in space. This protection is mainly from the Earth's magnetic field which prevents radiative particles from reaching the surface and from the atmosphere which absorbs the remaining radiation. The majority of radiation in space comes in the form of electrons and protons with lower levels of radiation due to heavier ions. These ionizing particles originate either from the sun or from sources outside the solar system. The magnetic field of the Earth traps most of the radiation in two belts around the Earth: the Van Allen radiation belts. Where the inner belt contains mostly protons and the outer belts contain mostly electrons [22].

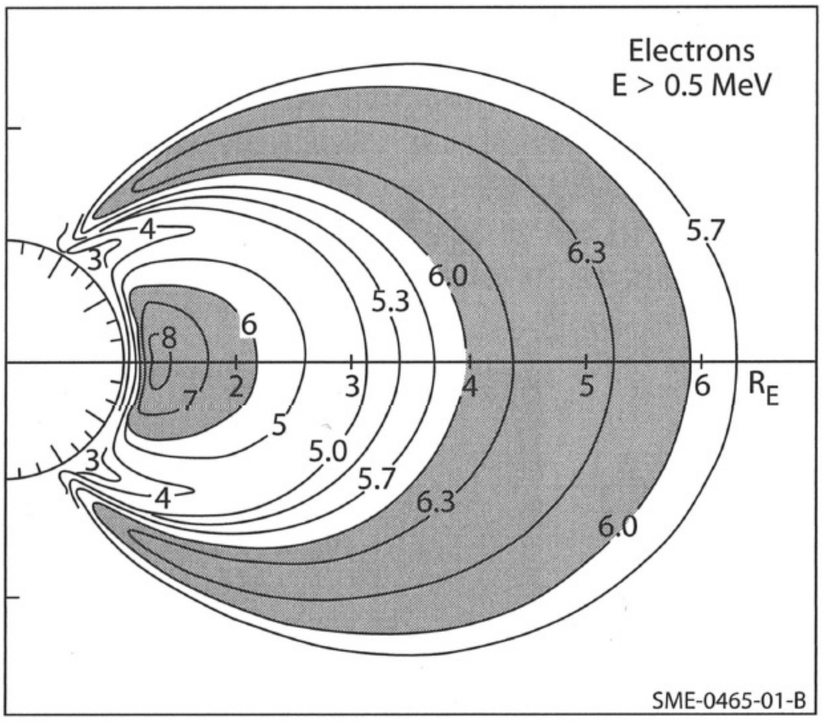

Figure 2.8: Diagram showing the inner and outer regions of electron radiation in the Van Allen radiation belts (Image source: [23]).

The altitude where the belts start are variable with the solar activity. The inner belt dips anomalously low over the south Atlantic in the aptly named south Atlantic anomaly. The proton energies vary between about 0.01 MeV and 400 MeV and are, due to their mass, far more damaging than the electron radiation which has energies between 0.4 MeV and 4.5 MeV [22][23].

Ionizing radiation can affect spacecraft in a variety of ways. The radiation can break molecular bonds in surfaces, for example, altering their thermal properties or causing lens browning [27][28]. Radiation also causes noise in optical detectors and can cause single event effects (SEE) in integrated circuits causing either erroneous changes in logic states called single event upsets (SEU), causing logic circuits to latch up called single event latch-ups (SEL) or causing the circuit to burn out in single event burnouts (SEB) [22][23].

2.3.3. Micro meteorites and other debris

There is a large number of debris in orbit, either naturally occurring or man made. Due to the high relative velocities collision with even tiny debris are hazardous for spacecraft due to the large kinetic energies involved. The amount of debris varies with altitude and inclination. Even impact with micro meteorites and tiny pieces of man made debris, such as flecks of paint, can impact a satellite by damaging and eroding the surfaces they strike [22][23].

2.4. Experiment selection

A spacecraft experiences a wide variety of different environmental conditions during its lifetime. The majority of these conditions can be simulated here on Earth. In order to allocate limited resources such as time and money not everything is useful to simulate. A first step would be to look at which environmental tests are required by the QB50 standard for cubesats and the ECSS-E-ST-10-03C regarding optical payloads.

The QB50 standard only stipulates qualification, acceptance, and flight testing requirements and does not specify tests for individual subsystems. Additionally, mechanical testing is required to take place while the cubesat is mounted inside a pod similar to the one it is being launched in [29]. Regardless, it is informative to look at the qualification test required by the QB50 standard for the full cubesat.

Table 2.2 contains an overview of potential qualificaiton tests and whether they are required by the QB50 and ECSS-E-ST-10-03C standards. Only tests that are at in at least one standard required or optional are listed.

Table 2.2: Overview of required and optional tests for cubesats and/or optical equipment [29][21].

Nr.	Category	Test	QB50	ECSS-E-ST-10-03C
1	General	Functional and performance	Required	Required
2	General	Humidity	Not required	Optional
3	General	Life	Not required	Optional
4	Mechanical	Physical properties	Required	Required
5	Mechanical	Static load	Required	Optional
6	Mechanical	Spin	Not required	Optional
7	Mechanical	Transient	Not required	Optional
8	Mechanical	Random vibration	Required	Optional
9	Mechanical	Acoustic	Not required	Optional
10	Mechanical	Sinusoidal vibration	Required	Required
11	Mechanical	Shock	Required	Required
12	Mechanical	Micro-vibration	Not required	Optional
13	Thermal	Thermal-vacuum	Required	Required
14	Thermal	Thermal-ambient	Not required	Depends on mission
15	Electrical	Electromagnetic compatibility	Required	Optional
16	Electrical	Magnetic	Not required	Optional
17	Electrical	Electrostatic discharge	Not required	Optional

Additionally, ECSS-E-ST-10-03C stipulates that either test 5 (static load), 6 (spin), or 7(transient) should be conducted if the loads are not fully covered by test 10, the sinusoidal vibration test. It also requires either a random vibration (test 8), an acoustic test (test 9), or both depending on the size, type, and location of the component. Test 12, the micro-vibration susceptibility test, is only required when there is a need identified by an analysis. Finally the thermal-ambient test (test 14) is only required if the component is designed to operate under ambient pressures after it has been exposed to vacuum [21].

The cameras investigated in this thesis are not yet in the qualification stage. However, the tests in Table 2.2 that are required for both the QB50 and ECSS-E-ST-10-03C standards provide a fairly sensible list of tests that one could conduct to test the space-worthiness of commercial off the shelf (COTS) cameras. These are:

1 Functional and performance test

4 Physical properties

5 Static load

8 Random vibration

10 Sinusoidal vibration

11 Shock

13 Thermal-vacuum

The functional/performance test and physical properties gather basic information about the component and the other 5 tests are aimed at determining the survivability of the component during launch and in space. However, due to limited resources only the functional/performance test, physical properties, and the thermal-vacuum test will be conducted. In what exactly these test entail this thesis will diverge from the above mentioned standards which primarily focus on the testing the functionality of the payload/subsystem within the operational context of a larger system. The cameras considered for this research have not yet reached the level of integration with a pocketqube to be able to do this.

2.4.1. Functional and performance test

QB50 and ECSS-E-ST-10-03C specify requirements for the functional and performance tests. However, these are qualification tests which is a stage not yet reached by the commercial off the shelf cameras used in this thesis. The metrics used in this test are given in Chapter 4 and the detailed setup is given in Chapter 5.

2.4.2. Physical properties

The following physical properties will be determined.

- Mass
- Dimensions and interfaces

These properties are measured for both cameras upon arrival and are presented in Table 3.4 and 3.5 in Section 3.3.

2.4.3. Thermal testing

The vacuum-oven available for testing can reach a vacuum pressure of $10^{-1} mBar$ which is admittedly significantly higher than the $10^{-5} mBar$ required in both the QB50 and ECSS-E-ST-10-03C [21][29]. Additionally the used vacuum-oven cannot cool. Therefore, a thermal-ambient test will be conducted which includes heating and cooling.

Table 2.3 contains the test characteristics for the thermal-vacuum tests according to QB50, ECSS-E-ST-10-03C.

Table 2.3: Test characteristics based on the QB50 standard and ECSS-E-ST-10-03C [21][29].

	QB50	**ECSS-E-ST-10-03C**
Min. temperature	$-20 \pm 2°C$	$T_{min} - 5°C$
Max. temperature	$50 \pm 2°C$	$T_{max} +° C$
Temperature variation rate	$\geq 1°C/min$	$< 20°C/min$
Dwell time	1 hour at extreme temperatures	2 hours at extreme temperature
Vacuum	$10^{-5} mBar$	$10^{-5} mBar$
Cycles	4	8 or ≥ 1 if combined with ambient cycles

The following requirements are for thermal testing.

I The thermal tests shall include both a thermal-vacuum and a thermal-ambient test.

II All temperature shall be measured at consistent locations on the cameras.

III The thermal-vacuum test shall test the cameras at a pressure of $10^{-1} mBar$.

IV The thermal-vacuum test shall bring the cameras to a max temperature of $50°C \pm 5°C$.

V The thermal-vacuum test shall include 2 cycles.

VI During the thermal-vacuum test camera switch-on shall only start after a dwell time of 1 hour at maximum temperature.

VII The cameras shall be subjected to a functional test before and after the thermal-vacuum test.

VIII The camera's mass shall be measured before and after the thermal-vacuum test to measure outgassing.

IX The cameras shall be switched on at the maximum temperature to demonstrate functionality during the thermal-vacuum test.

X During the thermal-vacuum test maximum temperatures the cameras shall be run at high load to determine their equilibrium temperatures.

XI The outgassing passing criteria is $< 1\%TML$.

XII The thermal-ambient test shall be conducted under atmospheric pressure.

XIII The thermal-ambient test shall bring the cameras to a minimum temperature of $-5^{\circ}C \pm 5^{\circ}C$.

XIV The thermal-ambient test shall bring the cameras to a maximum temperature of $50^{\circ}C \pm 5^{\circ}C$.

XV The thermal-ambient test shall include 4 cycles.

XVI The thermal-ambient test shall include a non-operating cycle.

XVII The thermal-ambient test shall demonstrate camera functionality at both maximum and minimum temperatures.

XVIII The cameras shall be subjected to a functional test before and after the thermal-ambient test.

2.5. Discussion

Apart from being handled here on Earth, satellites are subjected to two rather destructive environments during launch and when operating in space. During launch the satellite, and by extension, its payload are subjected to severe accelerations, high levels of acoustic noise, random and sinusoidal vibrations, and shocks. The accelerations and intensity of these forces vary from rocket to rocket but the spread between them is not as large one might expect from the different weight classes of the considered launch vehicles. In space there are several effects affecting a satellite. For individual components, such as the optical payload, the most important environmental consideration are outgassing, thermals, and internal and external degradation due to ionizing radiation, micro-meteorites, and atomic oxygen.

A lot of these factors are mission specific and their impact is analyzed for each specific mission. The mechanical environment during launch and the thermal environment in space are directly tested for and form the cornerstone of testing for spaceworthiness. Although these tests do not form a complete testing campaign for satellites or satellite subsystems they do provide a first insight in whether the components will survive and operate in space.

From the possible environmental tests, only a thermal-vacuum test will be conducted during this thesis. Due to the inability of the available vacuum-oven to cool below room temperature an additional thermal-ambient test is added to determine the cameras performance at low temperatures. A performance test is required before and after the thermal-vacuum and thermal-ambient tests to evaluate whether the tests had any adverse effects on the cameras.

In the next chapter, Chapter 3, the commercial off the shelf cameras that will be used for testing are selected. In Chapter 4 the metrics used in the performance test are discussed. The methodology of the tests themselves are discussed in Chapter 5.

3

Commercial off the shelf cameras

Before the experiments could be conducted two cameras had to be procured. This chapter describes the process of selecting these cameras. Section 3.1 describes the results of an internet search to create a list of potential cameras. In the next section, Section 3.2, the same is done for the lenses. After that the cameras are evaluated based on a first order analysis to determine their ground sampling distance and signal to noise ratio. Based on the results of that analysis two cameras are selected. Finally the results of this chapter are summarized and discussed in Section 3.4.

In order to avoid confusion the following terminology will be used. The terms *(board level) camera module* or *module* refer to the printed circuit board to which the light sensitive sensor and the electronics are attached. The terms *camera* or *imaging system* refer to the full system capable of capturing images and consists of a *module* and a lens. The term *sensor* only refers to the actual photovoltaic sensor.

3.1. Available board level camera modules

Cameras are everywhere and the terrestrial applications for science, industry, surveillance, and the taking of holiday pictures are nearly endless. It is no surprise then, that there is a very large quantity of commercial off the shelf cameras available. During this thesis only what are known as digital commercial off the shelf (COTS) *board level camera* modules are considered which are minimalistic cameras consisting of (usually) one printed circuit board (pcb) containing the sensor and some electronics, and a lens or lens mount. These camera modules are usually relatively easy to interface with via either USB or MIPI CSI (camera serial interface). Board level camera modules also come without a case which would have little use in space anyway. An internet search yielded 84 applicable camera modules although, this list is unlikely to be complete.

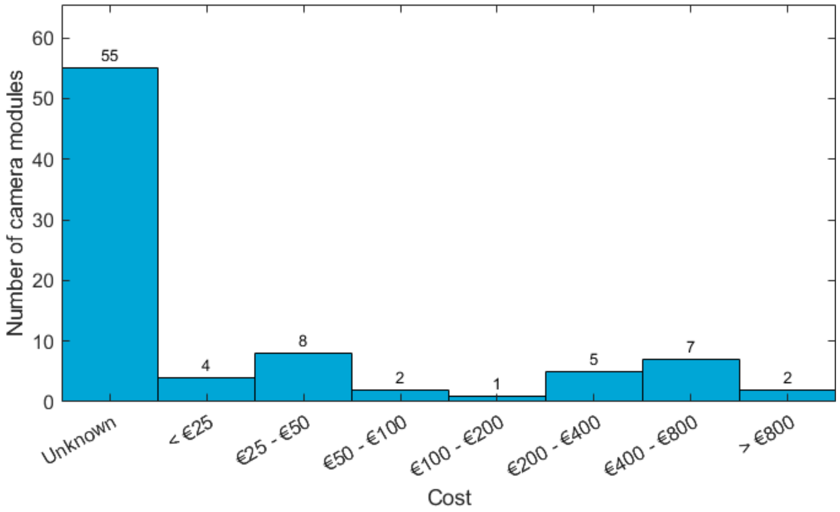

Figure 3.1: Histogram of the specified costs for COTS board level camera modules (2019).

Figure 3.1 shows the distribution of cost for the board level camera modules. A rough dichotomy can be distinguished between 'low-end' consumer modules, typically less than €100, intended for hobbyists or DIY applications, and more 'high-end' modules marketed towards scientific or industrial applications. The large quantity of modules with an unknown cost are modules for which a quotation has not been requested or received for this thesis. However, all of those are marketed towards either science or industry and it can reasonably be assumed that the majority of them would occupy space somewhere to the right of the plot in Figure 3.1.

The difference between the high- and low-end modules is not always clear from the data provided on the manufacturers website and data sheets. In general the high-end modules are slightly larger, consume slightly more power, and have a slightly larger pixel pitch than their low-end counterparts. The low-end modules typically specify, if specified at all, an operational temperature range between $-30°C$ and $70°C$ while the high-end cameras either fall within the industrial range of $-40°C$ to $85°C$ or have a much smaller operational temperature range between $0°C$ and $45°C$.

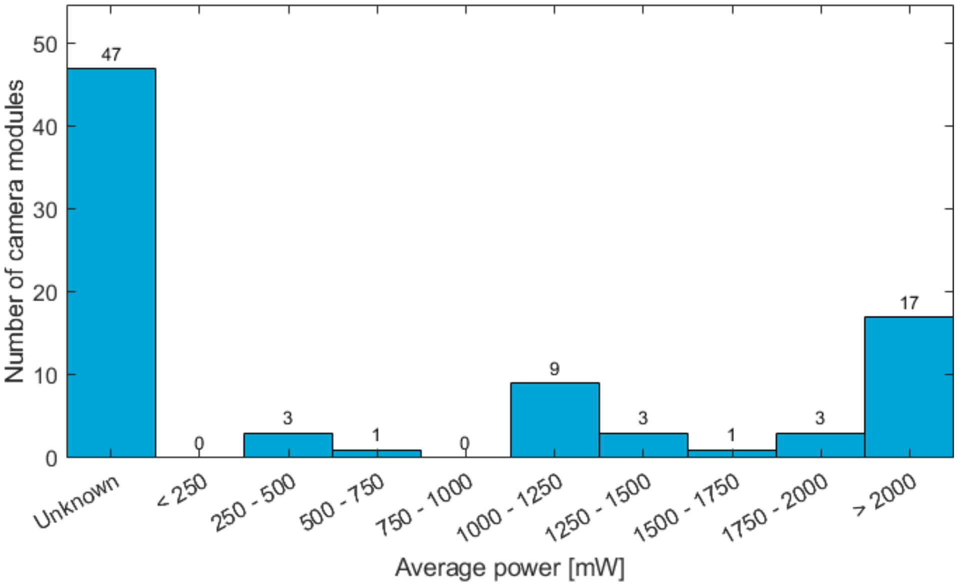

Figure 3.2: Reported average power consumption for COTS board level camera modules.

In Figure 3.2 the power consumption distribution is shown. For about 55% of the camera modules this is unspecified. Although there are some modules with low power consumption the majority requires more than 1 W with the average being around 2.2 W which is relatively high for a pocketqube to supply. However, the conditions under which this is measured is not typically specified and might not be representable of the conditions under which the modules would come to operate when installed in a pocketqube. Some connection types such as USB add to the power consumption. By connecting directly via, for example, the MIPI CSI power consumption could be lowered. The low-end cameras that have their power consumption specified typically report an average power consumption below 1.1 W. The high-end cameras have a much larger spread in power consumption which can roughly be divided into three sections. High-end cameras that have reported power consumptions have an average power consumption of about 1.2 W, between 2 and 2.5 W or more than 4 W.

The board level camera modules can be oriented inside the pocketqube either along (configuration 1) or across (configuration 2) the body-axis as shown in Figure 3.3.

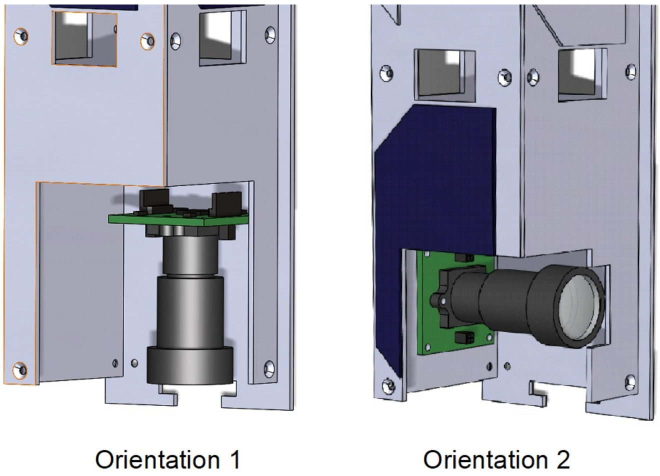

Figure 3.3: Illustration of camera orientation within a pocketqube.

Fitting a pcb in configuration 1 would require that both pcb dimensions are less than approximately 42 mm to also allow room for structural elements [6]. In configuration 2 at least one pcb dimensions should not exceed 42 mm while the other dimension can be somewhat larger, assuming a pocketqube larger than 1p.

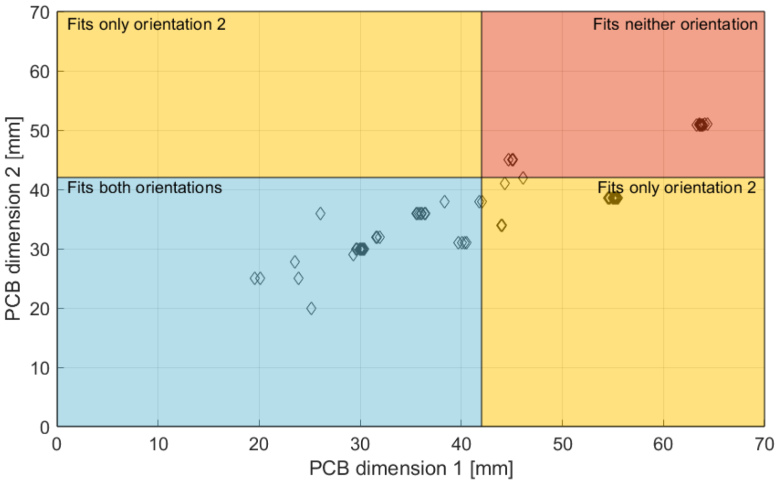

Figure 3.4: Distribution of both dimensions of the printed circuit boards. Some jitter has been added to the data to show overlapping data points.

Not all pcb's have square form factors. Figure 3.4 shows that 17 camera modules do not fit inside the pocketqube. 20 Modules only fit in orientation 2 while 45 modules can fit in either orientation 1 or 2. For 2 cameras the dimensions were not specified.

Out of the 84 camera modules 9 include a fixed lens. The other modules come with either a C, CS, or S lens mount the details of which is listed in Table 3.1. Lenses are attached to these mounts using threads. The C and CS mounts use a 25.4 mm thread while the S mount uses a 12 mm thread. The C and CS mount differ in depth. Most modules can be ordered with the preferred mount.

Table 3.1: Counts of the different lens mounts for the COTS camera modules.

Type	**Number of modules**
C	6
CS	7
S	33
C or CS	17
C or S	1
CS or S	1
C, CS, or S	10
Fixed lens	9

3.2. Available lenses

During this thesis only fixed focal length lenses are considered since these lenses have the least mass and complexity. There is a vast number of lenses commercially available and they come in all shapes and sizes. A list of 32 lenses was collected which only represents a small percentage of the available lenses. For C-, CS-, and S-mount type fixed focal length lenses the focal length typically ranges from about 1.68 to about 50 mm although still larger lenses are available. The F-number of the lenses usually varies between 1.8 and 2.8 where for lenses with a larger focal length the F-number slightly shifts towards the higher numbers. The aperture for pocketqube cameras is fundamentally limited due to the size of the pocketqube. This makes observations challenging due to the fundamentally limited signal that arrives. Maximizing the aperture is therefore important. The aperture, D, is related to the focal length, f, and the F-number, $F_\#$, using Equation (3.1).

$$D = f/F_\# \tag{3.1}$$

When imaging from low Earth orbit the Earth is so far away compared to the focal length of the camera that the lens should be focused at infinity. This means that, for a properly installed lens, the Earth will always be in focus regardless of the exact altitude. Considering this, and taking the thesis budget into account an Edmund Optics 50 mm infinite conjugate imaging lens with an F-number of 2.5 was selected for the analysis in Section 3.3 and experiments of this thesis. This camera has an aperture, as calculated by Equation (3.1), of 20 mm which is only slightly smaller than its physical aperture of 21 mm. This difference is caused by the presence of an F-stop. The other details of this lens are listed in Table 3.5.

3.3. COTS camera evaluation and selection

Together with a lens the camera module forms a fully functioning camera and can be analyzed and experimented upon. In this section a first order analysis will be conducted analyzing the 84 cameras. This will be used to get a general idea of the performance of the cameras and, together with cost, will be used to select two camera modules for experimentation.

The selection will be based on the spatial resolution, in the form of the ground sampling distance (GSD) that the cameras can achieve as well as their shot-noise signal to noise ratio (SNR). To simplify the analysis it is assumed that the cameras are installed in a satellite orbiting in an equatorial circular orbit at an altitude of 400 km. Although some cameras can be ordered without infrared (IR) cut filters it is assumed that all cameras have such a filter installed and only detect electromagnetic (EM) radiation with wavelengths between 400 and 700 nm.

3.3.1. Spatial resolution

Before calculating the GSD it might be worthwhile to look at the diffraction limit that governs the fundamental limit of what can be observed from a certain distance. This limit is calculated using the Rayleigh criterion given in Equation (3.2).

$$\Delta\ell = 1.22\frac{\lambda}{D}H \tag{3.2}$$

Where $\Delta\ell$ is the minimum distance two objects have to be apart to be able to differentiate them. At an altitude H of 400 km and at a wavelength λ of 700 nm this distance is, for an aperture D of 20 mm, 17.1 m.

This theoretical limit will not be achieved by the 84 cameras that are analyzed. Their spatial resolution is limited by the GSD of the system which represents the projection of a pixel onto the ground. The GSD is calculated using Equation (3.3).

$$GSD = d\frac{H}{f} \tag{3.3}$$

Where d is the pixel pitch. In Figure 3.5 the distribution of the ground sampling distances are shown.

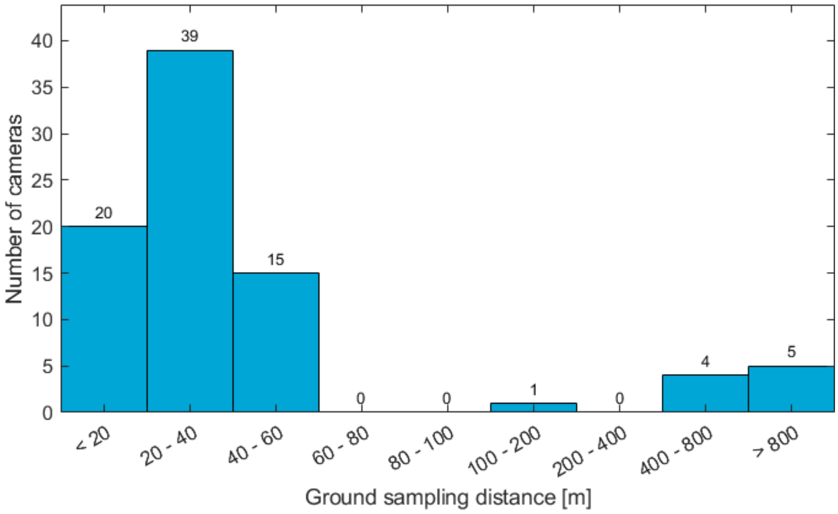

Figure 3.5: Ground sampling distances of 84 analyzed cameras when orbiting at an altitude of 400 km.

For the cameras using the $f = 50mm$ lens the minimum and maximum GSD is 9 and 59 meters respectively and the average is 29 m. For cameras with the fixed lenses this is 172 and 1600 m for the minimum and maximum GSD with an average of 916 m. These results already show the limitations of using first order calculations since 12 cameras have a GSD smaller than the diffraction limit for their lens. This simple analysis seems to suggest that these cameras are diffraction limited which is unlikely to be true. For lenses with a low F-number ($F\# \leq 4$) optical aberrations, inherent in the lens, limit the maximum achievable resolution. This effect is influenced by how small the tolerances are and how precisely the lens is manufactured. What can be concluded from this is that at least 12 and probably more cameras use the wrong lens.

However, these GSD results do put a cap on what can reasonably be expected in terms of resolution for a pocketqube based optical imaging system using COTS components. Scaling back the spatial performance can be achieved by selecting a different lens with a smaller focal length. Whether the spatial performance of these imagers is sufficient depends on the exact application, keeping in mind that a smaller GSD also results in a lower signal to noise ratio and a smaller instantaneous field of view. For example, 1080 pixels provide a swath width of 108 km with a GSD of 100 m and only 43 km with a GSD of 40 m. Finding the right lens for any application would mean having to balance those things. Given that when imaging close to the diffraction limit other aberrations can still significantly limit the achievable resolution a GSD of 40 m might provide a more reasonable expectation for a lower bound on the GSD. Although, a more detailed analysis is necessary to definitively conclude that.

Figure 3.6 illustrates the effect of the different resolutions. Figure 3.6a is the original image taken from Google Earth and has a resolution of approximately 3 m. Figure 3.6b is the same image with the resolution scaled back to approximately 18 m to demonstrate what the original image would look like when imaged at the diffraction limit for the 50 mm lens. The figures 3.6c and 3.6d show the image at a resolution of 40 m and 100 m respectively.

(a) Original image with a GSD of approximately 3.3 m (1906x876 pixels).

(b) Image scaled back to a resolution of approximately 20 m (318x146 pixels).

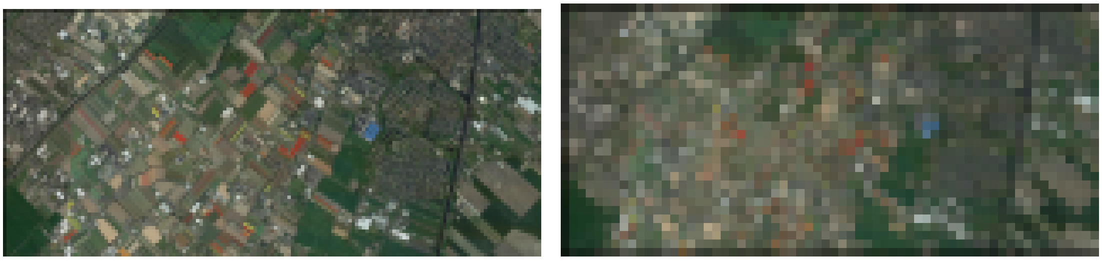

(c) Image scaled back to a resolution of approximately 40 m (159x73 pixels).

(d) Image scaled back to a resolution of approximately 98 m (64x30 pixels).

Figure 3.6: Aerial images of the fields south of Lisse scaled back to different resolutions. The border artifacts are caused by the convolution used to calculate down-sampled pixel values (image source: Google Earth).

3.3.2. Signal to noise ratio

A detailed analysis of the signal to noise ratio for each of the 84 cameras is beyond the scope of this thesis. A first order estimate can be calculated by assuming that the cameras are shot-noise limited. That is, the dominant source of noise is the signal itself and noise is thus proportional to the square root of the signal: $Noise \propto \sqrt{Signal}$. Using this the SNR can be calculated using Equation (3.4).

$$SNR_{dB} = 10\log_{10}\left(\frac{S}{\sqrt{S}}\right) \tag{3.4}$$

Where S is the signal in terms of the number of electrons released inside the photovoltaic sensor. The SNR is calculated for two cases. The first case consists of a sun and look angle that are both $0°$ and an albedo (α) of 0.25 which corresponds to dry soil. In the second case the look angle is $0°$, the sun angle is $60°$, and the albedo is 0.05 corresponding to the ocean [30].

The signal that arrives under these conditions at the detector can be calculated using Equation (3.5) [31].

$$S = \frac{GSD^2 \Omega \pi t_i}{4E_f} \int_{\lambda_{min}}^{\lambda_{max}} \eta(\lambda) L_{target}(\lambda) \tau_{optics}(\lambda) \lambda d\lambda \tag{3.5}$$

This equation consists of three parts: the radiant flux, the geometry, and the detector properties. The integral over $L_{target}(\lambda)$ is the spectral radiance (in $W/(m^2 \cdot \mu m \cdot sr)$ from a Lambertian target radiated in every direction. By dividing this total by the energy of a single photon, E_f (in Joules), the number of photons radiated away per second per meter squared per micron per steradian is calculated. In order to determine how many of the photons reach the detector the geometry is included where GSD^2 is the area of the Lambertian radiator and Ω the solid angle between the camera aperture and the radiator area. Finally the detector properties are considered. t_i Is the integration time determining for how long the detector will gather photons. The transmissivity of the optical elements in the lens is represented by $\tau_{optics}(\lambda)$ determining the percentage of photons not being reflected or scattered by the lenses. Finally $\eta(\lambda)$ is the quantum efficiency of the detector determining how many electrons are released per incoming photon [31].

Since $\Omega \propto aperture^2$ the geometry has the largest impact on the received signal. Increasing the GSD, by either increasing the pixel size or decreasing the focal length, and increasing the aperture size can significantly increase the received signal. However, this also lowers the resolution so a balance between the two has to be found.

A detailed explanation of how all the variables in Equation (3.5) are calculated can be found in Appendix A. In Appendix A it is also explained how the signal to noise ratios, calculated for each of the color channels (red, green, and blue), are aggregated into a single value.

The histograms of the SNR of each of the 84 cameras for both case 1 and case 2 are plotted in Figure 3.7.

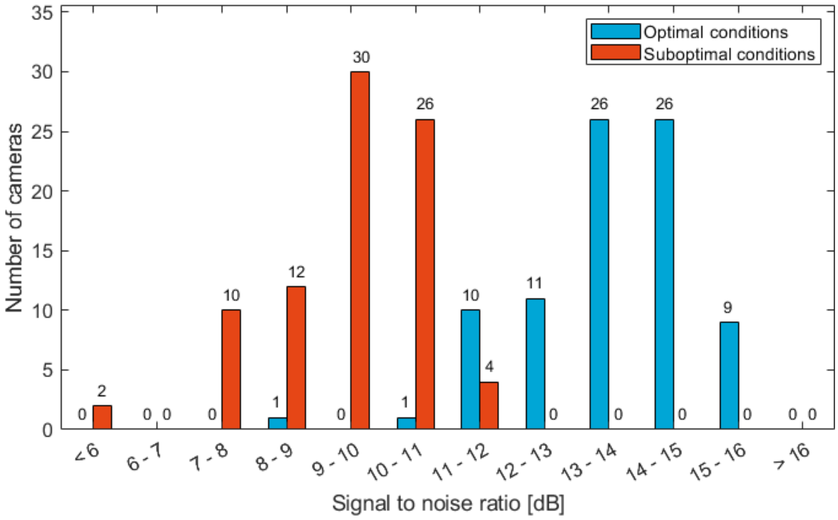

Figure 3.7: Histograms of the signal to noise ratios for each of the 84 cameras in case 1 (sun angle = 0 degrees and imaging dry soil) and case 2 (sung angle = 60 degrees and imaging ocean water).

In case 1 the lowest and highest SNR are 8 dB and 16 dB respectively with an average of 14 dB. For the second case the highest is 11 dB and the lowest SNR is 4 dB with an average of 9 dB. This is low.

For data from a well calibrated and characterized camera research is theoretically possible when there is more signal than noise which sets a lower signal to noise threshold of 2. However, due to inherent uncertainties the minimum SNR is typically higher depending on the application. For ocean or waterbody color measurements, signal to noise ratios in excess of 800 are usually recommended for observations in the visible part of the spectrum. A minimum threshold is not clearly defined and usually set either between 20-50 or 40-100 [32]. This would suggest that a pocketqube equipped with a camera would not be able to reach a sufficient SNR for ocean color measurements, especially considering that the calculated SNRs in Figure 3.7 are only shot-noise limited. The SNR could be increased by considering using a lower spatial resolution, binning pixels, or primarily observing very bright targets.

3.3.3. Camera selection

In order to select 2 out of the 84 cameras a small trade-off has been made. For this selection only the cameras which have a known cost of less than €200 are considered. Of this there are 15.

A small very basic trade-off is performed with three criteria, the GSD, the SNR calculated for observation case 1 (with a sun angle of 0 degrees and an albedo of 0.25), and the SNR calculated for observation case 2 (with the sun angle at 60 degrees and an albedo of 0.05). The three criteria have been given equal weight and are scored based on the criteria in Table 3.2. Power consumption would have, preferably, been a part of this trade-off. However, for only 6 out of the 15 cameras used in the trade-off an average power consumption is specified making it impossible to compare all cameras on a power based criteria. Of those 6 cameras average power consumption ranges between 300 mW for the e-CAM CUMI0330 MOD to 1100 mW for the See3CAM_CU135.

Table 3.2: Trade-off criteria.

	Excellent	**Good**	**Acceptable**	**Unacceptable**
GSD	**< 20 m**	**21 m - 50 m**	**51 m - 100 m**	**> 100 m**
SNR @ 0 degrees	**> 20 dB**	**15 dB - 20 dB**	**10 dB - 14 dB**	**< 10 dB**
SNR @ 60 degrees	**> 20 dB**	**15 dB - 20 dB**	**10 dB - 14 dB**	**< 10 dB**

The GSD score is *excellent* when the GSD is close to the theoretical limit and *good* when it is within the range that can reasonably be expected. The score decreases to *acceptable* for larger GSD's and to *unacceptable* for scores exceeding 100 m. Since a SNR of more than 20 dB would be sufficient for ocean color measurements it is considered to be *excellent* [32]. The score is *good* when between 15 and 20 dB and although such an SNR would be low it would likely still be very useful. Between 10 and 14 dB the SNR is considered to be *acceptable*. Below 10 dB the data will likely contain too much noise to be useful.

Applying these criteria to the 15 cameras gives the trade-off table shown in Table 3.3.

Table 3.3: Camera module trade-off table.

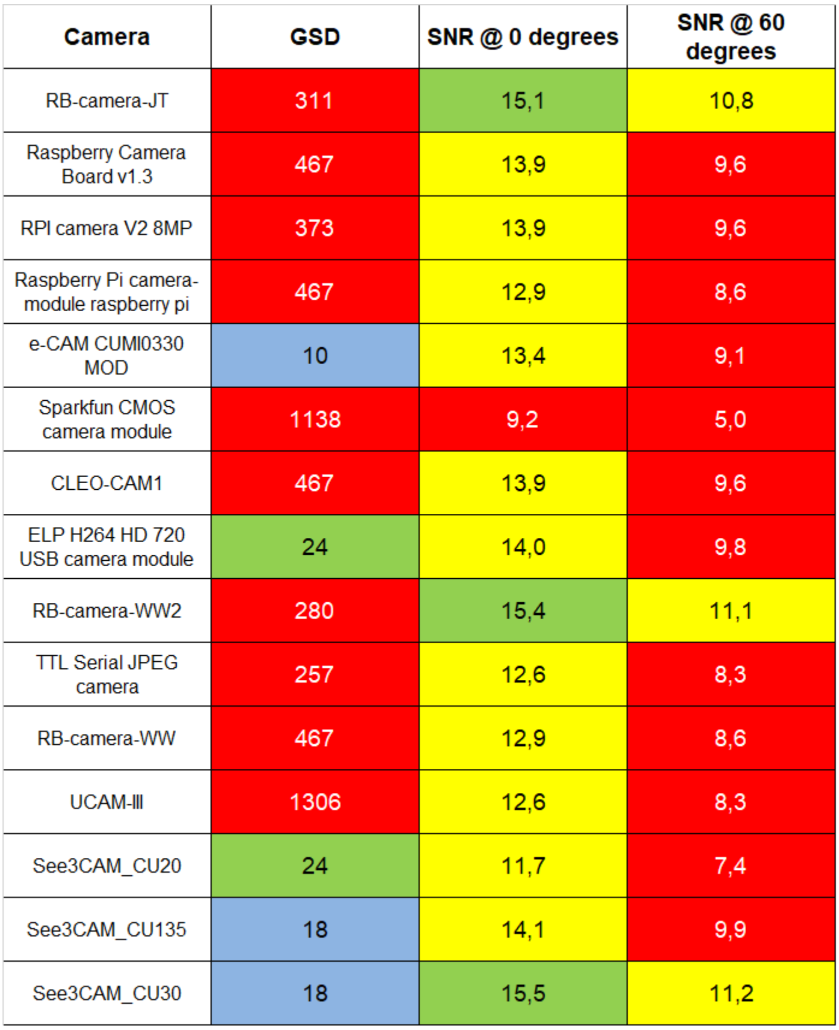

Camera	**GSD**	**SNR @ 0 degrees**	**SNR @ 60 degrees**
RB-camera-JT	311	15,1	10,8
Raspberry Camera Board v1.3	467	13,9	9,6
RPI camera V2 8MP	373	13,9	9,6
Raspberry Pi camera-module raspberry pi	467	12,9	8,6
e-CAM CUMI0330 MOD	10	13,4	9,1
Sparkfun CMOS camera module	1138	9,2	5,0
CLEO-CAM1	467	13,9	9,6
ELP H264 HD 720 USB camera module	24	14,0	9,8
RB-camera-WW2	280	15,4	11,1
TTL Serial JPEG camera	257	12,6	8,3
RB-camera-WW	467	12,9	8,6
UCAM-III	1306	12,6	8,3
See3CAM_CU20	24	11,7	7,4
See3CAM_CU135	18	14,1	9,9
See3CAM_CU30	18	15,5	11,2

From this trade-off the See3CAM_CU30 is the obvious choice. As a second camera the ELP H264 camera was also chosen, in part because of budgetary reasons and in part in order to have a second camera not from the See3CAM family of cameras. The ELP camera has the added benefit over the other non See3CAM cameras that it has an S type lens mount similar to the See3CAM_CU30 which means that the lenses are interchangeable.

The fact that the lenses can be swapped between the ELP camera and the See3CAM_CU30 is actually of considerable use. The See3CAM_CU30 camera, which will be called the See3CAM from here on, comes without an IR-cut filter. The ordered 50 mm infinite conjugate (IC) lens also has no IR-cut filter meaning that the combination of the See3CAM with the IC lens would detect light with wavelengths larger than 700 nm distorting the color representation of the camera. However, the ELP camera comes with both an IR-cut filter installed on the camera module and a lens also with an installed IR-cut lens. For the duration of the experiments the ELP module will be used in combination with the IC lens and the See3CAM in combination with the lens that accompanied the ELP camera. Table 3.4 contains the basic information about the See3CAM and ELP camera modules while Table 3.5 contains the information about both lenses.

Table 3.4: Basic information about the See3CAM and ELP cameras [33][34].

Full name	See3CAM_CU30	ELP H264 HD 720 USB camera module
Shorthand name	See3CAM	ELP
Manufacturer	E-con systems	Ailipu Technology
Length	30 mm	36 mm
Width	30 mm	36 mm
Mass	12 g	11.5 g
Lens mount	S	S
Interface	MIPI CSI with usb3.0 evaluation board	usb2.0
Sensor type	CMOS	CMOS
Pixel pitch	2.2 μm	3 μm
Optical format	1/3”	1/4”
Pixels	2304x1536	1280x720
Bit depth	10	10
Sensor	AE0330	OV9712
GSD (IC lens)	18 m	24 m
SNR (0 degrees, IC lens)	15.5 dB	14 dB

Table 3.5: Basic information about the IC and WA lenses [34][35].

Shorthand name	IC lens	WA lens
Manufacturer	Edmund Optics	Unknown
Focal length	50 mm	3.6 mm
Aperture	20 mm	2 mm
F number	2.5	1.8
Mass	29.5 g	4.5 g
Length	52.8 mm	17 mm
Diameter	27 mm	14 mm
Optical format	1/2”	1/2.7”
Mount type	S	S

3.4. Discussion

There is a large quantity of commercial off the shelf camera modules available with varying compatibility with the pocketqube platform in terms of power, size, and temperature range. Most modules fit within a 3p pocketqube platform and have temperature ranges compatible with the expected range described in Section 2.3. Power appears to provide the largest compatibility challenge with power consumption regularly in excess of 1 W which exceeds the estimate for available power in Section 2.1.

A first order analysis shows that the camera modules, in combination with a 50 mm lens, can expect a ground sampling distance somewhere between 20 and 60 m. However, this analysis does not include a detailed analysis of effects such as (optical) aberrations making it unclear whether or not the cameras can effectively reach these low spatial resolutions. The analysis also showed that the cameras would operate at relatively low signal to noise ratios, especially considering the optimal imaging conditions and the assumption of the noise only consisting of the shot-noise.

Based on the first order analysis and thesis budget the See3CAM_CU30 and ELP H264 HD 720 USB camera module were selected together with two lenses. For practical reasons the combination of the See3CAM with the 3.6 mm WA lens and the ELP with 50 mm IC lens will be used. These cameras will are subjected to the experiments proposed in Section 2.4. The next chapter describes how the performance of the cameras will be characterized.

4

Camera performance metrics

In order to characterize the performance of the cameras seven performance metrics will be introduced in this chapter. These include the modulation transfer function (MTF), color distance, signal to noise ratio (SNR), full well capacity (FWC), average dark signal, chromatic aberration, and optical distortion. These metrics make it possible to measure possible changes in the cameras caused by the thermal-ambient and thermal-vacuum tests. In this chapter their general principles are explained.

In order to measure the performance metrics a performance test must be conducted in a controlled environment. The exact method of testing is discussed in Section 5.3. The performance test makes use of three test charts.

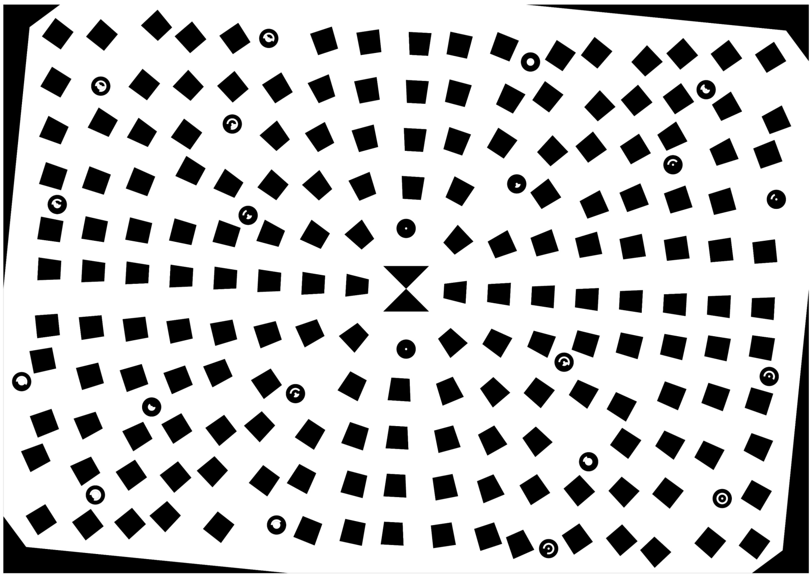

Figure 4.1: Chart used for the characterization of the modulation transfer function.

Figure 4.1 shows the chart used for measuring the modulation transfer function. This chart was generated using the open-source software MTF Mapper and is a chart that works specifically with MTF Mapper.

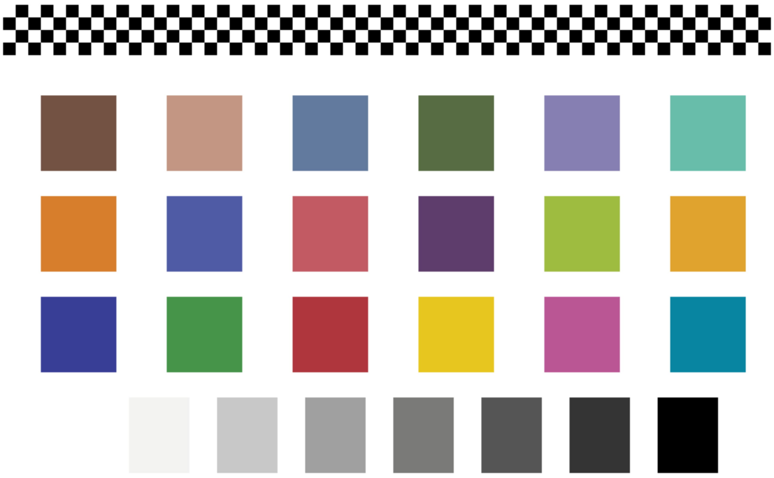

Figure 4.2: Chart used for the color distance measurement and signal to noise ratio.

The 18 colored squares in Figure 4.2 are used to determine the change in color representation of the cameras. The gray squares at the bottom are used for the measurement of the signal to noise ratio.

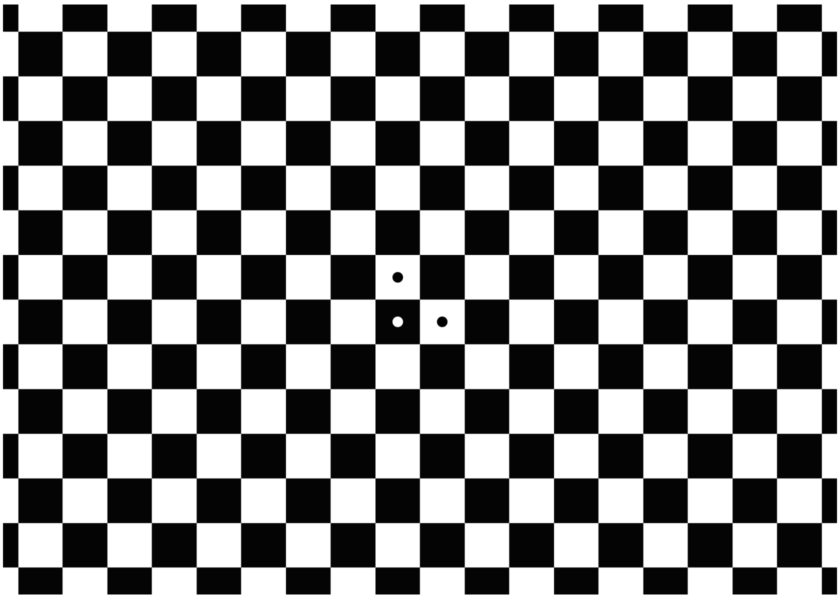

Figure 4.3: Chart used for measuring the chromatic aberrations and optical distortion.

The sharp edges of the checkerboard pattern in Figure 4.3 are used to determine the amount of chromatic aberration in the camera. The corners of the black and white squares are used to determine the distortion of the image.

4.1. Modulation transfer function

The modulation transfer function is a measure that describes the spatial frequency response of a system to a given input. It shows how well a system is able to transfer contrast from the scene it is observing to an image for any given resolution [36][37]. For example, the contrast between photographed black and white bars is high when the bars are far apart and decreases when the bars get closer and closer together. Figure 4.4 shows this. The left side of the figure has a low spatial frequency and high contrast while the left side of the figure has a high spatial frequency and low contrast. Id est, on the left side bars are far apart and clearly distinguished. On the left side the bars are close together and blurred. When contrast is too low it becomes impossible to resolve objects effectively.

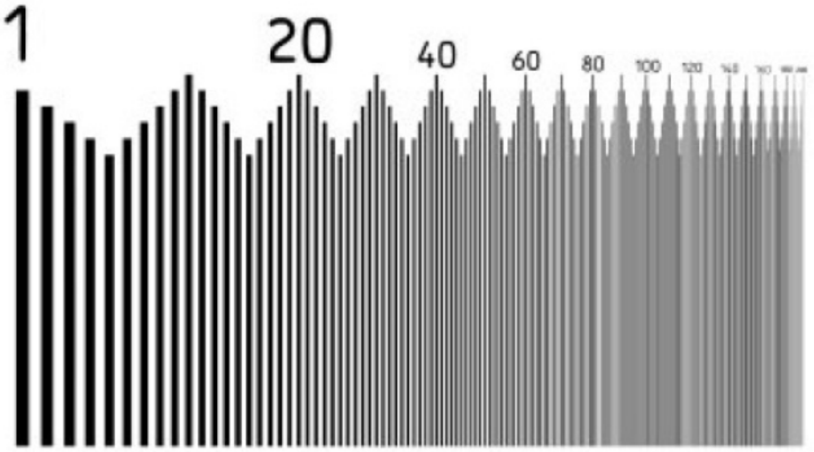

Figure 4.4: Example of MTF using alternating black and white bars (image source: [38]).

There are variety of techniques to measure the MTF and in this research the slanted edge method will be used. This method is based on an image taken of a sharp slanted edge either in the form of a printed high-contrast edge or a back-lit sharp edge [36][37]. The MTF can be determined from a slanted edge by first computing the edge spread function (ESF) of the edge. The derivative of this function forms the line spread function (LSF). By computing the discrete Fourier transform of the LSF the MTF is calculated [36][37][39].

The data will consist of images off the test chart illustrated in Figure 4.1. For each of the 700 slanted edges in the test chart an MTF curve will be calculated. However, each of these curves is of less interest than the information that the whole conveys. Therefore, the data that will be used consists of the MTF50 and MTF20 values plotted over the entire field of view (that is, the spatial frequencies where the MTF curves hit 50% or 20% contrast). This data is particularly useful for comparisons before and after experiments since it can show whether any change in the cameras ability to resolve certain spatial resolutions has changed.

4.2. Color distance

The ability of a camera to capture color is one of its key aspects. The exact colors that a camera captures are dependent on a number of factors such as lighting and the camera's exposure settings. For this metric the more interesting aspect is whether the color capturing ability changes during or after environmental tests.

In order to measure this it is important that all performance tests are conducted under the same conditions in terms of lighting and camera settings. Under these conditions the pictures will be taken of the color chart which is shown in Figure 4.2. The 18 colored squares on the chart form the basis of the measurement.

For each measurement the color of each of the colored squares is sampled. These RGB values are converted to CIELAB L*a*b* color space from which HCL (hue, chroma, luminance) can be determined. These HCL values are used to calculate the ΔE_{2000} (sometimes ΔE_{00}) color distance using Equation (4.1). This is done for each of the colored squares in Figure 4.2. This metric calculates the distance in color space between the measured sample and a reference color. For this reference color the results of the first performance test will be used. This takes the non-linearity of human color perception into account and allows one to determine whether a color change is perceptible or not. The details of how all values in Equation (4.1) are calculated can be found in Appendix B.

$$\Delta E_{2000} = \sqrt{\left(\frac{\Delta L'}{K_L S_L}\right)^2 + \left(\frac{\Delta C'}{K_C S_C}\right)^2 + \left(\frac{\Delta H'}{K_H S_H}\right)^2 + R_T \left(\frac{\Delta C'}{K_C S_C}\right)\left(\frac{\Delta H'}{K_H S_H}\right)} \tag{4.1}$$

4.3. Signal to noise ratio

The signal to noise ratio (SNR) can be calculated in many different ways. The different calculation methods not all represent the same SNR and can therefore not always be compared. Since both the See3CAM and the ELP camera do not allow for direct access to the sensor readout the SNR will be calculated based on fully processed images. For this calculation the cameras are required to operate without sensor gain [40].

The measurement will be conducted by imaging the color chart shown in Figure 4.2. The 8 grayscale squares at the bottom are used. The SNR for each of the squares is calculated using Equation (4.2).

$$SNR_{dB} = 20\log_{10}\left(\frac{\sum(\mu_i)}{\sqrt{\sum(\sigma_i^2)}}\right) \tag{4.2}$$

Where μ_i and σ_i are the mean and standard deviation for each color channel (red, green, blue) [40]. Note that this SNR calculation is different from the one in Section 3.3 and that both results are not directly comparable.

4.4. Full well capacity

The full well capacity (FWC) refers to how much charge a single pixel can hold before it is saturated. A higher FWC indicates a larger dynamic range for the camera. Unfortunately both the See3CAM and ELP cameras do not allow direct access to the sensor readout so an FWC measurement in terms of actual charge is impossible. Fortunately the FWC can also be measured from captured images although this provides less information since the translation between charge and pixel value has already been made.

This can be done by taking a series of images of a white background under constant illumination with increasing integration time. Each pixel value corresponds with a certain amount of charge held in the pixel.

4.5. Average dark signal

Noise can have a significant impact on the performance of a camera. Two sources of noise are fixed noise introduced by the circuitry in the camera and thermal noise which varies based on both temperature and integration time. A measure of these two noise sources can be determined by determining the average dark signal of the camera.

The average dark signal is measured in as dark a setting as possible. In these conditions a series of images is taken at varying integration times. In order to reduce temporal variation within the dark signal 10 measurements are taken per exposure time and averaged.

4.6. Chromatic aberration

Chromatic aberrations (CA) occur when light of different colors is focused slightly differently depending on the wavelength. This effect can occur in both axial direction, where the focal length is a function of the wavelength, or in lateral direction where the focal point has been shifted slightly. It is primarily an aberration of the lens.

CA is best visible near sharp edges. For this reason it can be quantified using the test chart in Figure 4.3. The CA will be measured by sampling a number of edges in order to construct an edge spread function. The chromatic aberration is quantified as the maximum distance between any of the three color channels at a normalized ESF value of 0.5. This is illustrated in Figure 4.5.

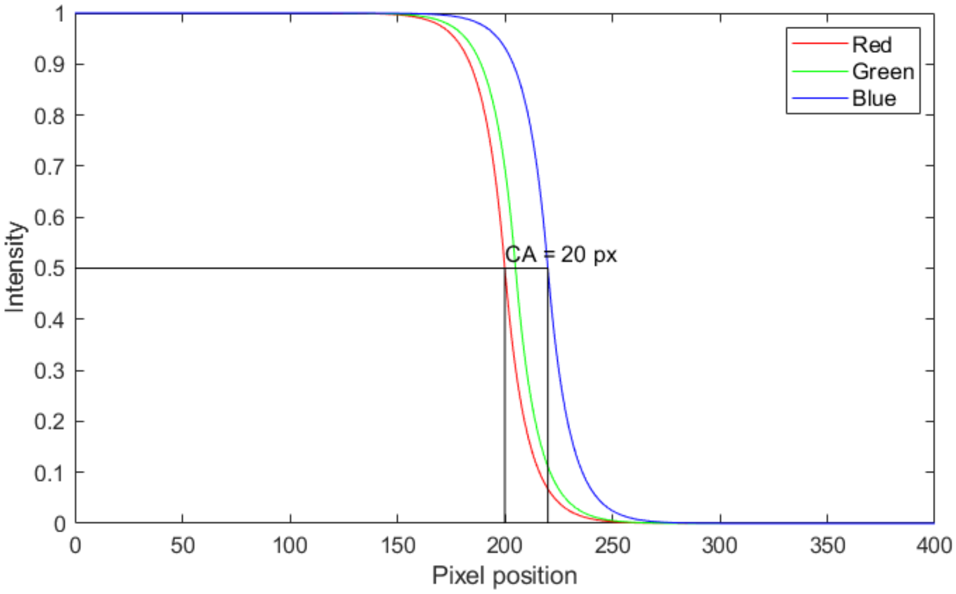

Figure 4.5: Example of chromatic aberration. The red, green, and blue edge spread functions do not overlap. Chromatic aberration is quantified as the maximum distance between two curves at 0.5 intensity.

4.7. Distortion

Optical distortions happen when imaged straight lines are not projected as such on the image plane. This is an issue of the lens. There are, primarily, two types of distortion: pincushion, where lines that do not go through the center of the image are bend inward, and barrel distortion where those lines are bend outward. Figure 4.6 illustrates this.

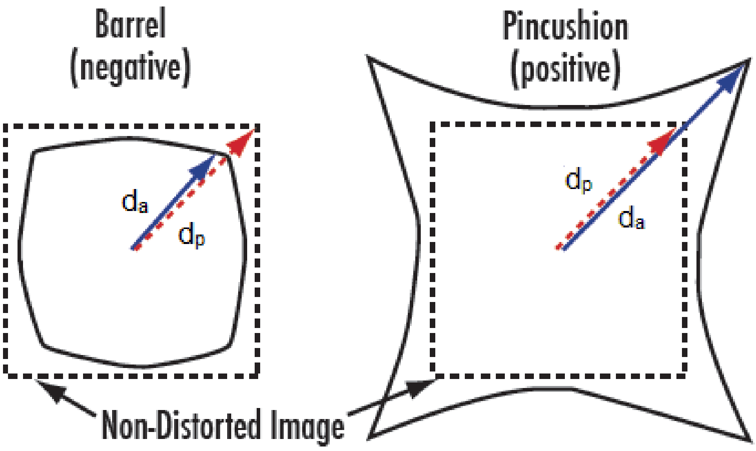

Figure 4.6: Example of the two most common type of distortion (image source: [41]).

The distortion is measured using the checkerboard chart illustrated in Figure 4.3. All the corners of the black and white squares are in known positions. From this the distortion can be quantified as the percentage difference between the actual and predicted (undistorted) location.

$$D_{dist} = \frac{d_a - d_p}{d_p} \tag{4.3}$$

4.8. Discussion

The discussed performance metrics together provide a reasonable overview of the performance of a camera. The full well capacity and average dark signal form a rudimentary characterization of the photovoltaic sensor based on processed images in lieu of direct access to the sensor readout data. The chromatic aberration and distortion metric look at two common lens aberrations while the signal to noise ratio and color space measurement characterize the radiometric performance of the camera.

Camera characterization is a specialization in and of itself requiring experience and dedicated hardware to do properly. A full characterization is therefore outside the scope of this thesis. The metrics discussed in this chapter are not intended for absolute measurements comparable to characterizations performed by other industry or scientific parties. Instead the measurements are intended to measure changes in the camera that might occur due to the experiments proposed in Section 2.4. Because the metrics roughly cover all aspects of the camera they should, in theory, point towards which aspects changed allowing for some level of pinpointing failures.

In the next chapter, Chapter 5, the materials and methods are discussed by which the performance metrics are measured.

5

Materials and method

In this chapter the materials and methods used to conduct the various experiments will be explained. First the general order of the experiments will be shown and some general remarks regarding temperature measurements are given. Then, in Section 5.1, the practical aspects for the integration time characterization is given. In Section 5.2 the same is done for the experiment to determine power consumption during various operational modes. After that, in Section 5.3 the performance tests are explained. In Section 5.4 and 5.5 the thermal-ambient and thermal-vacuum experiments are explained respectively. Finally, in Section 5.6 the procedure for an additional measurement of the average dark signal is given.

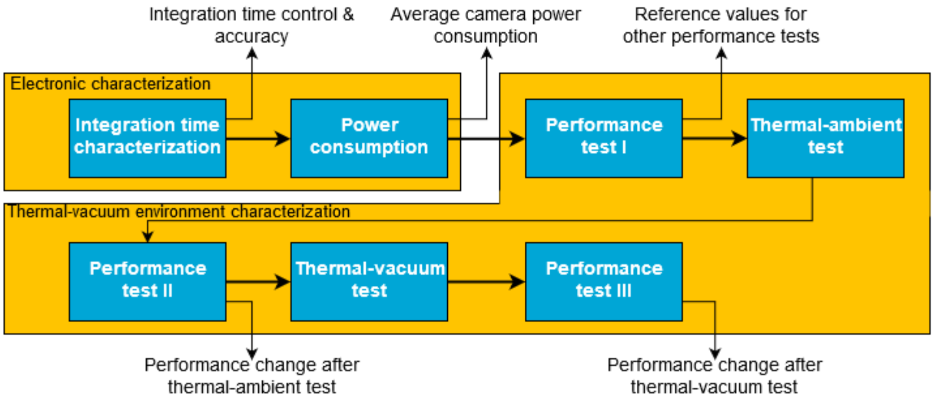

Figure 5.1: The order in which all the experiments have been conducted.

Figure 5.1 shows the order in which all the experiments have been conducted. An additional measurement of the average dark signal under hot conditions ($50^{\circ}C$) was conducted between the thermal-vacuum test and performance test III. The motivation for this is explained in Section 5.6.

During each of the experiments the temperatures of the cameras were measured. This was done using negative temperature (NTC) thermistors. For both cameras one was attached to the lens-mount and one was attached directly to the backside of the camera pcb using kapton tape. In Appendix C the method for measuring the temperatures using these NTC thermistors is explained.

Communication between the cameras and a computer was done exclusively using USB2.0.

5.1. Integration time characterization

Both cameras have two modes of operation: streaming and single mode. The streaming mode for both cameras operate with fixed framerates determined by their settings. Larger frame sizes decreases the framerate. In the single image mode images can be taken back to back which also allows data to be obtained at a certain framerate. In order to determine the maximum framerate that can be obtained in this manner the following test was conducted.

The cameras were set to a specific frame size both with and without MJPG compression, the frame sizes are listed in Table 5.1. The exposure time was varied from their minimum to maximum value. For each of the exposure times 100 images were taken back to back. Based on the time, t, it took to take these 100 pictures the achieved effective framerate, fps_e, can be determined using the relation $fps_e = 100/t$. Both cameras were controlled using MatLab.

Table 5.1: Configurations for duty cycle experiment

See3CAM			**ELP**		
Nr.	Resolution	Compression	Nr.	Resolution	Compression
1	2304x1536	false	5	1280x720	false
2	2304x1536	true	6	1280x720	true
3	640x480	false	7	640x480	false
4	640x480	true	8	640x480	true

5.2. Power

The total amount of power consumed by the cameras was measured by attaching a multimeter to $B_{bus}5V$ wire of the USB2.0 cable and measuring the current drawn by the camera. Power is calculated by multiplying the current with USB output voltage of $5V \pm 5\%$ [42]. Power was measured for both the streaming and single image mode of the cameras. Table 5.2 lists the modes for both cameras for which the steady state power consumption was determined.

Table 5.2: Configurations used during the measurement of power consumption.

See3CAM				**ELP**			
Nr.	Resolution	Mode	Compression	Nr.	Resolution	Mode	Compression
1	2304x1536	streaming	false	13	1280x720	streaming	false
2	2304x1536	streaming	true	14	1280x720	streaming	true
3	2048x1536	streaming	false	15	640x480	streaming	false
4	2048x1536	streaming	true	16	640x480	streaming	true
5	1920x1280	streaming	false	17	320x240	streaming	false
6	1920x1280	streaming	true	18	320x240	streaming	true
7	1280x720	streaming	false	19	1280x720	single image	false
8	1280x720	streaming	true	20	1280x720	single image	true
9	640x480	streaming	false				
10	640x480	streaming	true				
11	2304x1536	single image	false				
12	2304x1536	single image	true				

During streaming mode power was measured for 5 minutes to determine the steady state current consumption during operation. During single image mode the integration time of the cameras was varied from their minimum to maximum values. For each integration time the camera was operational for approximately 5 minutes during which the steady state current was measured.

In addition to the scenarios listed in Table 5.2 the current was also measured when the cameras were in idle mode.

5.3. Performance testing

The performance test is a series of smaller experiments conducted on the cameras to get a detailed overview of the performance of both cameras. By conducting this test before and after the thermal-ambient and the thermal-vacuum test changes in the performance of the cameras due to the environmental conditions to which the cameras were subjected could be determined. The theory of the performance metrics is discussed in Chapter 4. This section focuses on the practical test setup and practical aspects arising in the analysis of the data obtained by the performance test.

5.3.1. Setup

The cameras were mounted in a 3D printed frame as shown in Figure 5.2. Two L-shaped brackets were also 3D printed in which the frames fit. The two brackets were clamped down in the test setup which allows the cameras to be placed in the same position every time. The two L-shaped brackets were printed using PLA (polyactic acid) filament while the camera frames were made from PC (polycarbonate) which allows them to also be used in the vacuum-oven.

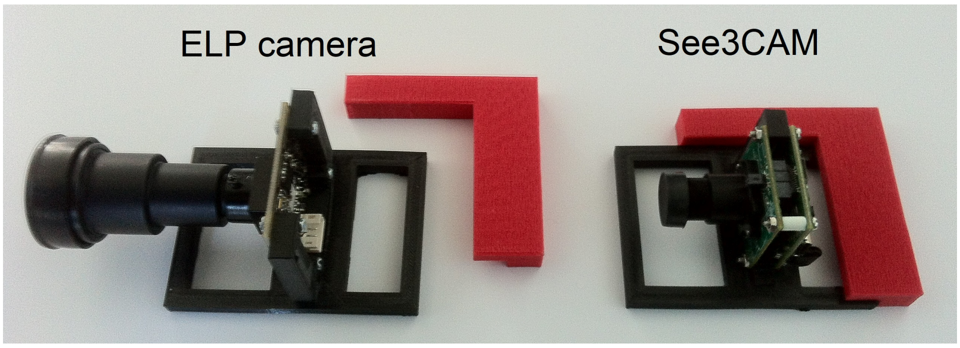

Figure 5.2: figure showing the ELP (left) and See3CAM (right) in their 3D printed frames and clamping brackets.

The setup was located in a dark room with minimal light from the outside. For lighting two 4200 lumen LED lights with a light temperature of 6000 K were used. The lights measured 120x30 cm and were placed upright to ensure an even vertical light distribution. The lights were placed at approximately $45°$ angles from the optical center line as shown in Figure 5.3.

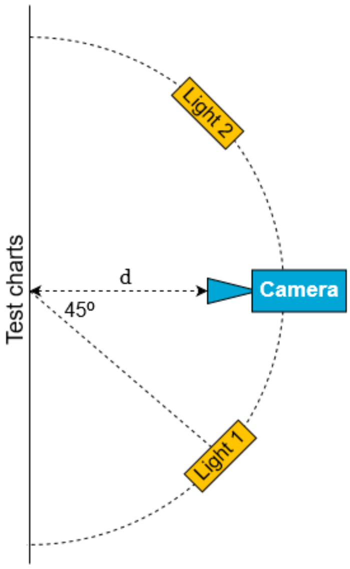

Figure 5.3: Schematic overview of the test setup used for the performance test. For the See3CAM d is 30 cm and for the ELP d is 270 cm.

The See3CAM and the ELP were placed 30 and 270 cm from the test charts respectively. The lights were placed approximately 50 cm from the test charts for both the tests involving the See3CAM and ELP. Due to the narrow field of view of the ELP camera it can image in between both lights without seeing them. The test charts, shown in the figures 4.1, 4.2, and 4.3, were printed on $200g/m^2$ paper to minimize chart warping. For the See3CAM the charts were printed on A3 size and for the ELP the charts were scaled to slightly smaller than A5 and printed on A4 paper. The charts were attached to a flat gray wall using magnets.

The camera settings were identical for every performance test. Brightness, gain, sharpness, pan, tilt, zoom, and hue were set to minimize their effect on the captured image. Contrast, and saturation were kept at factory settings. Both cameras can automatically set the values for exposure, gamma, and white balance. For the performance tests these settings were fixed by setting them to values that produced images that approximately looked like the images created using the automatic settings. Table 5.3 contains the settings used for each of the cameras as well as the range that these values can take. The See3CAM contained a LED light on the back of its pcb. To minimize its interference with the measurement of the average dark signal the LED was covered completely.

Table 5.3: Settings for the cameras during the performance test. Ranges are indicated between square brackets.

Setting	**See3CAM**	**ELP**
Exposure mode	manual [auto/manual]	manual [auto/manual]
White balance mode	manual [auto/manual]	manual [auto/manual]
Brightness	0 [-15 15]	0 [-64 64]
Contrast	10 [0 30]	32 [0 64]
Exposure	-9 [-13 0]	-9 [-13 -1]
Gain	1 [1 100]	0 [0 100]
Gamma	270 [40 500]	89 [72 500]
Saturation	16 [0 60]	64 [0 128]
Sharpness	0 [0 127]	0 [0 6]
White balance	6400 [1000 10000]	5800 [2800 6500]
Pan	0 [-180 180]	-
Tilt	0 [-180 180]	-
Zoom	100 [100 800]	-
Hue	-	0 [-40 40]

5.3.2. Data gathering and analysis

The performance test consists of a series of five measurements from which the seven performance metrics discussed in Chapter 4 are determined. Figure 5.4 summarizes the process for conducting the test. During the test the cameras are controlled using MatLab.

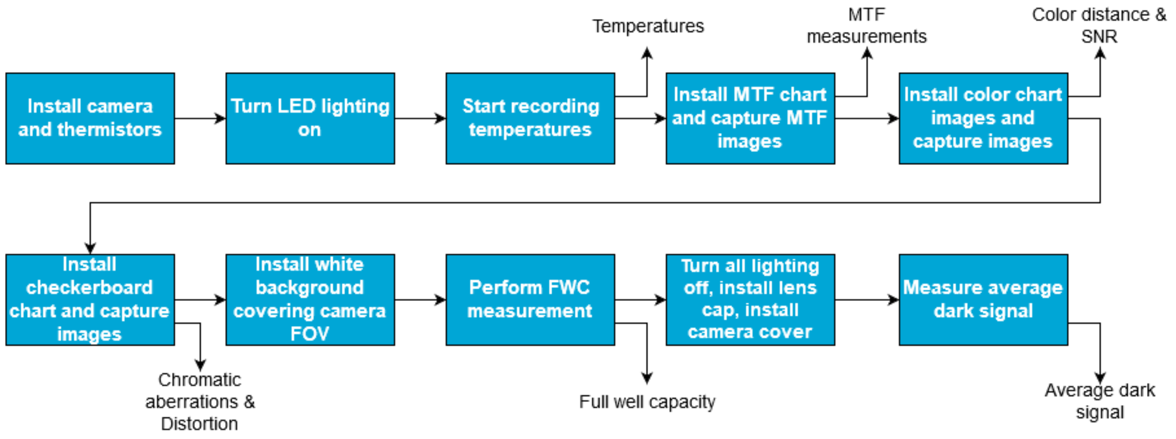

Figure 5.4: Overview of the steps taken in order to conduct a performance test.

The consistency of the setup was tested by repeating the performance test for both cameras twice on two different days. This demonstrated that the measurements were consistent. The details of this are described in Appendix D. Figure 5.5 shows the See3CAM in the performance test setup.

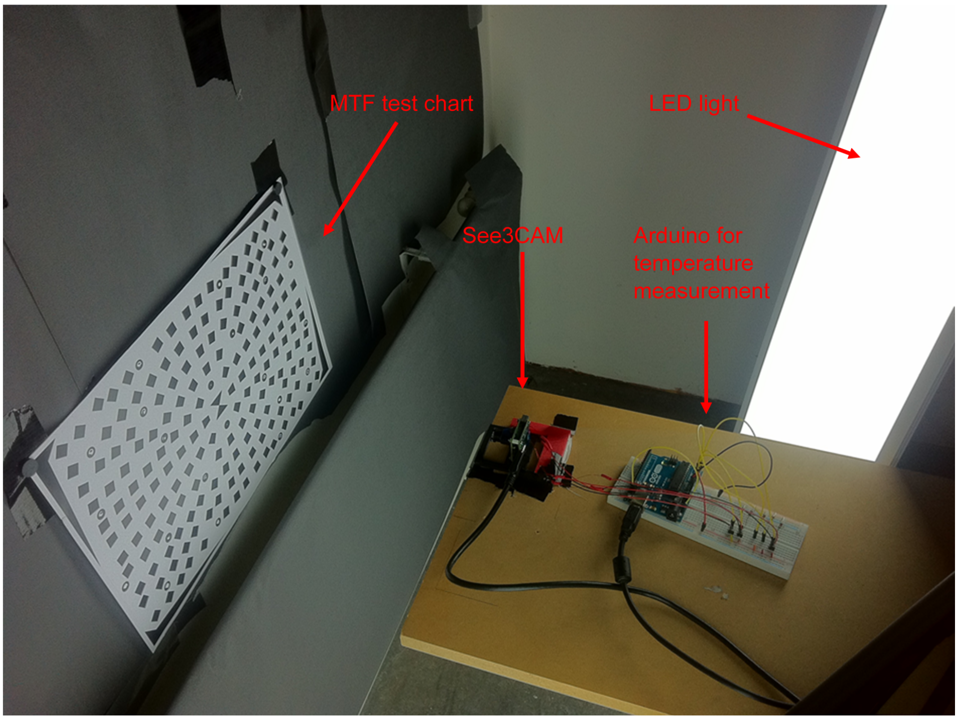

Figure 5.5: See3CAM in the performance test setup.

Modulation transfer function
During a performance test three separate images of the modulation transfer function (MTF) test chart are taken. The resulting images are analyzed using the open-source MTF Mapper software. This software has also been used to create the MTF chart. This chart includes fudicial markers which allows the software to automatically find and analyze the 700 slanted edges it contains. It outputs the MTF curves for both meridional and sagittal direction for slanted edges located near the top left corner and the center of the image. It also produces a chart showing the spatial frequency for the MTF_{50} values at every point of the test chart. For this it interpolates data between the different edges [43]. This software was verified using the ISO12233:2017 recommended sfr3mat implementation. The verification can be found in Appendix D.

Color distance
During the performance test three separate images are taken of the color chart. The images are analyzed using MatLab. The checkerboard pattern at the top of the chart allows for automatic detection of the 18 color patches. These patches form the regions of interest (ROI's) for the color analysis. For the analysis the average value of each of the rgb color channels for each ROI is determined. Using Equation (4.1) the distance between the color distance to a set of 18 reference values can be determined. During each performance test the color chart is imaged three times. The reference values are the rgb values for each ROI averaged over the three measurements during performance test I. For all subsequent performance tests the triplicate measurements were averaged and compared against the reference value from performance test I.

Signal to noise ratio
The signal to noise ratio (SNR) was measured using the grayscale patches located at the bottom of the color-chart. Using MatLab the 8 ROI's were located. For each of these ROI's, which increase in darkness from left to right, the standard deviation and mean were calculated for each of the rgb color channels. Using Equation (4.2) the signal to noise ratio was determined.

Distortion
Distortion was measured by first imaging the checkerboard chart thrice. Extra care was taken that for each performance test the checkerboard chart was placed in the same location. The imaged charts contain points in known locations. The distance, in pixels, between the middle and top right corner of the top right completely visible square was measured. Using Equation (4.3) the percentage distortion in the image based on a known undistorted reference was calculated.

Chromatic aberrations
The chromatic aberrations are also measured by imaging the checkerboard chart. Within the chart 5 regions of interest are analyzed. Each of these 5 ROI's contains an edge over which the edge spread function (ESF) was determined. The angle of the edge is first detected. If it is more than $0.2°$ the ESF is calculated by interleaving the data and applying Gaussian smoothing. If the angle is less than $0.2°$ the ESF is determined by calculating the average pixel value over the edge for ten edge crossings. This method was found to work well in practice.

Once the ESF had been determined the chromatic aberration was calculated by determining the maximum mean distance, in pixels, between two color channels with a pixel intensity between 0.4 and 0.7. That is, for each contrast level between 0.4 and 0.55 the distance in pixels between all three color channels are calculated. For each of these combinations (red-green, red-blue, blue-green) the average pixel distance is calculated where the maximum value represents the chromatic aberration along the edge.

Full well capacity
The full well capacity (FWC) was measured by imaging a uniform white background with increasing exposure times. The images were converted to grayscale images and the mean pixel value was calculated and plotted against the exposure time. This measurement is performed three times during a single performance test.

Average dark signal
While measuring the average dark signal all lights are turned off. The lens cap is placed on the lens and a cover is placed over the camera which is, in turn, covered by a cloth. All of this is to prevent light from reaching the photovoltaic sensor. Measuring the average dark signal is done by capturing a series of images with increasing exposure time. For each exposure time 10 images are taken and averaged to reduce the effects of thermal noise. The resulting image is converted to a grayscale image and the average pixel value is calculated. This is plotted against the exposure time. The average dark signal is measured three times during each performance test.

5.4. Thermal-ambient experiment

As explained in Section 2.4 the available vacuum-oven is not capable of cooling below room temperature. In order to expose the cameras to the expected low temperatures of $-5°C$ this thermal-ambient experiment was conducted. Because this experiment has been conducted in the physical setup of the performance test, described in Section 5.3.1, it was possible to take images of the color chart and to measure the average dark signal while the cameras were heated. This last experiment was repeated in the more controlled environment of the vacuum-oven (described in Section 5.6). Measurements were not conducted during the cold conditions because keeping the cameras at low temperatures for prolonged periods of time was not feasible in the setup.

5.4.1. Setup

In order to conduct this experiment the cameras were placed in the performance test setup. The cameras were heated to $50°C$ using a heat gun and cooled down to $-5°C$ using freeze-spray. Both were applied to the cameras from a distance of approximately 10 cm. The temperatures were measured using the Arduino controlled thermistors described in Appendix C. Both cameras were experimented on separately. During the test of a single camera two thermistors were attached to the camera and one thermistor was placed further apart to measure the surrounding air temperature. The cycle of heating up and cooling down was repeated four times. Table 5.4 shows the steps taken during each of these cycles.

Table 5.4: Steps taken during each of the different cycles of the thermal-ambient experiment. These steps were applied separately to both cameras.

Cycle	Notes
1	The camera was off during both the heating and cooling. After returning to room temperature the functionality of the camera was tested by turning it on and capturing an image..
2	The process was identical to cycle 1.
3	The camera was turned on and streaming continuously during both heating and cooling.
4	The camera was on and idle during heating. After both thermistors attached to the camera indicated a temperature above $50°C$ the average dark signal and full well capacity of the camera were measured.

5.4.2. Data gathering and analysis

During the experiment the temperatures of the cameras were continuously recorded. The experiment contained measurements also performed during the performance test. These measurements, consisting of images taken of the color chart and the measurement of the average dark signal, were analyzed using the method described in Section 5.3.2.

5.5. Thermal-vacuum experiment

The thermal-vacuum experiment was conducted to determine whether the cameras can survive the thermal-vacuum environment in space.

5.5.1. Setup

Thermal-vacuum testing was conducted in a Heraeus Vacutherm vacuum-oven capable of reaching an absolute pressure of $1 \cdot 10^{-1} mBar$. Both cameras were subjected to the experiment simultaneously. Temperatures were recorded during the entirety of the experiment. Test charts were setup in the appropriate locations for each camera. During the experiment the MTF test chart and the color chart were used. Figure 5.6 contains a schematic overview of the setup.

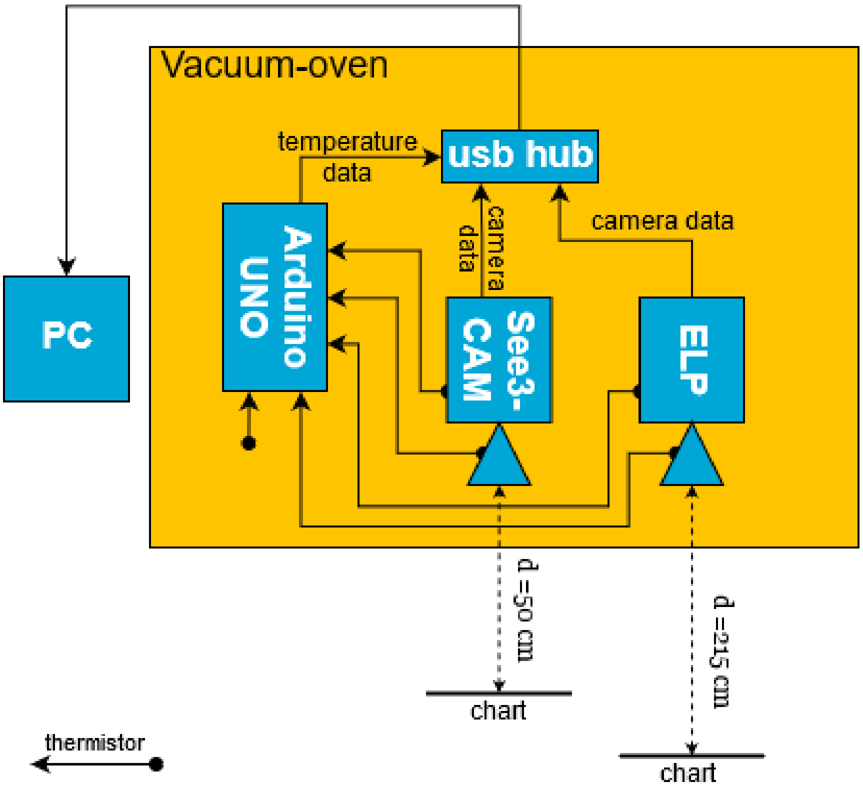

Figure 5.6: Schematic overview of thermal-vacuum experiment setup.

The vacuum-oven was located a room in which blinds could be lowered to cover all windows. For lighting the present overhead lighting was used. Because this is different from the lighting used during the performance test measurements taken during this experiment and the performance test cannot be compared directly.

Before and after the experiment the two pcb camera modules and the two lenses were weighed separately on a scale with a precision of $0.001g$.

Figure 5.7 contains an overview of the steps taken to conduct the experiment. It shows that the first step was to accurately measure the mass of the camera modules and lenses separately. After that the cameras were placed in the vacuum-oven and the door was closed. In this state the functionality of the cameras and the temperature sensors were verified. The temperature sensors were verified by recording their temperature and confirming it with a thermometer. The cameras were turned on using MatLab and reference images were taken of the color chart and MTF chart and a FWC measurement was conducted while imaging a white background.

During the next step the chamber was heated, under atmospheric pressure, to $50°C$ while the cameras were off. This step was conducted before bringing the chamber to a vacuum to reduce experiment time since it takes the chamber considerably longer to heat the cameras to $50°C$ while at low pressure. When this temperature was reached, as indicated by the vacuum-oven's internal thermometer and the 5 temperature sensors attached to the cameras images were again taken by both cameras of the MTF and color charts. A FWC measurement was also conducted.

After this step the cameras were again turned of and the chamber was brought to a pressure of $1.0 \cdot 10^{-1} mBar$ while maintaining the set temperature. This process took approximately 4.5 hours. After this the measurements of the color chart, MTF chart, and FWC were conducted. Additionally the cameras were set to stream data for 10 minutes continuously to measure the steady state temperature that they reached under these conditions.

In order to let the cameras and vacuum-oven cool down more efficiently the chamber was re-pressurized and opened. It was left to cool down with the door open for about 1 hour.

After the temperatures of the cameras and chamber had returned to room temperature the process of heating the chamber, bringing it to low pressure, and taking images was repeated in a similar time span.

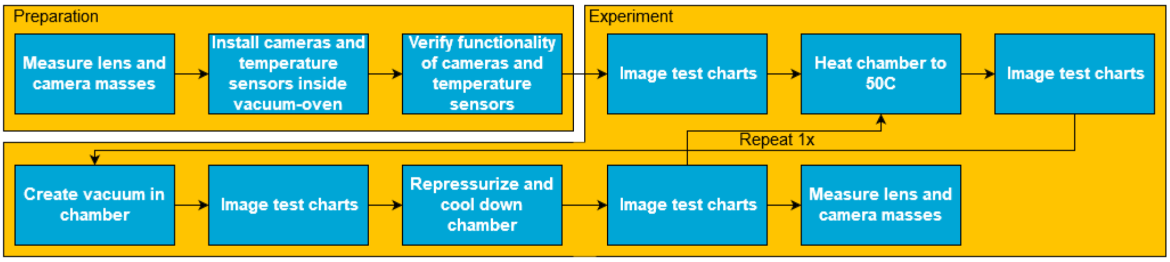

Figure 5.7: Overview of the steps taken to conduct the thermal-vacuum experiment.

5.5.2. Data gathering and analysis

The cameras were controlled using MatLab and the temperatures were recorded using the arduino Uno as described in Appendix C.

From the initial and final weighing of the cameras the total mass loss (TML) was calculated as the percentage change from the original mass. The measurements taken during the experiment consist of the images taken of the MTF and color test chart and the FWC measurement. Each measurement was conducted 10 times. The analysis of these images was conducted in a similar manner as described in Section 5.3.2.

5.6. Additional average dark signal measurement

During the thermal-ambient experiment the average dark signal was measured in hot conditions. That is, the average dark signal was measured while the camera was kept heated to approximately $50°C$. However, it proved difficult to accurately control the temperature of the camera using the heat gun. Thus, An additional average dark signal measurement was performed to measure the average dark signal in hot conditions. This test was performed after the thermal-vacuum experiment. This measurement was done inside the vacuum-oven under ambient pressure where the cameras were placed inside the oven with their lens caps on the lenses. A cover was placed in front of the glass door of the vacuum chamber as well as the windows of the room in which the vacuum-oven was located. In this setting the vacuum-oven was heated to $50°C$ after which the lights in the room were turned off and the cameras started measuring the average dark signal using the method described in Section 5.3.

5.7. Discussion

The methods and materials discussed in this chapter describe how the various experiments were conducted. The power measurement and duty cycle test were relatively straightforward measurements. The performance test is a bit more involved. It did show consistency over multiple measurements using the same cameras. However, an in depth verification of all techniques used to measure the metrics is, given the limited resources, beyond the scope of this thesis.

The vacuum-ovens inability to cool the chamber is another limitation imposed by circumstance. Although the thermal-ambient experiment is a suitable alternative heating the cameras using a heat-gun and, especially, cooling the cameras using freeze spray is less than ideal. This is because cooling the cameras to below $0°C$ in ambient conditions causes water to condensate on the cameras. Something which would not occur in space. Using this method it is also difficult to ensure a uniform camera temperature.

These limitations do not invalidate the experiments but do put a limit on how much the obtained results can be used to make generalized statements about the cameras. This is compounded by there only being two (different) cameras available for testing.

The next chapter deals with the practical execution of the experiments discussed in this chapter and talks about both issues encountered while conducting the experiment. It also presents the results of the experiments.

6

Results

In this chapter the results obtained during the experiments are discussed. The experiments are discussed in the order in which they were conducted starting with the power and integration time characterization in Section 6.1. After that the first performance test (Section 6.2), the thermal-ambient experiment (Section 6.3), the second performance test (Section 6.2), and the thermal-vacuum experiment (Section 6.5) are discussed. In Section 6.6 the results of the extra average dark signal measurements are discussed. Finally in Section 6.7 the results of the third performance test are discussed. This section ties the rest of the results together and presents a clear overview of how the performance of the cameras changed during the environmental tests. In Section 6.8 the results as a whole are discussed touching on the topic of what can be concluded from the results as well as what kinds of experiments are required to make broader and more generalized statements.

6.1. Power and integration time characterization

The first thing measured was the power consumption of the cameras. In idle mode the See3CAM was found to consume approximately 530 mW while the ELP consumed 280 mW. The power consumption was also measured while the cameras were streaming data. This was tested at various frame sizes (total number of pixels) and both with and without compression. It was found that for each setting the cameras operated at a fixed framerate. Lowering the framerate in a viewing application did not cause the camera to capture less frames and just resulted in the application displaying less frames. Figure 6.1 shows that the power is primarily influenced by whether the images are compressed. The ELP camera reached framerates up to 30 fps in most configurations while the largest uncompressed frames only reached about 10 fps. The See3CAM could reach 60 fps for smaller compressed frames. For the See3CAM streaming 2304x1536 uncompressed images was only possible at 5 fps.

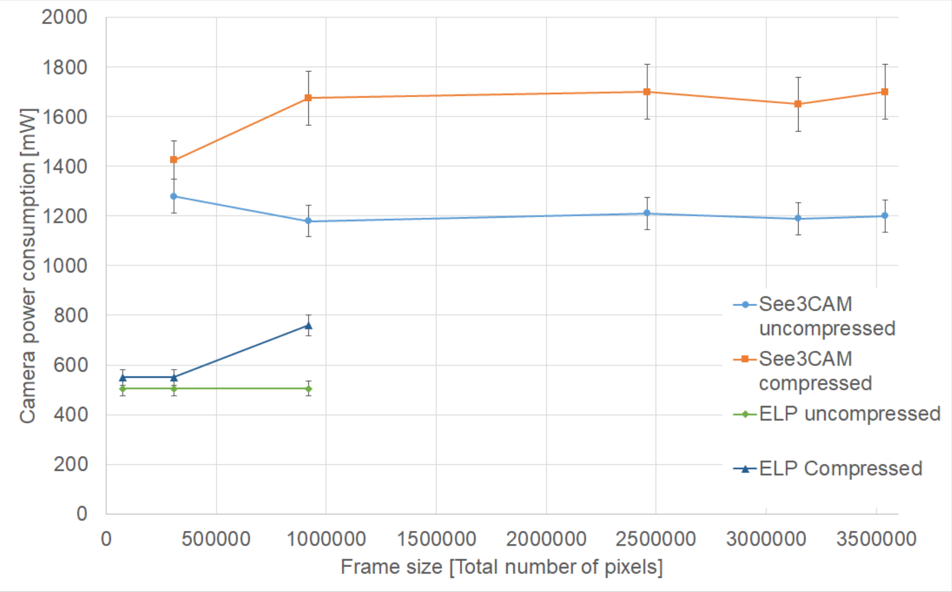

Figure 6.1: Power consumption of both the See3CAM and ELP cameras while streaming data in both compressed and uncompressed modes at maximum framerates.

The next step in this series of experiments was to determine the maximum framerate of both cameras by capturing a series of images as fast as possible one image at a time. Figure 6.2 shows the speeds achieved by both cameras.

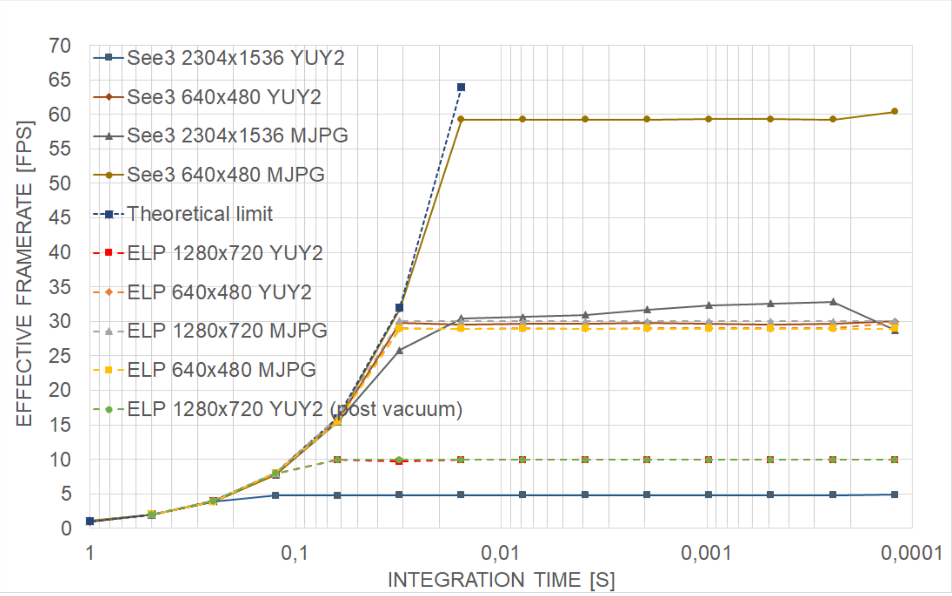

Figure 6.2: Maximum framerates achieved by the See3CAM and ELP in single image mode. MJPG and YUY2 indicate image encoding where YUY2 is uncompressed.

Note that that in Figure 6.2 the x-axis is reversed and to the left are the long exposure times. In the figure it can be observed that for long exposure times both cameras follow the theoretical limit (1/integration time) reasonably well. At various points the different variations on frame size and compression plateau and settle on a fixed framerate. These framerates are comparable to the ones achieved during streaming mode. In an equatorial orbit at an altitude of about 300 km a satellite has a ground track velocity of about 7.3 km/s. Table 6.1 shows the framerates and data rates for the See3CAM and ELP camera when operating as either a staring array or using time delayed integration (TDI). The staring array operates by taking an image of the entire field of view and waiting until the movement of the satellite brings a new area into view to image. TDI is a method that can be used to increase the signal by having each (cross-track) line of pixels overlap as they move over the same area. This does require very high framerates and causes the cameras to send significantly more data to the on-board computer. The data rates in Table 6.1 are calculated using the specified framerate and are based on full frame sizes (2304x1536 for the See3CAM and 1280x720 for the ELP) and 10 bit image depth without compression.

Table 6.1: Framerates and data rates for the See3CAM and ELP when operating as staring arrays or using TDI at various ground sampling distances.

	See3CAM			**ELP**		
GSD	20 m	40 m	250 m	20 m	40 m	250 m
Framerate (array)	0.24 fps	0.12 fps	0.02 fps	0.5 fps	0.25 fps	0.04 fps
Data rate (array)	8.4 Mbit/s	4.2 Mbit/s	0.7 Mbit/s	3.9 Mbit/s	2.0 Mbit/s	0.3 Mbit/s
Framerate (TDI)	363 fps	182 fps	29 fps	363 fps	182 fps	29 fps
Data rate (TDI)	12.8 Gbit/s	6.4 Gbit/s	1.0 Gbit/s	2.8 Gbit/s	1.4 Gbit/s	0.2 Gbit/s

Table 6.1 and Figure 6.2 show that the required framerates for both cameras to operate as staring arrays can be achieved easily. This is due to the fact that even for the ELP camera with only 1280x720 pixels and a GSD of 20 m the array would still be able to see 25.6 by 14.4 km. TDI only becomes possible for both cameras if the GSD is 250 m or larger. For the staring array implementation a delay needs to be introduced to wait for the movement of the satellite to bring a new area into view of the array. This is possible by introducing a delay between the taking of two images. It was found that the framerate could be reasonably well controlled to within 0.006 fps for both cameras using a delay. Table 6.2 lists the control accuracy for both cameras.

Table 6.2: Control accuracy for integration time of the See3CAM and ELP cameras.

Camera	Nominal framerate	Set framerate	Mean error (fps)	Error standard deviation (fps)
See3CAM	4.48	2	0.0036	0.0033
ELP	9.93	5	0.0056	0.0063

Where the mean error is calculated as the average absolute value of the achieved framerate minus the set framerate. The power consumption at various framerates is shown in Figure 6.3. The framerate was found to have no impact on the power consumption of the cameras.

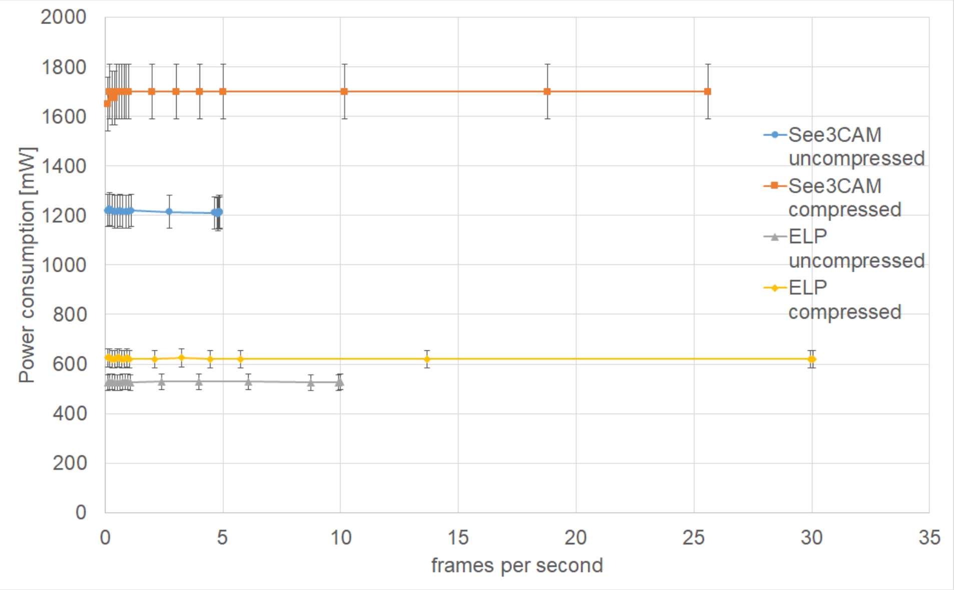

Figure 6.3: Power consumption of the See3CAM and ELP at various custom framerates with and without compression.

6.2. Performance test I

A first performance test was performed which forms a reference against which the performance tests conducted after the thermal-ambient and thermal-vacuum tests can be compared. The performance tests measure the modulation transfer function (MTF), full well capacity (FWC), average dark signal, color distance, distortion, and chromatic aberration. This performance tests already clearly shows some of the differences between the two cameras. When looking at the MTF the See3CAM achieves MTF50 values at spatial frequencies which are relatively uniform over the entire field of view (FOV) while the ELP has much more random variation throughout its FOV. This can be observed in Figure 6.4 which shows the spatial frequencies at which the modulation transfer function reaches a contrast of 50%. It can be observed that the FOV of the See3CAM is very uniform compared to the FOV of the ELP which shows some significant variation which appears to be random. Figure 6.4 shows the difference in MTF50 values measured along the sagittal edges (aligned with the top left to bottom right diagonal) of the MTF test chart. This behavior is similar when measured using the meridional edges (aligned with the top right and bottom left diagonal).

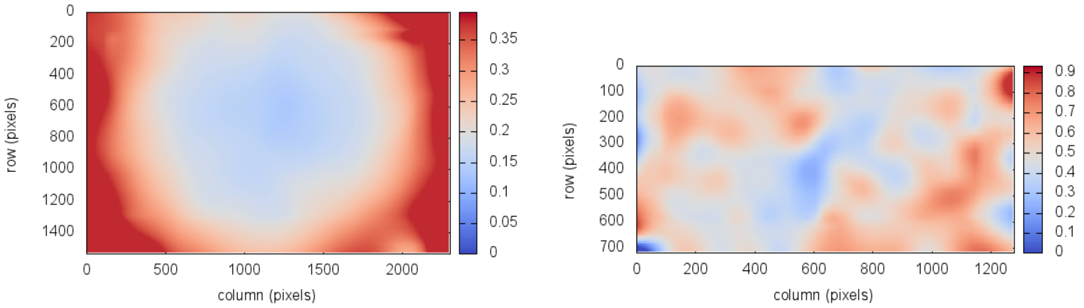

(a) SEE3CAM MTF50 spatial frequencies in sagittal direction.

(b) ELP MTF50 spatial frequencies in sagittal direction.

Figure 6.4: Figure showing at which spatial frequency, in cycles/pixel, the modulation transfer function reaches 50% contrast at every point in the cameras field of view.

The lenses on both cameras showed no significant chromatic aberrations. Interestingly, although the sharpening setting was set to its lowest value, 0, the ELP camera does show some evidence of edge sharpening. This is visible in Figure 6.5a where the edge is clearly brighter than the white area to the right of it. Figure 6.5b, which shows the edge spread function (ESF) over that edge, also shows this behavior clearly showing the significant increase in signal when moving from white (left) to black (right). This behavior is not seen in the images taken by the See3CAM.

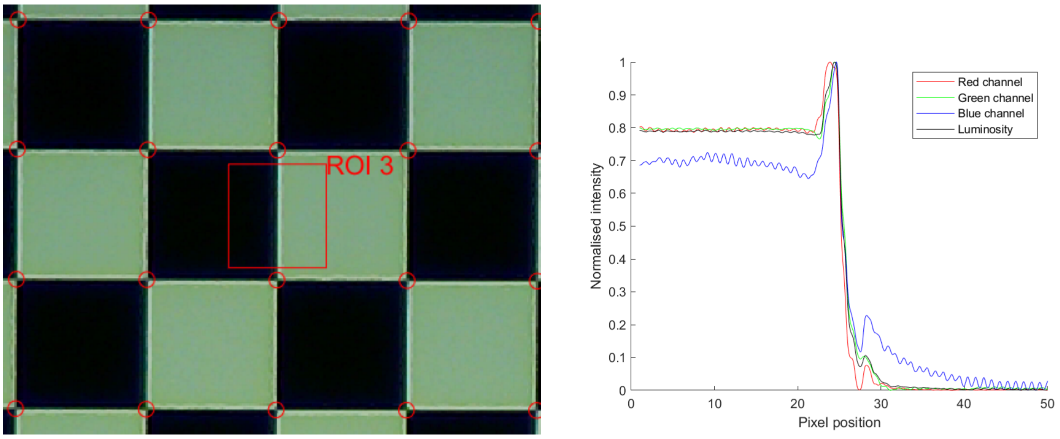

(a) Detailed view of the edge in region of interest 3 captured by the ELP camera of the checkerboard test chart.

(b) Edge spread function of the edge moving from white (left) to black (right).

Figure 6.5: Detailed view and edge spread function measured using the checkerboard chart by the ELP camera during performance test I.

In terms of distortion there is a large difference between the EO and WA lens. The EO lens measures no distortion while the WA lens, attached to the See3CAM, shows a negative (barrel) distortion of about -30%. Figure 6.6 shows the checkerboard chart as captured by both cameras.

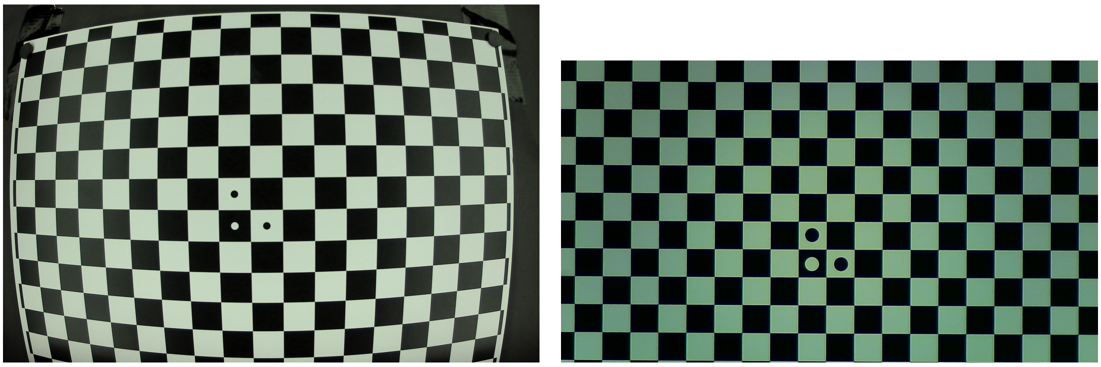

(a) The checkerboard chart as captured by the See3CAM showing a barrel distortion of about -30%.

(b) The checkerboard chart as captured by the ELP showing a negative (barrel) distortion of which the absolute value is < 1%.

Figure 6.6: The checkerboard charts as captured by both cameras showing the difference in distortion between the two cameras.

During this performance test the temperatures of both cameras were measured with thermistors attached to the lens and pcb. Figure 6.7 shows the recorded temperatures. During operation the See3CAM's pcb reached a maximum temperature of $37^{\circ}C$ while the ELP camera's pcb only reached $31^{\circ}C$. In the figure it can be observed that there is a sudden drop of about $5^{\circ}C$ in the temperature of the See3CAM's pcb likely caused by the thermistor detaching from the pcb.

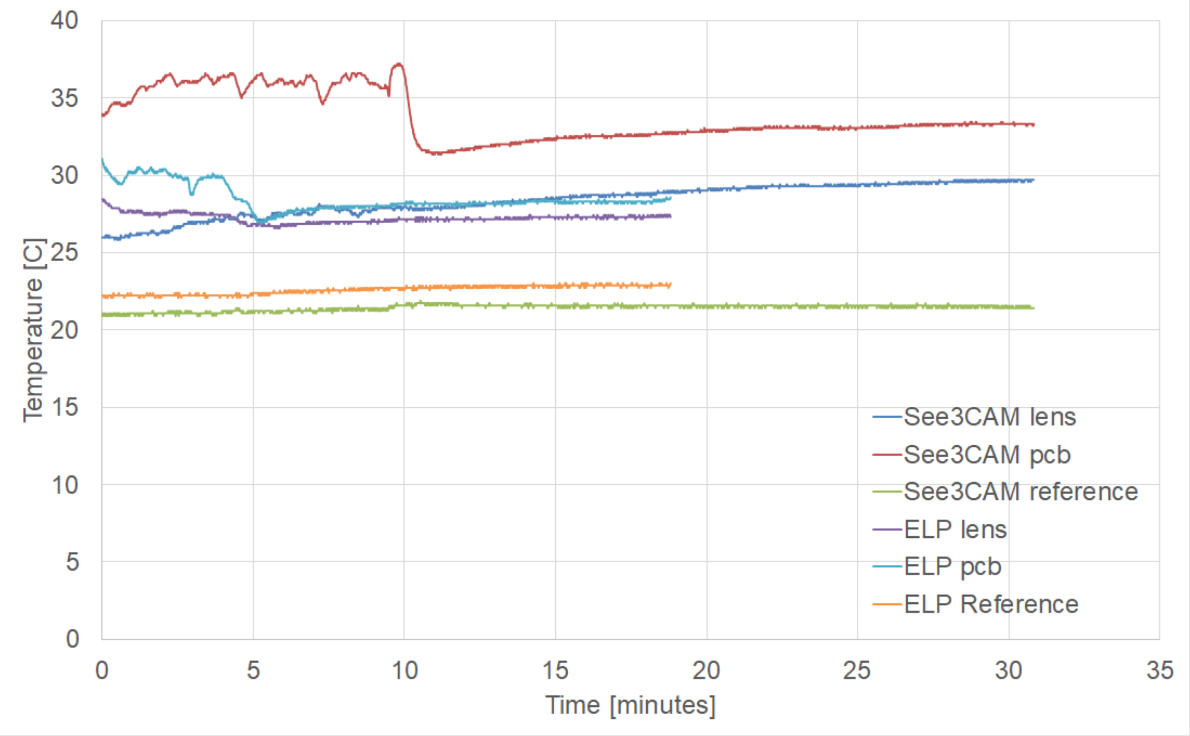

Figure 6.7: Temperatures of the See3CAM and ELP cameras measured during the first performance test.

6.3. Thermal-ambient experiment

The thermal-ambient test was conducted to observe whether the cameras would operate during hot and cold conditions under atmospheric pressure. The recorded temperatures of both cameras are shown in Figure 6.8.

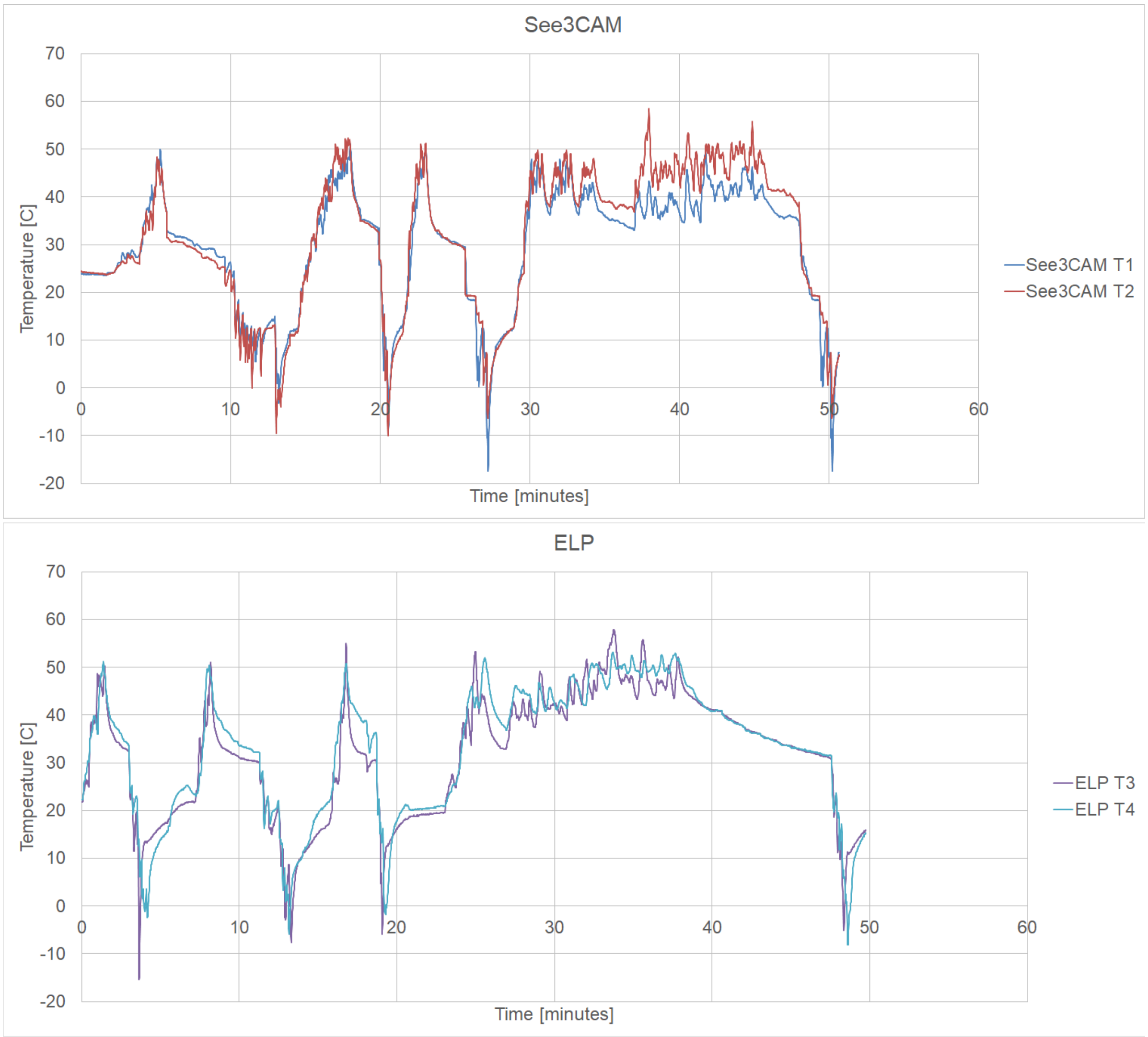

Figure 6.8: Temperature progression during the thermal-ambient experiment for the See3CAM (top) and ELP (bottom).

In these figures the four cycles of heating and cooling are clearly visible. No meaningful difference in temperatures are shown between the first two cycles and the third cycle during which the cameras were turned on. The fourth cycle lasts significantly longer due to the measurements of the average dark signal as well as images taken of the color test chart. During the experiments it proved difficult to accurately control the temperatures of the cameras. During the fourth cycle it can be seen the temperatures of both cameras never significantly exceeded $50°C$ and that the temperatures of the lens and pcb's typically did not differ by more than one or two degrees. This was unexpected since during the performance tests the camera pcb's consistently measured higher temperatures than the lens and were about $20°C$ warmer than the ambient temperature. This behavior is likely caused by the heat-gun. During the experiment air of about $50°C$ is blown pas the cameras which is suspected to cool the cameras when they exceed that temperature.

From the images of the color test chart any change in color representation as well as the signal to noise ratio (SNR) was determined. However, these metrics, as well as the average dark signal, shows no change compared to the same metrics measured during performance test I.

6.4. Performance test II

After the thermal-ambient test a second performance test was conducted. The results of this test are similar to the first performance test with one exception. The color representation of the See3CAM has changed slightly.

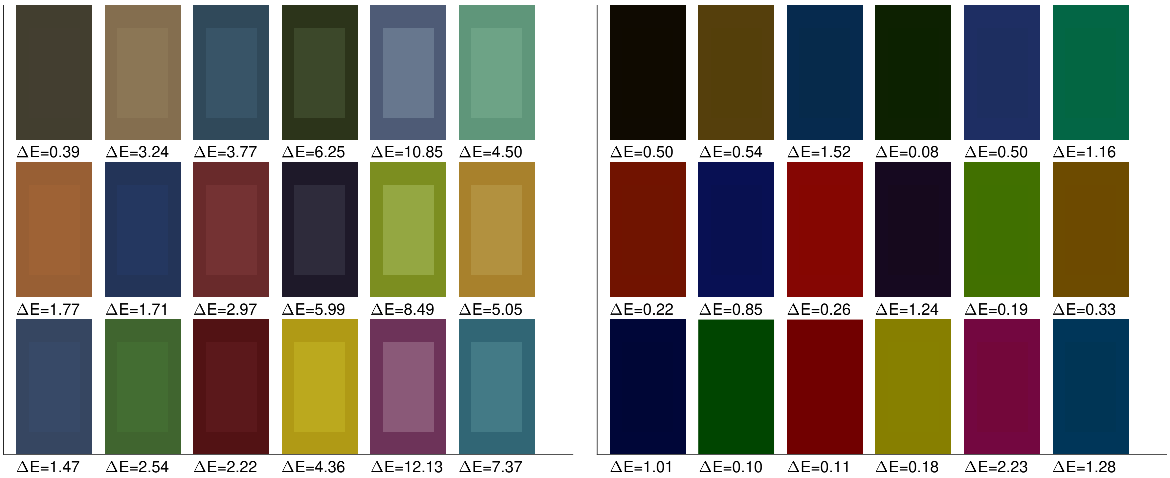

(a) Color patches captured by the See3CAM during performance test II.

(b) Color patches captured by the ELP during performance test II.

Figure 6.9: Color patches showing a slight change in the color representation of the See3CAM and no change in the color representation of the ELP camera.

Figure 6.9a shows the color patches captured by the See3CAM during the second performance test. This figure shows the same information both visually and quantified. The 18 colored squares correspond with the 18 squares on the color test chart in Figure 4.2. The outer boundary of each square is the reference color against which the inner square is compared. As can be seen for some colors the inner square is noticeably different indicating that the color capturing ability of the See3CAM has changed. This is illustrated by the ΔE color difference indicated between each of the 18 patches. The ΔE color difference is calculated taking into account human perception. Table 6.3 shows how these values roughly correspond to human perception.

Table 6.3: Method to interpret ΔE color differences [44].

Value	**Interpretation**
< 1	Imperceptible difference
1 - 2	Just noticeable difference
2 - 5	Easily noticeable difference
> 5	Large difference

The See3CAM showed an average ΔE of 4.7 while the ELP only had an average ΔE of 0.7. Figure 6.9 also shows a large differences between the colors captured with the See3CAM and with the ELP camera. However, this is due to the different settings of the two cameras.

6.5. Thermal-vacuum experiment

Before starting the thermal-vacuum experiment both the See3CAM and ELP cameras were placed inside the vacuum-oven and their functionality was checked with the door closed but the vacuum-oven otherwise turned off. Both cameras functioned normally and streamed data as well as took images of the MTF chart and color chart. The oven was turned on and set to reach $50°C$ after which the functionality of the cameras was again tested in a manner similar to before. However, During this test the See3CAM no longer functioned. The camera was still recognized by the pc as a usb camera but requesting image data continuously resulted in a time-out of the request. Because the experiment had already started and because troubleshooting the camera and restarting the 10+ hour experiment would mean it could not be completed that day it was decided to continue the experiment.

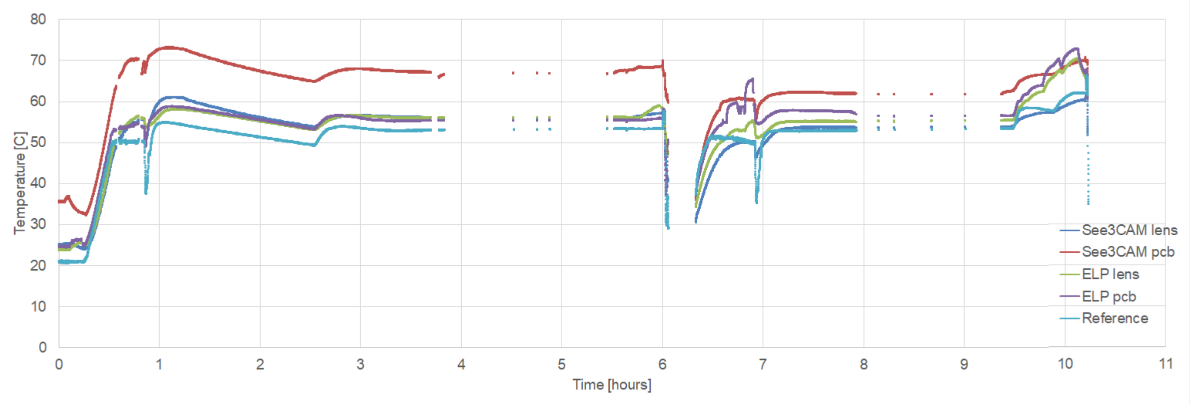

Figure 6.10: Temperatures recorded during the first two cycles of the thermal-vacuum experiment.

Figure 6.10 neatly shows all the different phases of the experiment. The first steep rise in the temperature graph indicates the oven heating up to $50°C$. The then sudden temperature drop is caused by the start of the vacuum pump after which air pressure rapidly drops inside the chamber. The expanding gas rapidly cools down after which the oven, detecting the sudden temperature decrease, starts heating again and overcompensates causing the overshoot. After seeing the overshoot the oven was set to a lower temperature allowing the oven to slowly cool down a little. After about 2.5 hours the temperature setting was again set to $50°C$ causing the oven to heat up to the desired temperature. All the while the vacuum pump was running. After 5.5 hours the vacuum-oven reached a pressure of $1.0 \cdot 10^{-1} mBar$ or one ten-thousandth normal atmospheric pressure. Once this pressure was reached the cameras captured images of the color and MTF test charts after which the oven was turned off and air was let back into the chamber rapidly cooling the cameras. The second cycle was conducted in much the same way with two exceptions. Before starting the vacuum pump the oven was set to a lower temperature which was raised slowly to prevent the overshoot that occurred during the first cycle. Also, before repressurizing the ELP was set to stream data for 10 minutes to allow it to reach a steady state temperature.

One final note about Figure 6.10 is that the temperature measurement of the See3CAM's pcb seems anomalous considering that the See3CAM was inoperable during the experiment. This might be just an erroneous temperature reading or the See3CAM, which was during the entirety of the experiment connected via usb, consumed a copious amount of energy.

Table 6.4: Results from the mass measurements before and after thermal-vacuum testing.

Item	Initial mass [g]	Final mass [g]	TML [g]	TML [%]
See3CAM module	11.964	11.934	0.030	0.25
ELP module	11.452	11.440	0.012	0.10
IC lens	29.615	29.570	0.045	0.15
WA lens	4.460	4.434	0.026	0.58

Before and after this experiment the masses of both cameras were measured to determine outgassing. Table 6.4 shows that both camera modules and both lenses (measured separately) lost less than 0.6% of their total initial mass. Considering that the pass criteria, set in Section 2.4, was set at $< 1\%$ it must be concluded that outgassing is not a concern for these specific cameras and lenses.

During the two cycles of the thermal-vacuum experiment the See3CAM did not function properly. After retrying to connect the camera a couple of times it started working again and the problem did not return. It is unknown what caused it. To gather data from the See3CAM in vacuum it was subjected to another cycle in the vacuum-oven. This time only the See3CAM was tested. During the experiment first a vacuum was created inside the chamber before heating. This proved a faster strategy for reaching a pressure of $1 \cdot 10^{-1} mBar$. The See3CAM consists of two pcb boards. During this test one of the thermistors was placed between the two pcb's and attached to the board containing the photovoltaic sensor. Figure 6.11 shows the recorded temperatures. During this test the thermistor between both pcb's recorded a temperature of $88°C$. Although this is high it does not appear to have influenced the camera negatively.

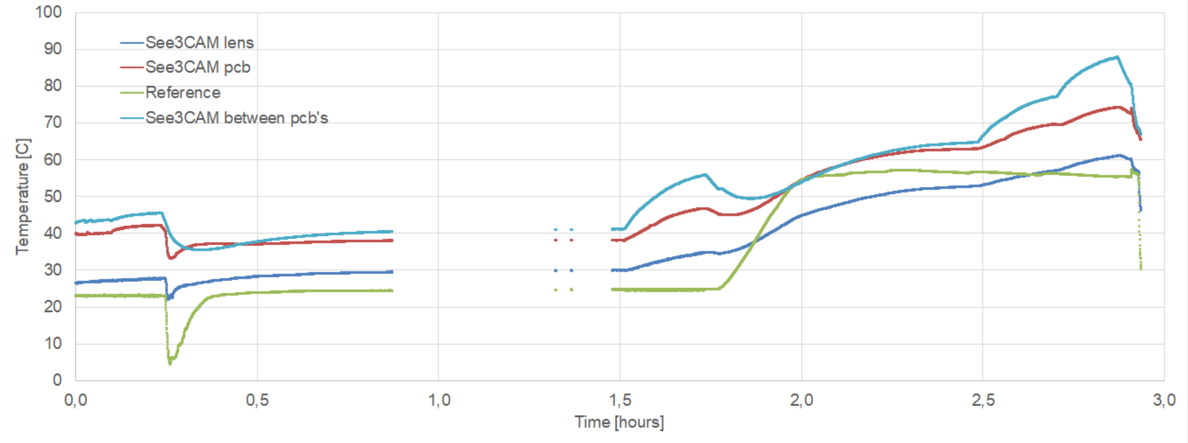

Figure 6.11: Temperatures of the See3CAM recorded during the second thermal-vacuum test.

6.6. Additional measurement of average dark signal

During the thermal-ambient experiment it proved difficult to reliably control the temperature of the camera for the duration of the measurements of the color chart and average dark signal. Especially for the average dark signal this could have a significant impact. For this reason the average dark signal of both cameras was again measured at an ambient temperature of $50°C$. This time this was done inside the vacuum-oven. Unfortunately a performance test was not conducted between this test and the thermal-vacuum experiment. This makes it difficult to say with certainty whether this experiment or the thermal-vacuum experiment had the largest effect on the cameras. The results of this test are interesting when viewed together with the third performance test. Therefore, they are discussed in Section 6.7 so as to not present them twice.

6.7. Performance test III

During the second performance test the See3CAM already showed some slight color change compared to the first performance test. During the third performance test this difference increased slightly with an average ΔE value of 4.9 compared to the 4.7 measured during performance test II. This change is caused by some color patches having a somewhat increased color distance and others a slightly decreased ΔE. For the ELP camera the difference is much larger with an average ΔE of 31.6. Figure 6.12 shows the results for both cameras during the third performance test.

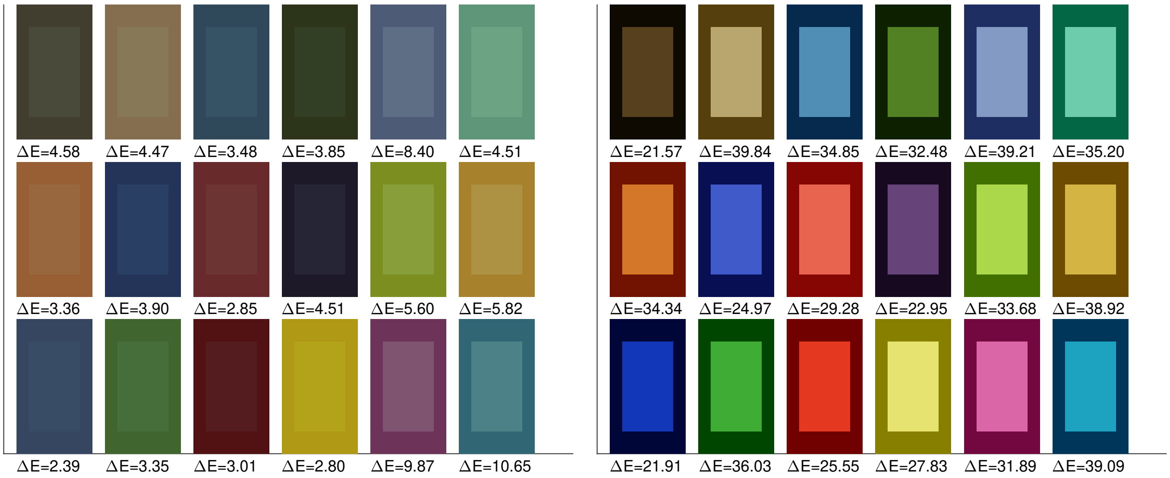

(a) Color patches captured by the See3CAM during performance test III.

(b) Color patches captured by the ELP during performance test III.

Figure 6.12: Color patches showing how color representation changed for both cameras between the first and third performance tests.

The large difference between the first and third performance test for the ELP is visible in almost all other metrics. Figure 6.13 show the full well capacities of the See3CAM and ELP as measured during each of the performance tests. It shows that the FWC has significantly changed for the ELP between the second and third performance test. What is interesting in this figure is that for all three performance tests of the ELP the three shortest integration times all receive the same amount of signal. This is strange because the average signal should increase with increasing integration time. What this suggests is that even before all the experiments the ELP camera was not capable of actually taking an image at the shortest exposure times and instead not being able to get shorter integration times than about 0.5 ms.

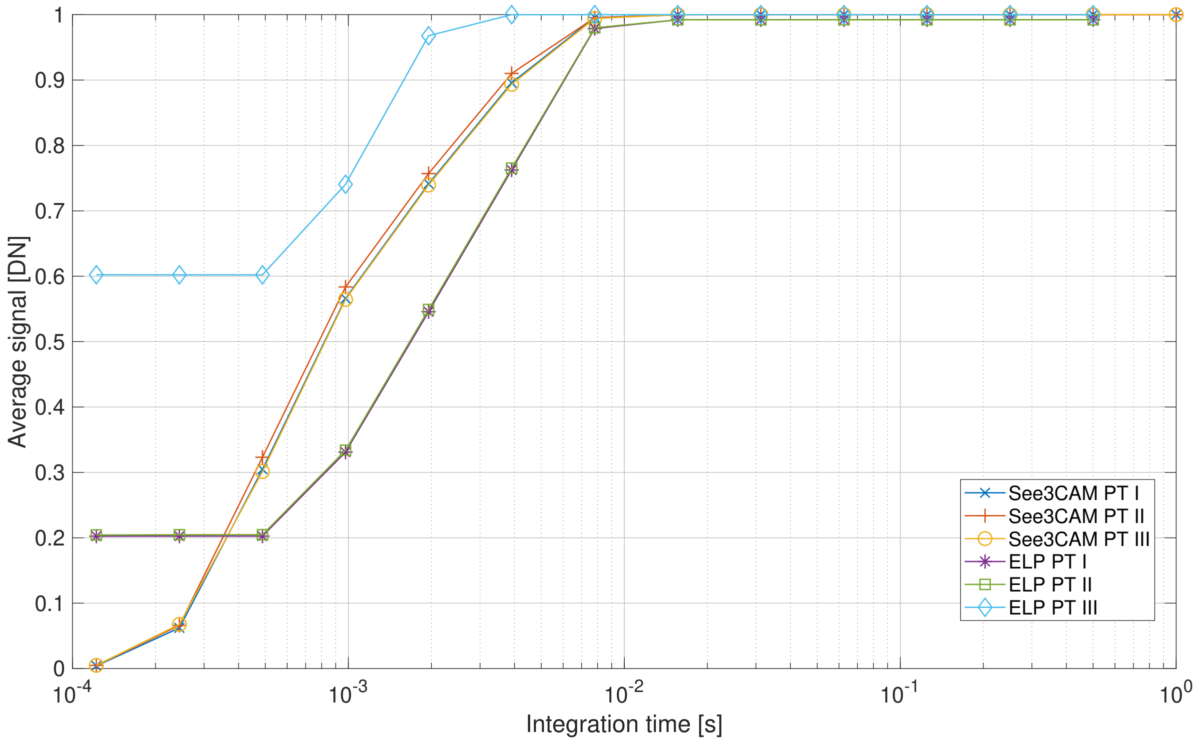

Figure 6.13: Results of the full well capacity measurements for both the ELP and See3CAM.

What seems to happen to the ELP is that for each measurement during the third performance test each image is overexposed. This is illustrated by Figure 6.14a and 6.14b which show the color test chart captured by the ELP camera in the same lighting conditions and with the same settings during the first and third performance test. This is a problem because it shows large changes in measurements which should otherwise be the same. A visual inspection of the ELP camera showed no signs of physical damage.

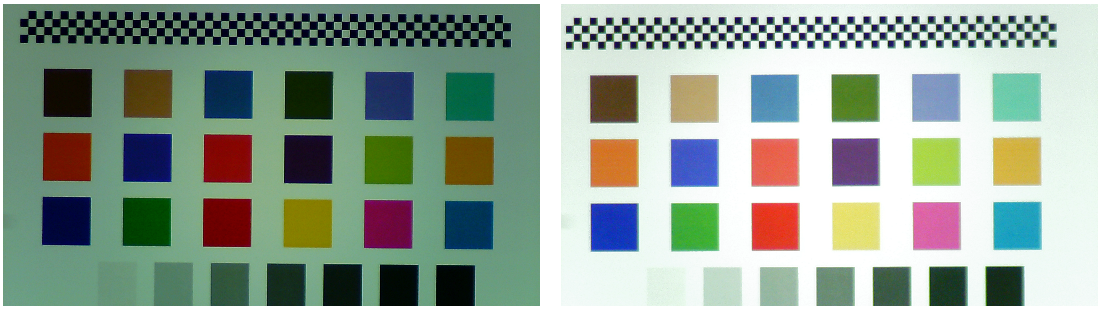

(a) Image of the color chart taken by the ELP camera during performance test I.

(b) Image of the color chart taken by the ELP camera during performance test III.

Figure 6.14: Comparison between images of the color chart taken during performance test I and III illustrating that the image taken PT III is over exposed.

Although no physical damage is visible something clearly changed in the behavior of the ELP camera. A cause for the observed change could be a defect in how the camera determines the correct integration time or an increase in noise.

Figure 6.15 shows the signal to noise ratio all three performance tests for both cameras. The figure also shows that the signal to noise ratio for the third ELP performance test is consistently about 10 dB larger than measured in the other two performance tests. Although a higher SNR seems like a good thing it indicates a negative change in the camera because it shows that the thermal-vacuum experiment has caused a significant change in the behavior of the camera. This makes, for example capturing ocean color data unreliable. The See3CAM shows no significant difference between each of the three tests. Note that the regions of interest on the x-axis refers to the grayscale patches on the bottom of the color test chart.

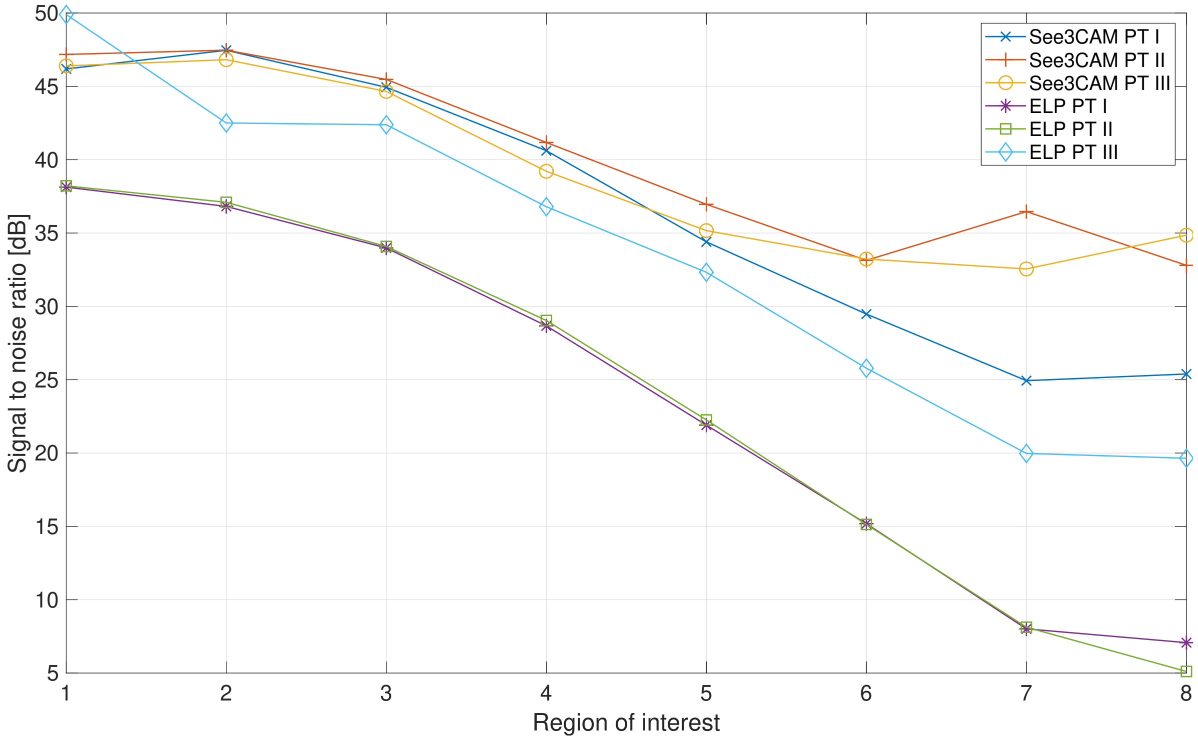

Figure 6.15: Signal to noise ratios measured during each of the three performance tests.

In Figure 6.16 the results of all the conducted average dark signal measurements are shown. What is interesting is that the results for the ELP PT III and the ELP additional dark signal measurement are significantly higher than the other measurements for the ELP. What is also interesting is the peak in average dark signal observed at short integration times for the See3CAM. Considering that it occurs during every measurement, even the measurement taking place inside the vacuum-oven, which was conducted in a very different setup, it must be caused by some aspect of the camera itself. The See3CAM has an attached led to its pcb which has been covered. However, the led is on continuously when it is measuring making it an unlikely candidate for the cause of this peak. The reason for this peak has not been determined.

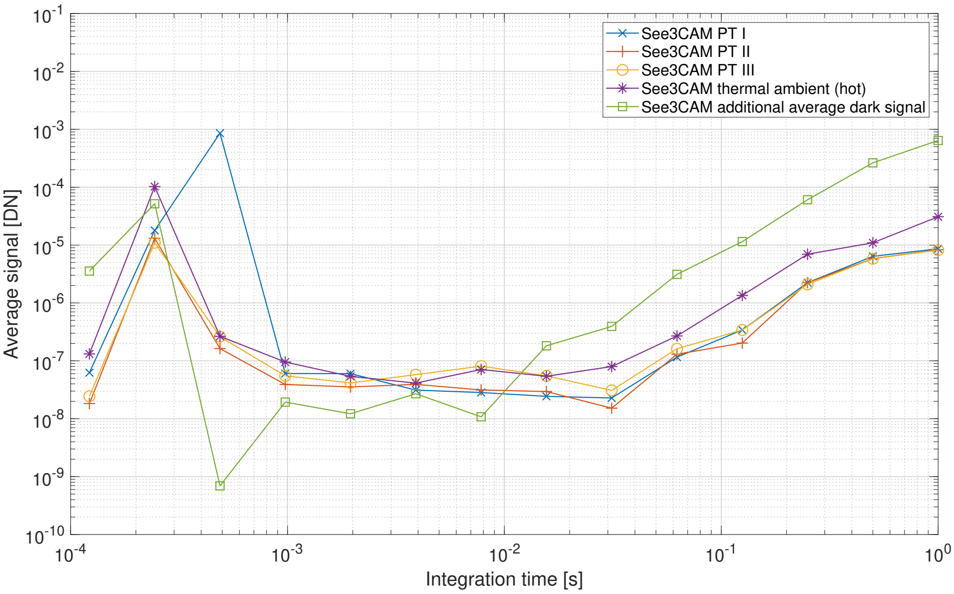

(a) Average dark signal measured for the See3CAM camera.

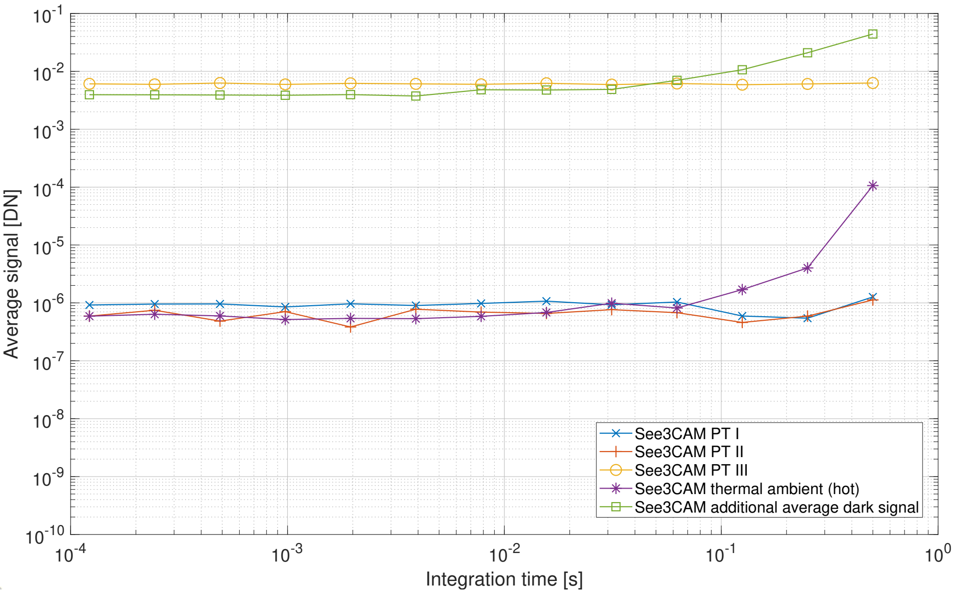

(b) Average dark signal measured for the ELP camera.

Figure 6.16: Average dark signal measurements taken during the performance tests, thermal-ambient test, and additional dark signal measurement.

Figure 6.16 shows that the noise for the ELP camera has increased with a factor of about 10^4 between the second and third performance test. The fact that the signal to noise ratio of the ELP camera also increased between the second and third performance test suggests that the method by which the SNR is calculated might not be the most suitable for determining changes in the SNR.

All the measurements discussed above involve the electronics of the cameras. The distortion and chromatic aberration metrics do not. In those metrics no significant difference between the first, second, and third performance test was measured.

Because the ELP appeared to show a problem with the integration time a small part of the duty cycle test from Section 6.1 was repeated. Interestingly, the calculated effective framerate, determine by the time it took to capture 50 images as fast as possible, has not changed as shown in Figure 6.17. The root mean square difference between this measurement taken before and after the environmental tests is merely 0.08 frames per second.

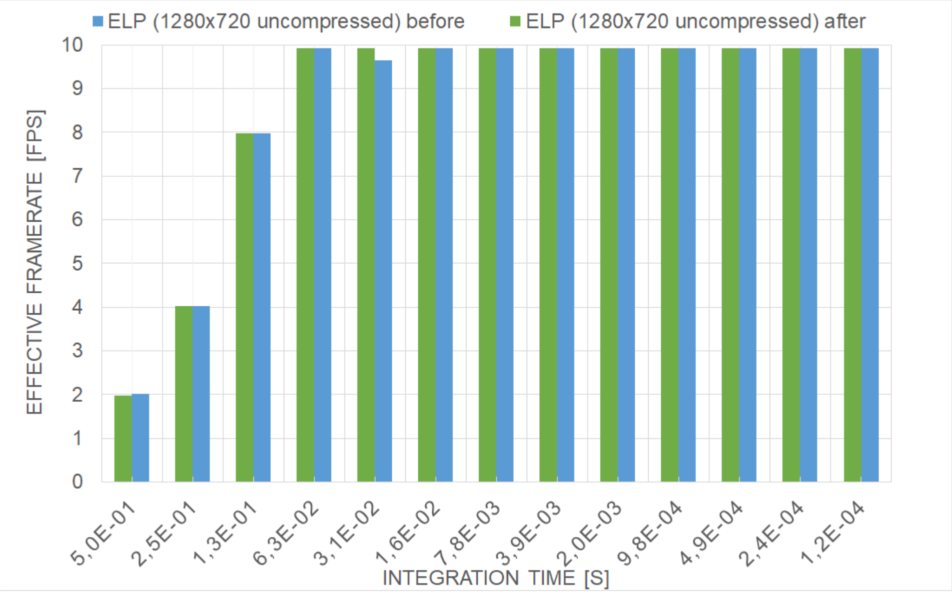

Figure 6.17: Comparison between the effective framerates achieved by the ELP camera (1280x720 uncompressed) before and after the thermal-vacuum and thermal-ambient experiments.

6.8. Discussion

There are some interesting conclusions that can be drawn from the results above. The measurements of the chromatic aberrations and distortion were an attempt to determine whether the environmental tests had an adverse effect on the lenses in particular. Considering that both those metrics showed no significant difference between each of the three performance tests it might be concluded that the thermal-ambient and thermal-vacuum environments did not influence the lenses. It must be noted that it is possible that the metrics were incapable or insufficient to detect negative changes in the lenses. However, considering that the lenses have not been subjected to unreasonable high temperatures, contain no electronically active or moving parts, and considering that neither the lenses nor the camera modules experienced any significant outgassing the probability that the lenses have been impacted in some undetected way must be considered low.

That the experiments have negatively impacted the ELP camera, on the other hand, has been clearly demonstrated. The measurements of the average dark signal and full well capacity all show that the camera somehow overexposes the images. The measurements of the average dark signal during the third performance test do show that the amount of noise captured by the camera has increased. However, This does not fully explain the behavior since the signal to noise ratio actually increased rather than decreased. This change in the SNR is, however, caused by the fact that the signal is increased by the overexposing of the image. This change in signal is negative since for consistent and reliable measurements the amount of signal received under similar conditions should be consistent. A hypothesis for what happened might be that, somehow, the integration times of the camera are longer than they should be. However, this would likely be visible in Figure 6.17. For now the exact reason for why the ELP camera appears to overexpose its images is unknown.

The performance tests have shown that the See3CAM also experienced some changes due to the environmental experiments albeit much smaller in scale than the ELP's changes. The only significant change was visible in the colors captured by the See3CAM. What is responsible for this change, in terms of components, is unknown. It is possible that it is a similar mechanism as with the ELP camera although on a much smaller scale. However, it should be noted that Figure 6.9 shows that not all colors are affected to a similar degree.

The experiments have demonstrated that the environmental conditions for which have been tested can have a serious impact on the performance of the camera. This impact is visible in both the ELP camera and, to a lesser extent, the See3CAM. Notwithstanding the environmental conditions for which no tests have been conducted, for example radiation or the mechanical loads during launch, there are several questions that must be answered before it can be determined whether or not the See3CAM would survive for any amount of time in space. The two most important of these are:

- Is the detected change specific to this See3CAM or does it also happen to other See3CAM cameras?
- Does the See3CAM's ability to capture color change further with repeated thermal cycling or does it remain constant after a number of cycles?

The first question must be answered to determine whether or not this test was a statistical anomaly. Maybe the tested See3CAM had some manufacturing flaw while other See3CAM's survive the experiments with no noticeable change. The opposite is also possible. Maybe this the tested See3CAM performed much better than other See3CAM's normally would. The second question provides insight in whether or not the See3CAM is usable with the changes. If after a certain number of cycles the color capturing ability stabilizes it is still a usable camera which just requires a bit of color correction. The two questions above are in line with a more engineering approach trying to determine if the See3CAM can be used in space or in a pocketqube specifically. A more scientific line also yields some interesting questions. What inside both cameras was influenced to have caused the observed behavior? What aspect of the environmental tests caused the change? The thermal cycling? The hot vacuum conditions? A combination of conditions? An investigation into this could allow one to make more generalized statements about the survivability of these cameras inside a vacuum while being heated or cooled.

7

Conclusion and future work

The objective of this thesis was to determine if commercial off the shelf cameras are suitable for use in pocketqubes and whether or not these cameras are capable of surviving space. In the literature study, summarized in Section 1.1, it is explained that these cameras can be useful if they are easy to integrate and if the application of the cameras relies heavily on a very high temporal resolution and thus requires a large constellation of pocketqubes. An example of such an application would be measuring ocean and lake color changes multiple times per day for biodiversity and environment monitoring. Section 3.3 shows that the expected signal to noise ratio of the cameras would be be about 16 dB. This is low, although perhaps not insurmountably so, considering that for such an application a signal to noise ratio between 20 and 50 dB is considered sufficient. A pocketqube has a very limited volume as well as limited available power for the payload and data downlink bandwidth. In Section 3.1 it is demonstrated that there is a large number of board level camera modules that fit the restricted volume. The exact application would determine whether or not the limited amount of available power and transmission bandwidth is sufficient.

The rest of the thesis aims to answer the question whether or not these cameras can survive space. A series of questions is given in Section 1.2 aimed at providing a clear path to answering that question. To answer these questions two cameras, the See3CAM_CU30 and ELP cameras, where tested.

R1.1 Which of the environmental conditions that a commercial off the shelf camera would experience can damage the camera?

Section 2.2 argues that during launch the accelerations and vibrations of the launch vehicle translate to the payload and can have a significant impact on the cameras. In Section 2.3 it is explained that when in space the thermal-vacuum environment can have a very large impact on the spacecraft and the camera. Apart from some components being susceptible to outgassing, the inefficient radiative heat transfer means that the cameras can reach high temperatures without being able to loose that heat efficiently. Section 2.3 also argues that atomic oxygen, present in low Earth orbit, might damage exterior surfaces such as the camera lens. The same is true for micro meteorites and other tiny pieces of debris. Finally it argues that radiation is capable of discoloring certain lenses or lens coatings as well as cause temporary or permanent damage to electronic components.

R1.2 With which metrics can the effects of the environmental tests on the cameras be quantified?

The metrics used to measure the effects of the experiments were the color distance, full well capacity (FWC), average dark signal, signal to noise ratio, distortion, chromatic aberration, and modulation transfer function (MTF).

The metric of color change was very effective in showing changes in the color representation for both cameras and was capable of both illustrating small and large differences. This color distance is calculated based on the ΔE_{2000} calculation the distance in color space between the a set of colors and a set of reference colors. For the reference colors the results from the first performance test was used. The full well capacity shows whether or not the signal increases linearly with the integration time and at which integration times image saturation is reached. The average dark signal is captured in as dark a situation as possible and is used as a measure of noise. The signal to noise ratio (SNR) is also a measurement of noise and, unlike the average dark signal, is calculated in relation to the received signal. These four metrics quantify changes in how the cameras electronically process the images. Changes in the optical part of the cameras are quantified by the distortion and chromatic aberration. The distortion is a measure of how much the image is distorted close to the edges compared to what is being imaged. High distortion typically results in slightly curved lines near the edges which are supposed to be straight. The chromatic aberration is a measure of how well a lens is capable of focusing light of different wavelengths at exactly the same point. A change in the distortion, chromatic aberration, or both would indicate a physical change inside a lens. Finally the MTF is a metric indicating how well contrast is transferred from the imaged scene, through the lens, to the photovoltaic sensor for every spatial frequency. This metric essentially aggregates the performance of all three into one metric. A change in the MTF indicates that something changed in either the imaged scene, the lens, or the camera module.

Apart from those metrics used to determine the performance of the cameras the total mass loss, the difference between initial and final mass before and after the thermal-vacuum experiment, was used as a metric for outgassing.

R1.3 What are the effects of the environmental tests on the selected cameras?

The thermal-vacuum experiment showed that neither the tested lenses nor the tested camera modules experienced any significant outgassing. The distortion and chromatic aberration metrics also showed that the performance of the lenses did not change during the thermal-vacuum and thermal-ambient experiments. For the See3CAM camera module the color distance metric showed that the color representation of the camera module changed slightly after both the thermal-ambient and thermal-vacuum test. However, this change was small, with an average ΔE of 4.7 after the thermal-ambient experiment and an average ΔE of 4.9 after the thermal-vacuum experiment. This change was only visible in the color distance metric. The SNR, FWC, and average dark signal showed no change.

For the ELP camera module no change was detected after the thermal-ambient experiment. However, after the thermal-vacuum experiment the camera still functioned but became unusable. The color distance showed an average ΔE of 31.6 which indicates a very significant change. This change was also visible in the full well capacity, average dark signal, signal to noise ratio, and modulation transfer function.

R1 Can commercial off the shelf cameras, that are fit for use in pocketqubes, survive the space environment?

Both cameras survived the thermal-ambient and thermal-vacuum experiments. That is, both cameras could still function and could still capture images. However, due to the experiments the color representation of the See3CAM changed. This change was small and if the changes do not continue the camera would still be usable. The ELP camera experienced such changes that it became, in terms of performance, unusable. The experiments conducted on these cameras indicate the necessity for environmental tests for such cameras. The fact that one camera became unusable also indicates that not all commercial off the shelf cameras can be used.

Unfortunately it is not possible to answer the research question definitively. One camera did survive the thermal-vacuum environment in a usable state. However, the mechanical environment during launch as well as other environmental factors, such as ionizing radiation, have not been experimentally tested. Nor have their effects been analyzed. This lack of tests/analysis is the main limitation of this study as well as the fact that only one of each camera (one See3CAM and one ELP camera) was tested. Based on the thermal-vacuum experiment, literature about the effect of ionizing radiation on cameras, and considering the fact that other cameras have successfully been launched there is an indication that there are commercial off the shelf cameras that could work in space in a pocketqube.

It is impossible to say whether the investigated class of 'plug-and-play' commercial off the shelf cameras generally works in space. This thesis has shown that both cameras probably will survive in space, at least for some time, but that both cameras also experience some negative changes in their performance. In the case of the ELP this change is large and in the case of the See3CAM this change is small. This thesis has been a first step in determining whether or not those cameras are suitable for use in space but more research is needed. For any specific application a new camera, complying with that application's requirement, will have to be selected. That camera would have to be subjected to experiments that have been both proposed in this thesis. However, this thesis does provide a framework that can be used as a starting point for testing those cameras. The method of performance tests described in this thesis can function as a basis for experiment conducted on similar cameras.

Future research and recommendations

As mentioned in Section 6.8 there are, generally speaking, two approaches to continue the research. A more scientific approach would entail repeating the experiments of this thesis with different cameras of the same type to determine whether or not the obtained results are statistically significant. A second approach would be more pragmatic and application oriented. In this approach a camera should be selected for integration into the Delfi-PQ or one of its successors. The aim of this would be to launch the camera and obtain in-situ data with and about the camera. There is a clear ordering in the next steps for such research as it would be prudent to subject the selected camera to environmental tests before integrating it with the pocketqube. These tests should, at least, include experiments subjecting the camera to a thermal-vacuum environment and the mechanical environment experienced during launch. The performance tests used in this thesis could be helpful when trying to quantify changes in the performance of this new camera. The following directions can be explored in future research.

- Perform an mechanical launch environment test on a camera intended for use in the Delfi-PQ as well as a thermal-vacuum test if the new camera is not the See3CAM_CU30.
- Integrate this camera with Delfi-PQ or one of its successors and subject the whole to qualification, acceptance, and pre-flight testing.
- Launch the camera as a demonstrator of the concept as well as an opportunity to investigate how the cameras behave over time while exposed to its environment.
- Investigate the economics and mission design of the topic. What would a detailed use-case look like? Who would use such a constellation? How many satellites would that need? What is the coverage and revisit time? What is an acceptable fault rate?

The following recommendations are made for those wanting to select a camera for further research or want to repeat the experiments in this thesis.

- Since the results of one camera do not necessarily provide any conclusions about different cameras it is recommended to keep a (type of) application in mind when selecting a camera.
- Select a camera that allows for sufficient control over basic functions. For example, during this thesis it was a hindrance that the maximum integration time was only 1 second or that for the ELP camera edge sharpening could not be turned off.
- If the lenses are not part of the experiments use appropriate lenses with minimal distortion and a relatively short focal length. Distortion makes analysis difficult and a long focal length means that the distance between the chart and camera can become somewhat large and cumbersome.
- Figure out a better method of measuring the signal to noise ratio of the cameras.
- Modify the thermal-ambient experiment. Preferably the thermal-vacuum experiment should include both a hot and cold conditions in vacuum. If that is not possible ensure at least that the cameras are inside a container which, as a whole is heated or cooled instead of exposing the cameras directly to hot air or cold gas.

Bibliography

[1] ESA/NASA. View of the netherlands seen from the international space station. `http://www.esa.int/ESA_Multimedia/Images/2006/08/View_of_the_Netherlands_seen_from_the_International_Space_Station`; [accessed 28-11-2019], 2006.

[2] Tony Reichhardt. The first photo from space. *Air & Space Magazine*, 2006. `https://www.airspacemag.com/space/the-first-photo-from-space-13721411/`; [accessed 18-11-2019].

[3] E. Kulu. Nanosatellite & cubesat database. `https://www.nanosats.eu/index.html#database`; [accessed 01-11-2019], 2019.

[4] Andres Klesh, Brian Clement, Cody Colley, John Essmiller, Daniel Forgette, Joel Krajewski, Anne Marinan, and Thomas Martin-Mur. Marco: Early operations of the first cubesats to mars. In *Small Satellite Conference*, volume 474 of *Delivering Mission Success*, 2018.

[5] R. Twiggs. Making it small, cal poly developers' workshop, san luis obispo, 2009.

[6] Silvana Radu, Sevket Uludag, Stefano Speretta, Jasper Bouwmeester, Eberhard Gill, and Nikitas Chronas Foteinakis. Delfi-pq: The first pocketqube of delft university of technology. In *Proceedings of 69th International Astronautical Congress*. International Astronautical Federation, IAF, 2018.

[7] David Barnhart and Martin Sweeting. Right-sizing small satellites. In *Proceedings of the 28th Annual AIAA/USU Conference on Small Satellites, 2014*, 2014.

[8] Jasper Bouwmeester, Silvana Radu, Sevket Uludag, Nikitas Chronas Foteinakis, Stefano Speretta, Alessandra Menicucci, and Eberhard Gill. Condititions and potential applications for pocketqubes. In *Proceedings Small Satellites, System & Services Symposium (4S)*, 2018.

[9] Claudia Kuenzer, Marco Ottinger, Martin Wegmann, Huadong Guo, Changlin Wang, Jianzhong Zhang, Stefan Dech, and Martin Wikelski. Earth observation satellite sensors for biodiversity monitoring: potentials and bottlenecks. *International Journal of Remote Sensing*, 35(18):6599–6647, 2014.

[10] Frank E Muller-Karger, Erin Hestir, Christiana Ade, Kevin Turpie, Dar A Roberts, David Siegel, Robert J Miller, David Humm, Noam Izenberg, Mary Keller, et al. Satellite sensor requirements for monitoring essential biodiversity variables of coastal ecosystems. *Ecological applications*, 28(3):749–760, 2018.

[11] ESA. nsight-1 cubesat mission in qb50 constellation; [accessed 01-11-2019], 2019.

[12] CubeSatShop. Scs gecko imager; [accessed 01-11-2019], 2019.

[13] Dee Pack, David Ardila, Eric Herman, Darren Rowen, Richard Welle, Sloane Wiktorowicz, and Bonnie Hattersley. Two aerospace corporation cubesat remote sensing imagers: Cumulos and r3. *31st Annual AIAA/USU Conference on Small Satellites*, 2017.

[14] Stefano Speretta, Tatiana Pérez Soriano, Jasper Bouwmeester, Johan Carvajal Godínez, Alessandra Menicucci, Trevor Watts, Prem Sundaramoorthy, Jian Guo, and Eberhard Gill. Cubesats to pocketqubes: Opportunities and challenges. In *Proceedings of the 67th International Astronautical Congress (IAC)*. IAF, 2016.

[15] Delft University of Technology. Delfi-pq website; [accessed 13-11-2019]. `https://www.tudelft.nl/lr/subsites/delfi-space/delfi-pq/`, 2019.

[16] Richard F Haines and Sherry L Chuang. The effects of video compression on acceptability of images for monitoring life sciences experiments. *NASA technical paper 8239*, 1992.

[17] Rocket Lab. *Electron Payload User's guide*, version 6.4 edition, jun 2019.

[18] Space X. *Falcon 9 Launch Vehicle Payload User's Guide*, revision 1 edition, oct 2008.

[19] Ariane Space. *Soyuz User's Manual*, issue 2 revision 0 edition, mar 2012.

[20] Ariane Space. *Vega User's Manual*, issue 4 revision 0 edition, apr 2014.

[21] European cooperation for space standardization. *Space engineering testing*. ESA-ESTEC requirements and standards division, ecss-e-10-03c edition, jun 2012.

[22] Peter Fortescue, Graham Swinerd, and John Stark. *Spacecraft systems engineering*. John Wiley & Sons, 2011.

[23] James R Wertz, David F Everett, and Jeffery J Puschell. *Space mission engineering: the new SMAD*. Microcosm Press, 2011.

[24] National Aeronautics and Space Administration. Low earth orbit spacecraft charging design handbook, nov 2018. NASA-HDBK-4006A.

[25] NASA Community Coordinated Modeling Center. Nrlmsise-00 atmosphere model. `https://ccmc.gsfc.nasa.gov/modelweb/models/nrlmsise00.php`; [accessed: 15-05-2019], 2019.

[26] R. Avila de Luis. Standardized thermal control solutions for pocketqubes. Master thesis, Delft University of Technology Faculty of Aerospace Engineering, 2019.

[27] Shinichi Kimura and Akira Miyasaka. Qualification tests of micro-camera modules for space applications. *Transactions of the Japan Society for Aeronautical and Space Sciences, Aerospace Technology Japan*, 9:15–20, 2011.

[28] Johan Fagerstrom. Ionizing radiation effects on image sensors. Master thesis, Lund University department of Electrical and Information Technology, jun 2016.

[29] VKI ISIS, MSSL. Qb50 system requirements and recommendations, jul 2014. Revision 6.

[30] Tom Markvart, Augustin McEvoy, and Luis Castaner. *Practical handbook of photovoltaics: fundamentals and applications*. Elsevier, 2003.

[31] Robert D Fiete and Theodore A Tantalo. Comparison of snr image quality metrics for remote sensing systems. *Optical Engineering*, 40, 2001.

[32] Raphael M Kudela, Stanford B Hooker, Henry F Houskeeper, and Meredith McPherson. The influence of signal to noise ratio of legacy airborne and satellite sensors for simulating next-generation coastal and inland water products. *Remote Sensing*, 11(18):2071, 2019.

[33] e-con Systems. *See3CAM CU30 Type-C Datasheet*, version 1.6 edition, aug 2018.

[34] Ailipu Technology. *ELP H264 HD 720p USB camera module datasheet*, 2018.

[35] Edmund Optics. 50.0mm fl, f/2.5 micro video lens specifications. `https://www.edmundoptics.com/p/500mm-fl-no-ir-cut-filter-f25-micro-video-lens/16455/`; [accessed: 29-01-2019], 2019.

[36] EN Manson, L Bambara, RA Nyaaba, JH Amuasi, JJ Flether, C Schandorf, and ASK Amable. Comparison of modulation transfer function measurements for assessing the performance of imaging systems. *MEDICAL PHYSICS*, 5(2), 2017.

[37] Hang Li, Changxiang Yan, and Jianbing Shao. Measurement of the modulation transfer function of infrared imaging system by modified slant edge method. *Journal of the Optical Society of Korea*, 20(3):381–388, 2016.

[38] Xujie Zhang, Tamar Kashti, Dror Kella, Tal Frank, Doron Shaked, Robert Ulichney, Mani Fischer, and Jan P Allebach. Measuring the modulation transfer function of image capture devices: what do the numbers really mean? In *Image Quality and System Performance IX*, volume 8293, page 829307. International Society for Optics and Photonics, 2012.

[39] Peter D Burns et al. Slanted-edge mtf for digital camera and scanner analysis. In *Is and Ts Pics Conference*, pages 135–138. SOCIETY FOR IMAGING SCIENCE & TECHNOLOGY, 2000.

[40] White paper. *Measurement of signal-to-noise ratio (SNR).* AXIS communications, 2016.

[41] Edmund Optics. Distortion. `https://www.edmundoptics.com/resources/application-notes/imaging/distortion/`; [accessed: 22-10-2019], 2019.

[42] USB Implementers Forum. Universal serial bus cables and connectors class document, aug 2007. Revision 2.0.

[43] Frans van den Bergh. *MTF Mapper user guide*, jul 2019.

[44] Gaurav Sharma, Wencheng Wu, and Edul N Dalal. The ciede2000 color-difference formula: Implementation notes, supplementary test data, and mathematical observations. *Color Research & Application: Endorsed by Inter-Society Color Council, The Colour Group (Great Britain), Canadian Society for Color, Color Science Association of Japan, Dutch Society for the Study of Color, The Swedish Colour Centre Foundation, Colour Society of Australia, Centre Français de la Couleur*, 30(1):21–30, 2005.

[45] SONY. Imx250llr/lqr, imx252llr/lqr. `https://www.sony-semicon.co.jp/products/common/pdf/IMX250_252_Flyer.pdf`; [accessed: 19-02-2019], 2019.

[46] Altavision. aca2440-75uc general specifications. `http://www.altavision.com.br/Arquivos/Basler/Datasheet/acA2440-75uc_Datasheet.pdf`; [accessed: 19-02-2019], 2019.

[47] Ming Ronnier Luo. Cie 2000 color difference formula: Ciede2000. In *9th Congress of the International Colour Association*, volume 4421, pages 554–559. International Society for Optics and Photonics, 2002.

[48] TKS. Ntc thermistor: Tts series epoxy bead type for temperature sensing/compensation. Datasheet, 2019.

[49] Kumaran Ramanathan and Bengt Danielsson. Principles and applications of thermal biosensors. *Biosensors and Bioelectronics*, 16(6):417–423, 2001.

[50] Parallax inc. Plx-daq. `https://www.parallax.com/downloads/plx-daq`; [accessed: 11-06-2019], 2019.

[51] International Organization for Standardization. Photography — electronic still picture imaging — resolution and spatial frequency responses. `https://www.iso.org/standard/71696.html`; [accessed: 26-03-2019], 2017. ISO standard no. 12233:2017.

[52] Society for imaging science and technology. Digital capture resolution measurements. `https://www.imaging.org/Site/IST/Standards/Digital_Camera_Resolution_Tools.aspx?WebsiteKey=6d978a6f-475d-46cc-bcf2-7a9e3d5f8f82&hkey=f9040928-44d3-411a-9594-98ee6fd81e69`; [accessed: 26-03-2019], 2019.

[53] Jack. Spatial resolution - mtf mapper vs sfrmat3. `https://www.strollswithmydog.com/mtf-mapper-vs-sfrmat3/`; [accessed 26-03-2019], 2015.

A

Signal to noise ratio calculation

The signal to noise calculation is calculated based on the Equation (3.5) which repeated here. However, the method of calculating the result differs slightly from just plugging in the numbers.

$$S = \frac{GSD^2 \Omega \pi t_i}{4E_f} \int_{\lambda_{min}}^{\lambda_{max}} \eta(\lambda) L_{target}(\lambda) \tau_{optics}(\lambda) \lambda d\lambda \tag{A.1}$$

The wavelength range only covers the visible part of the electromagnetic spectrum and ranges from 400 nm to 700 nm. Because the quantum efficiency ($\eta(\lambda)$) of every camera is not known at every wavelength it is assumed that it is constant for each color band (red, green, blue) and the same for every camera. The quantum efficiency (QE) is based on that for the Sony Pregius IMX250LLR/LQR. Details are listed in Table A.1.

Table A.1: Quantum efficiency details [45][46]

Channel	Wavelength range	Quantum efficiency (peak)
Blue	400 nm - 500 nm	0.61
Green	500 nm - 600 nm	0.7
Red	600 nm - 700 nm	0.55

The optical transmission factor ($\tau(\lambda)$) is also unknown. This value is assumed to be constant for all wavelengths and is set to 0.9.

The spectral radiance ($L_{target}(\lambda)$) is calculated as follows. The radiometric surface input is calculated based on the model in Figure A.1 provided by the thesis supervisor.

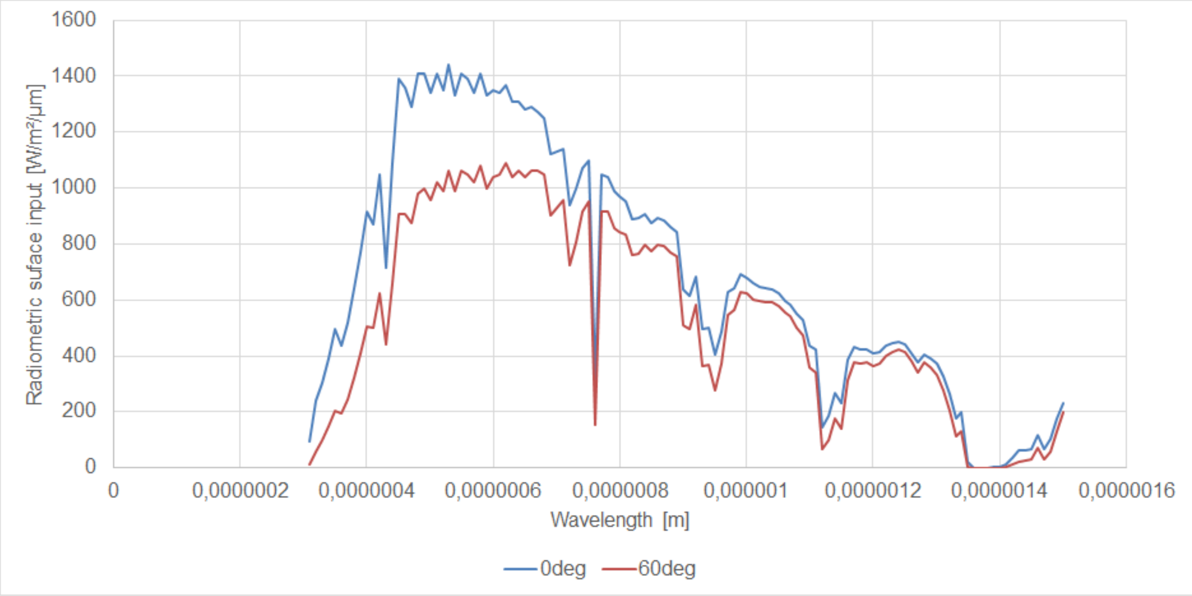

Figure A.1: Radiometric surface input model

For each color channel (red, green blue) the power of a Lambertian radiator is calculated by calculating the integral of the surface input (using a Riemann sum). The spectral radiance is then calculated using Equation (A.2).

$$R_{channel} = \frac{\alpha\rho}{\pi} \int_{channel} R_{surface} \tag{A.2}$$

Where $\int_{channel} R_{surface}$ is the Riemann sum over each color channel in the model in Figure A.1. α Is the albedo and ρ the atmospheric transmission factor. This last factor is assumed to be 0.7 and is only applied once because the model in Figure A.1 already accounts for one transmission through the atmosphere. The total signal is then given by Equation (A.3).

$$S = \frac{GSD^2 \Omega \pi t_i \tau}{4} \sum R_{channel} \eta_{channel} E_{f,channel} \tag{A.3}$$

The energy per photon (E_f), calculated for each channel, is calculated as follows.

$$E_f = \frac{h \cdot c}{\lambda_c} \tag{A.4}$$

Where h is the Planck constant, c is the speed of light, and λ_c is the center wavelength of the each channel.

The GSD (ground sampling distance) is already known for each camera and calculated using Equation (3.3). The solid angle (Ω) is calculated using Equation (A.5).

$$\Omega = \frac{A_d}{H^2} \tag{A.5}$$

Where A_d is the area of the camera aperture and H is the altitude of the satellite.

The integration time (t_i) in Equation (A.3) is set to 2^{-11} seconds. This value was chosen based an available integration time for most cameras (which are specified in negative powers of 2) and set in such a way that with a GSD of 60 m the pixel would move approximately 10% of the GSD during the integration time.

B

Color distance calculation

The calculation takes place in the hue, chroma, luminance space which can be calculated from the CIELAB color values ($L*, a*, b*$). These calculations are based on [44] and [47]. The parametric values K_C, K_H, and K_L were set to 1.

$$C_{i,ab}* = \sqrt{(a_i*)^2 + (b_i*)^2} \quad i = 1, 2 \tag{B.1}$$

$$\bar{C}_{ab}* = \frac{C_{1,ab}* + C_{2,ab}*}{2} \tag{B.2}$$

$$G = 0.5\left(1 + \sqrt{\frac{\bar{C}_{ab}*^7}{\bar{C}_{ab}*^7 + 25^7}}\right) \tag{B.3}$$

$$a_i' = (1 + G)a_i* \quad i = 1, 2 \tag{B.4}$$

$$h_i' = \begin{cases} 0 & b_i* = a_i' = 0 \\ \tan^{-1}(b_i*, a_i*) & otherwise \end{cases} \quad i = 1, 2 \tag{B.5}$$

$$\Delta L' = L_2* - L_1* \tag{B.6}$$

$$\Delta C' = C_2' - C_1' \tag{B.7}$$

$$\Delta h' = \begin{cases} 0 & C_1'C_2' = 0 \\ h_2' - h_1' & C_1'C_2' \neq 0; |h_2' - h_1'| \leq 180 \\ (h_2' - h_1') - 360 & C_1'C_2' \neq 0; (h_2' - h_1') > 180 \\ (h_2' - h_1') + 360 & C_1'C_2' \neq 0; (h_2' - h_1') < 180 \end{cases} \tag{B.8}$$

$$\Delta H' = 2\sqrt{C_1'C_2'}\sin\left(\frac{\Delta h'}{2}\right) \tag{B.9}$$

$$\bar{L}' = (L_1* + L_2*)/2 \tag{B.10}$$

$$\bar{C}' = (C_1' + C_2')/2 \tag{B.11}$$

$$\bar{h}' = \begin{cases} \frac{h_1'+h_2'}{2} & |h_1' - h_2'| \leq 180; C_1'C_2' \neq 0 \\ \frac{h_1'+h_2'+360}{2} & |h_1' - h_2'| > 180; (h_1' + h_2') < 360; C_1'C_2' \neq 0 \\ \frac{h_1'+h_2'-360}{2} & |h_1' - h_2'| > 180; (h_1' + h_2') \geq 360; C_1'C_2' \neq 0 \\ (h_1' + h_2') & C_1'C_2' = 0 \end{cases} \tag{B.12}$$

$$T = 1 - 0.17\cos(\bar{h}' - 30) + 0.24\cos(2\bar{h}') + 0.32\cos(3\bar{h}' + 6) - 0.2\cos(4\bar{h}' - 63) \tag{B.13}$$

$$\Delta\theta = 30\exp\left[-\left(\frac{\bar{h}' - 275}{25}\right)^2\right] \tag{B.14}$$

$$R_C = 2\sqrt{\frac{\bar{C}'^7}{\bar{C}'^7 + 25^7}} \tag{B.15}$$

$$S_L = 1 + \frac{0.015(\bar{L}' - 50)^2}{\sqrt{20 + (\bar{L}' - 50)^2}} \tag{B.16}$$

$$S_C = 1 + 0.045\bar{C}' \tag{B.17}$$

$$S_H = 1 + 0.015\bar{C}'T \tag{B.18}$$

$$R_T = -\sin(2\Delta\theta)R_C \tag{B.19}$$

$$\Delta E_{2000} = \sqrt{\left(\frac{\Delta L'}{K_L S_L}\right)^2 + \left(\frac{\Delta C'}{K_C S_C}\right)^2 + \left(\frac{\Delta H'}{K_H S_H}\right)^2 + R_T\left(\frac{\Delta C'}{K_C S_C}\right)\left(\frac{\Delta H'}{K_H S_H}\right)} \tag{B.20}$$

C

Temperature measurements

Temperatures were measured using the TKS TTS1A103F39H3RY NTC thermistor which has an operating temperature range between $-40^{\circ}C$ and $100^{\circ}C$ [48]. Five thermistors were used during the experiment were two were dedicated to each camera and a fifth was used for background temperature measurements. The thermistors were connected to an Arduino Uno to measure their output. Figure C.1 shows the circuit diagram.

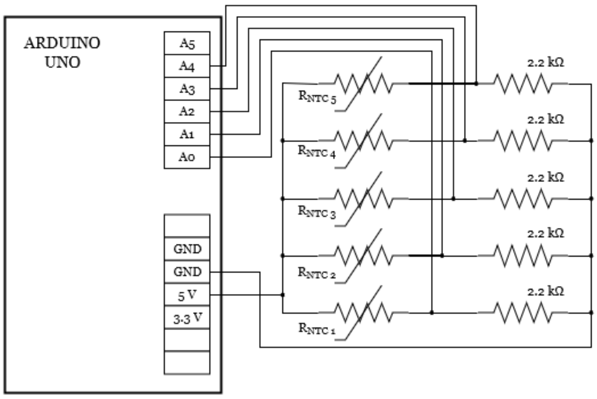

Figure C.1: Circuit diagram for temperature measurements

The Arduino measures the voltage (V_{out}) between the thermistor (R_{NTC}) and a known resistor (R_{bias}), for each of the thermistors. The resistance of the thermistor can be calculated using Equation C.1.

$$R_{NTC} = R_{bias}\left(\frac{V_{in}}{V_{out}} - 1\right) \tag{C.1}$$

Where $V_{in} = 5V$ and $R_{bias} = 2.2k\Omega$. From the calculated resistance the temperature can be calculated using the Steinhart-Hart equation given in Equation C.2 [49].

$$T = \frac{1}{C_1 + C_2 lnR_{NTC} + C_3(lnR_{NTC})^3} \tag{C.2}$$

Where C_n are the Steinhart-Hart coefficients which are derived from the temperature-resistance curve provided in the NTC's datasheet.

Table C.1: Steinhart-Hart coefficient values for the TKS TTS1A103F39H3RY NTC thermistor [48]

Coefficient	**Value**
C_1	$1.232808079 \cdot 10^{-3}$
C_2	$2.155052741 \cdot 10^{-4}$
C_3	$1.744893596 \cdot 10^{-7}$

The temperatures measured by the arduino are read via a PC serial port directly into Excel using the Parallax PLX-DAQ Excel software plugin. This has the advantage of enabling the use of the PC’s clock for timekeeping [50]. The temperature measurements are performed at 1 Hz.

D

Performance test setup verification

Because there are no calibrated cameras available for verification the process of verification of this thesis' performance test, discussed in Section 5.3, consists of the following items. A demonstration that the data that is retrieved from the camera images is retrieved from the correct location in the image. A demonstration that the performance test measurements are conistent. A verification of the validity of MTF Mapper based. Most data that is used here comes from the first performance test. The reason for this is that experiments conducted prior to the first performance test are not comparable to it because camera settings changed before settling on the values used during performance test I.

D.1. Image processing

The analysis of the performance test consists of processing and analyzing images taken during that test. With all three test charts it is important that the right parts of the image are analyzed. The MTF chart contains fiducials which are automatically recognized by MTF Mapper. Figure D.1 shows two images captured with the ELP and See3CAM during the first performance test. Shown in this image are the MTF_{50} values as detected by MTF Mapper showing that it correctly detects all the slanted edges which are fully within the image.

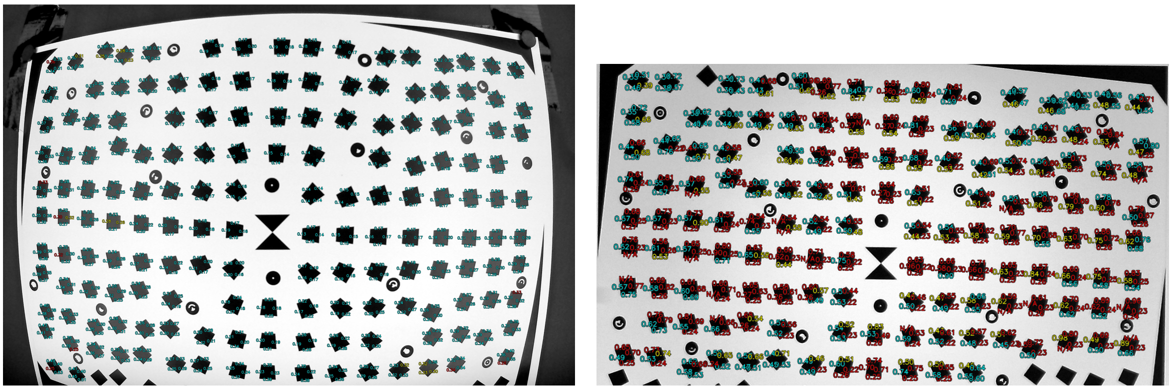

(a) Image of the MTF chart captured by the See3CAM during the first performance test.

(b) Image of the MTF chart captured by the ELP during the first performance test.

Figure D.1: Images of the MTF chart, captured during the first performance test, showing the MTF50 value at detected edges. Value color represents the quality of the data.

The color of the value indicates the quality of the data (blue is good, yellow is acceptable, and red is bad). This is influenced by the length of the edge (in pixels) and the angle of the edge. Figure D.1 shows that the images are processed correctly, even if they include significant distortion. No wrong edges are detected and only partially visible squares near the edge of the image are ignored. This is similar for all captures MTF images.

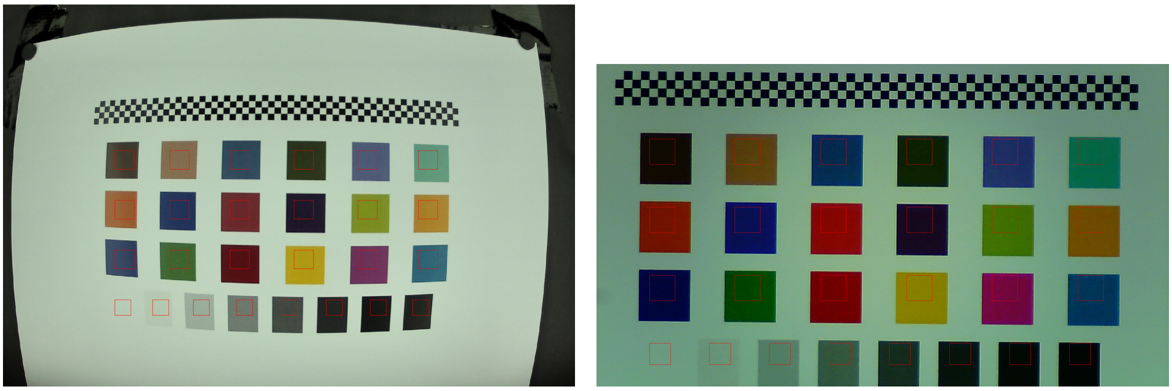

(a) Image of the color chart captured by the See3CAM during the first performance test.

(b) Image of the color chart captured by the ELP during the first performance test.

Figure D.2: Images of the color chart, captured during first the performance test, showing ROI boxes within which data is collected for further analysis.

The red boxes in Figure D.2a and D.2b indicate the areas in which data is gathered for the calculation of the color distance and for the calculation of the signal to noise ratio. Both figures show that each of the regions of interest only capture data from within a square of a specific color. That is, no white background from in between the squares is processed as if it where part of a colored (or black/white) square. This is similarly the case in all other color chart images.

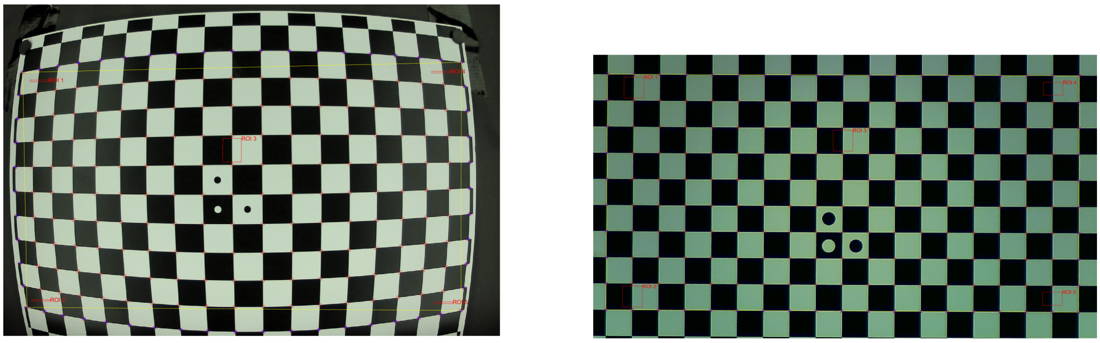

(a) Image of the checkerboard chart captured by the See3CAM during the first performance test.

(b) Image of the checkerboard chart captured by the ELP during the first performance test.

Figure D.3: Images of the checkerboard chart, captured during the first performance test, showing ROI boxes within which the chromatic aberration is calculated.

In Figure D.3 the five regions of interest are indicated in which the edge spread function is calculated (from which the chromatic aberration is determined). The figures demonstrate that the processed areas only include one edge both vertically and horizontally. The difference in height in the ROI's is due to whether the data can be interleaved (small box) or not (large box). In the figure the corners of the checkerboard pattern are also indicated showing that those are detected correctly. These are used for the calculation of the distortion. This is similar for all analyzed checkerboard chart images.

D.2. Consistency

The consistency of the measurements is checked in two ways. First it is demonstrated that multiple identical measurements, taken during the same performance test, are consistent. Then it is demonstrated that multiple measurements taken over two days are consistent. Only the results for the See3CAM are shown here. However, the results for the ELP camera are identical.

During each performance test three images are taken of each test chart. Similarly the full well capacity (FWC) is measured thrice. Below are the three results as measured during the first performance test for the See3CAM. They show no significant difference.

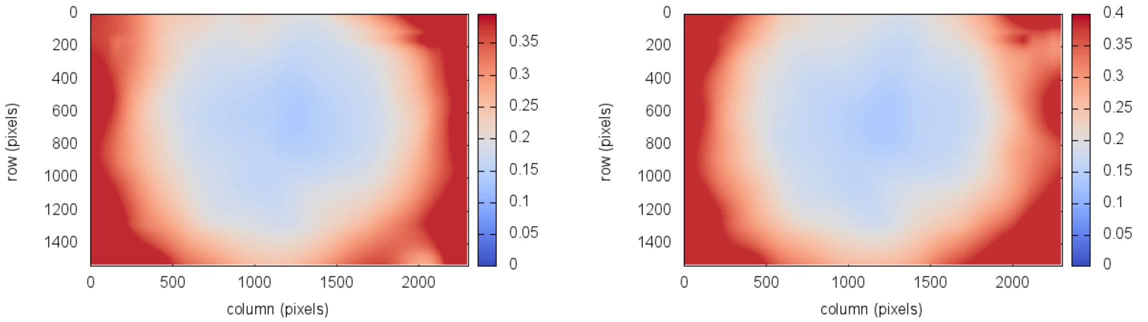

(a) First measurement of the MTF50 values in sagittal direction.

(b) Second measurement of the MTF50 values in sagittal direction.

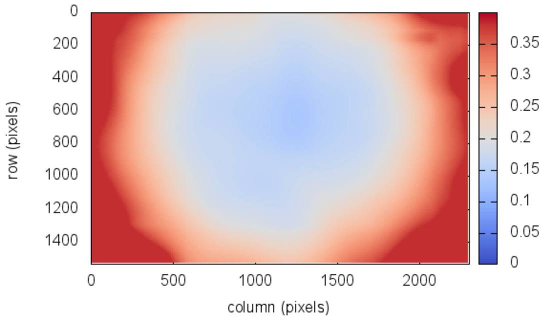

(c) Third measurement of the MTF50 values in sagittal direction.

Figure D.4: Comparison of the sagittal MTF measurements for the See3CAM during performance test I.

For the chromatic aberrations the edge spread functions of ROI 1 (see Figure D.3a) are shown. They again show no significant difference.

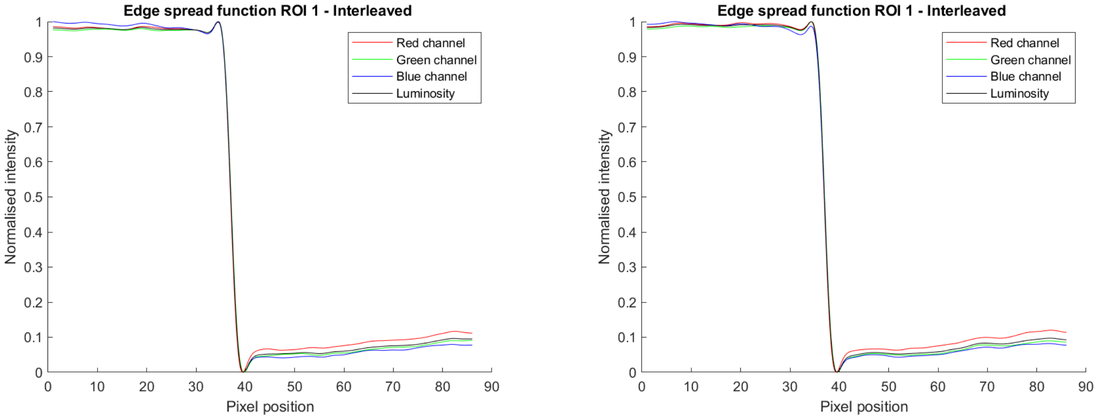

(a) First measurement of the edge spread function of ROI 1.

(b) Second measurement of the edge spread function of ROI 1.

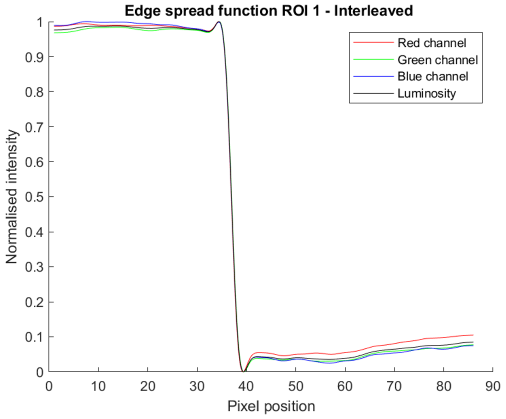

(c) Third measurement of the edge spread function of ROI 1.

Figure D.5: Comparison of the edge spread functions of ROI 1 imaged with the See3CAM during the first performance test.

Figure D.6 and D.7 show the three measurements of the full well capacity and signal to noise ratio again showing consistent measurements.

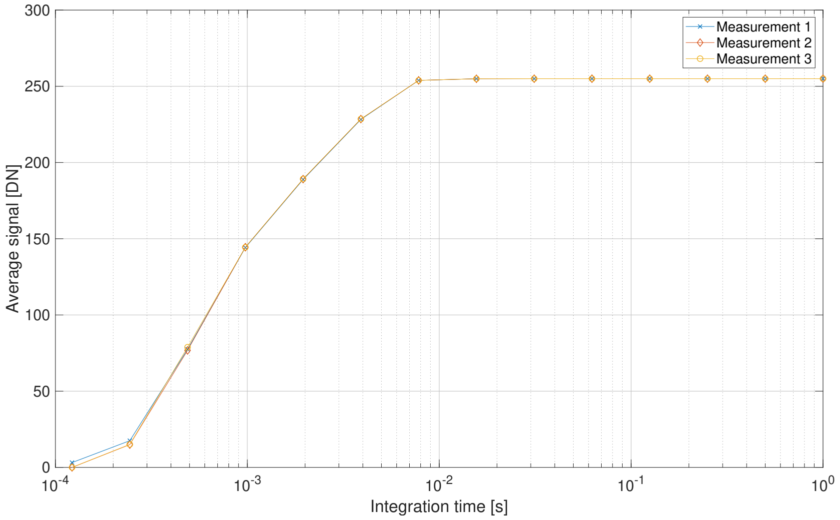

Figure D.6: Full well capacity of the See3CAM measured during the first performance test.

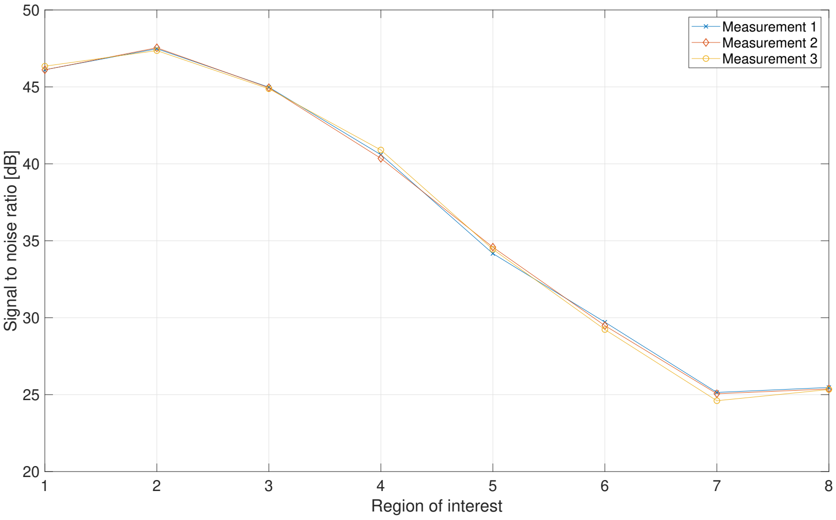

Figure D.7: Signal to noise ratio of the See3CAM measured during the first performance test.

Table D.1 shows the consistency of the distortion measurements for the See3CAM and ELP camera.

Table D.1: Distortion measured during the first performance test of the See3CAM.

Measurement	See3CAM	ELP
Measurement 1	-0.3043	-0.0093
Measurement 2	-0.3053	-0.0093
Measurement 3	-0.3046	-0.0092

Figure D.8 shows the color changes from the See3CAM performance test 1 compared to the average color value of each region of interest. Figure D.9 shows the same for the ELP camera. The See3CAM measurements have a standard deviation of 0.04 and the ELP measurement of 0.06.

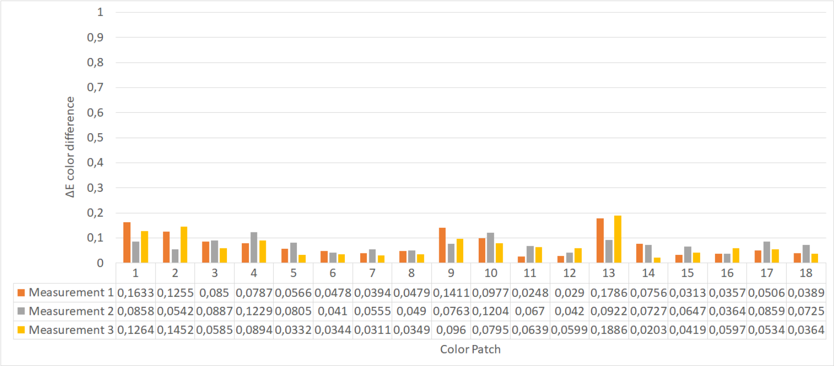

	1	2	3	4	5	6	7	8	9	10	11	12	13	14	15	16	17	18
Measurement 1	0,1633	0,1255	0,085	0,0787	0,0566	0,0478	0,0394	0,0479	0,1411	0,0977	0,0248	0,029	0,1786	0,0756	0,0313	0,0357	0,0506	0,0389
Measurement 2	0,0858	0,0542	0,0887	0,1229	0,0805	0,041	0,0555	0,049	0,0763	0,1204	0,067	0,042	0,0922	0,0727	0,0647	0,0364	0,0859	0,0725
Measurement 3	0,1264	0,1452	0,0585	0,0894	0,0332	0,0344	0,0311	0,0349	0,096	0,0795	0,0639	0,0599	0,1886	0,0203	0,0419	0,0597	0,0534	0,0364

Figure D.8: ΔE color distance spread during performance test I for the See3CAM.

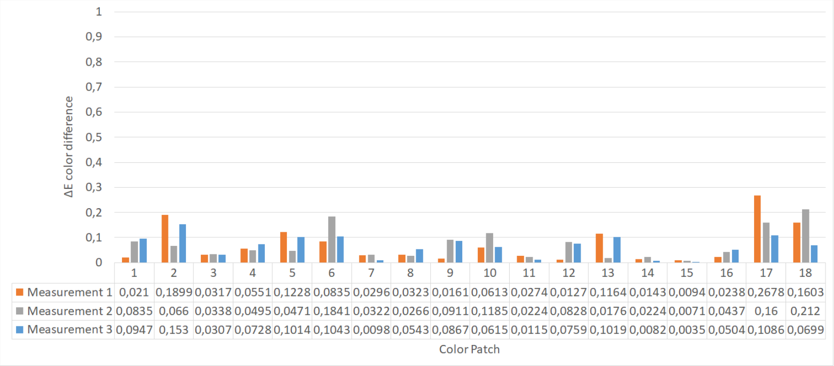

Figure D.9: ΔE color distance spread during performance test I for the ELP camera.

The above figures demonstrate that the measurements are consistent when taken during the same performance test. The figures below show that the measurements are also consistent when taken at different times. For this process the See3CAM was placed in the performance test setup and measurements were taken (only one of each type of measurement). The camera was then removed from the setup and the light turned off. The See3CAM was then again placed in the performance test setup and measurements were again taken. The same was done with the ELP camera.

Figure D.10 shows the color difference measured during these tests for the See3CAM compared against the reference value. This reference value was set against the value obtained during performance test I (the analysis of this test was redone after the first performance test). The real values are not relevant since camera settings changed during this test and performance test I.

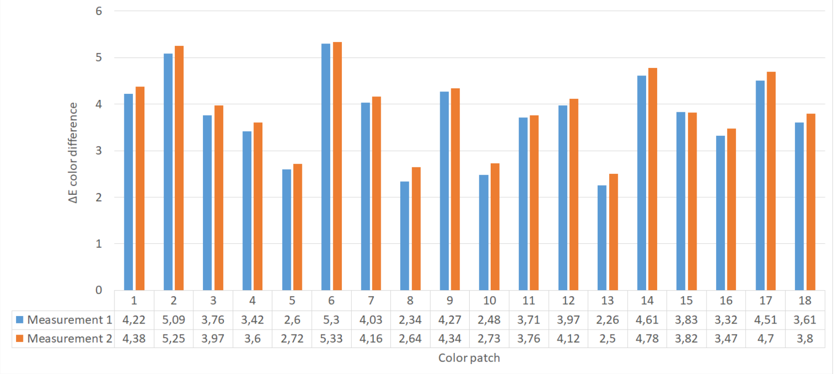

Figure D.10: ΔE color difference showing two separate measurements of the See3CAM compared to the color of the performance test 1.

The figures D.11 and D.12 show the full well capacity and signal to noise ratio respectively measured with the See3CAM at two separate occasions. They demonstrate that the measurements are consistent even when taken not during the same measurement session.

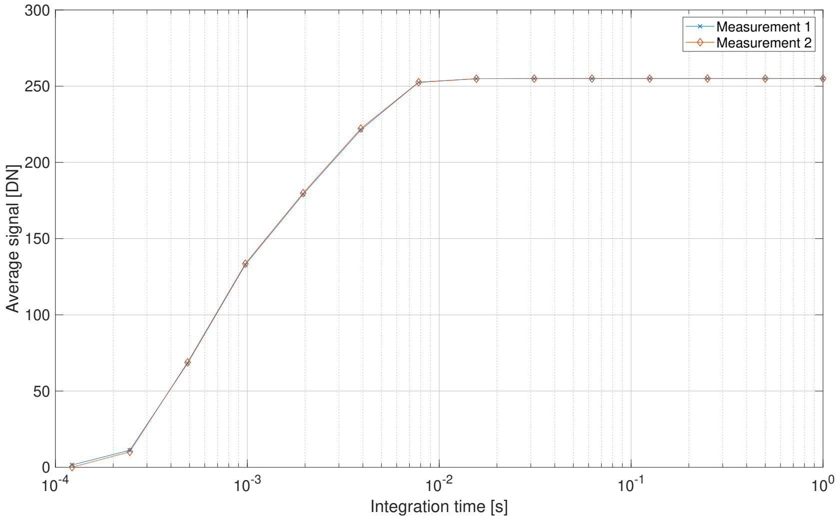

Figure D.11: Full well capacity of the See3CAM measured at two separate occasions.

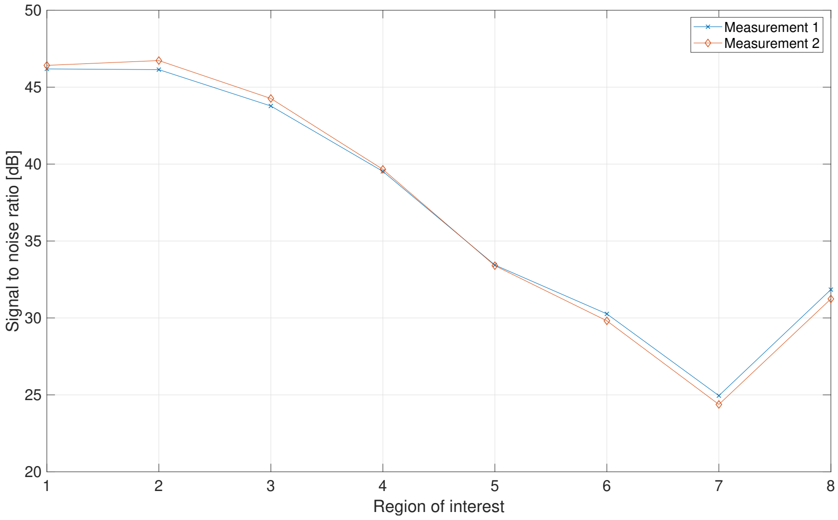

Figure D.12: Signal to noise ratios of the See3CAM measured at two separate occasions.

D.3. MTF Mapper verification

The standard ISO12233:2017 specifies a standard by which the spatial frequency response (which is in this case the same as the modulation transfer function) can be measured using the slanted edge method. The software used in this standard is, amongst others, a freely available MatLab script called sfrmat3 (information retrieved from ISO website) [51][52].

MTF Mapper was preferred over sfrmat3 because of its ability to automatically detect and process multiple slanted edges in an image. Verification of MTF Mapper was done by comparing its performance against that of sfrmat3 for two slanted edges with a known MTF. The figures D.13a and D.13b show the processed images. Figure D.13a contains little noise and Figure D.13b significant noise. This method of verification is based on [53].

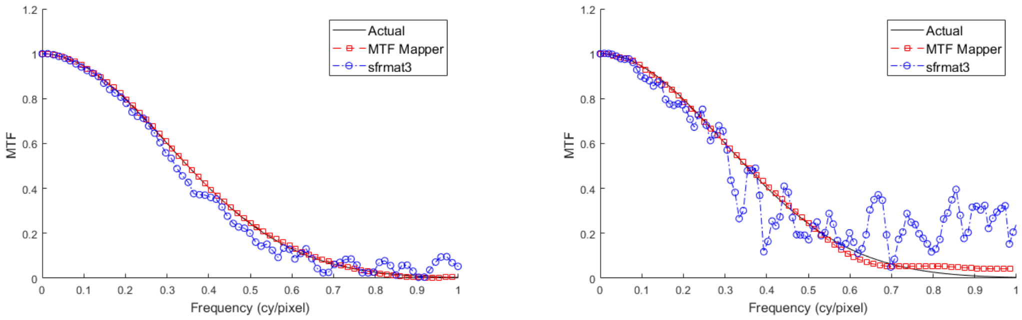

(a) Comparison of low noise performance of MTF Mapper and sfrmat3.

(b) Comparison of high noise performance of MTF Mapper and sfrmat3.

Figure D.14: Comparison of MTF Mapper and sfrmat3.

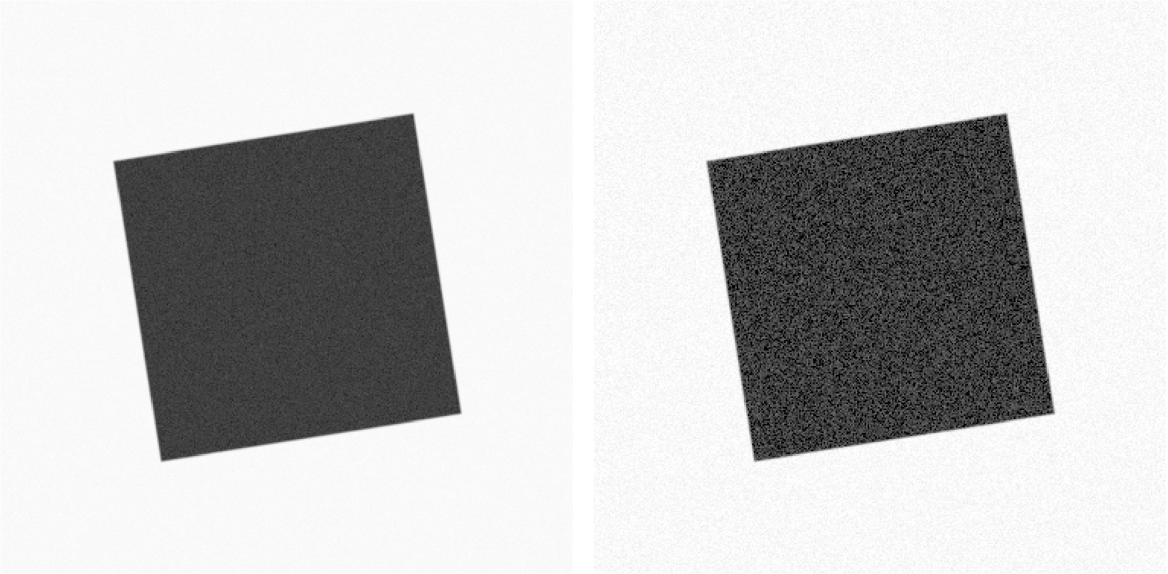

(a) Low noise rectangle for comparison between MTF Mapper and sfrmat3.

(b) High noise rectangle for comparison between MTF Mapper and sfrmat3.

Figure D.13: Rectangles used for MTF Mapper verification.

Figure D.14 shows the MTF as calculated by both methods for both the low- and high-noise cases.

Figure D.14 shows that MTF Mapper outperforms sfrmat3 in both the low noise case and especially in the high-noise case.

E

Supplementary figures

The analysis of this thesis contains well over 150 images. To keep this document at any reasonable length they cannot all be shown. Fortunately, a part of those images comes from data being measured thrice during each performance test. Appendix D has demonstrated that the performance test measurements are consistent making it not necessary to show all images. This appendix contains the images created during the performance tests which are not displayed in Chapter 6.

MTF charts

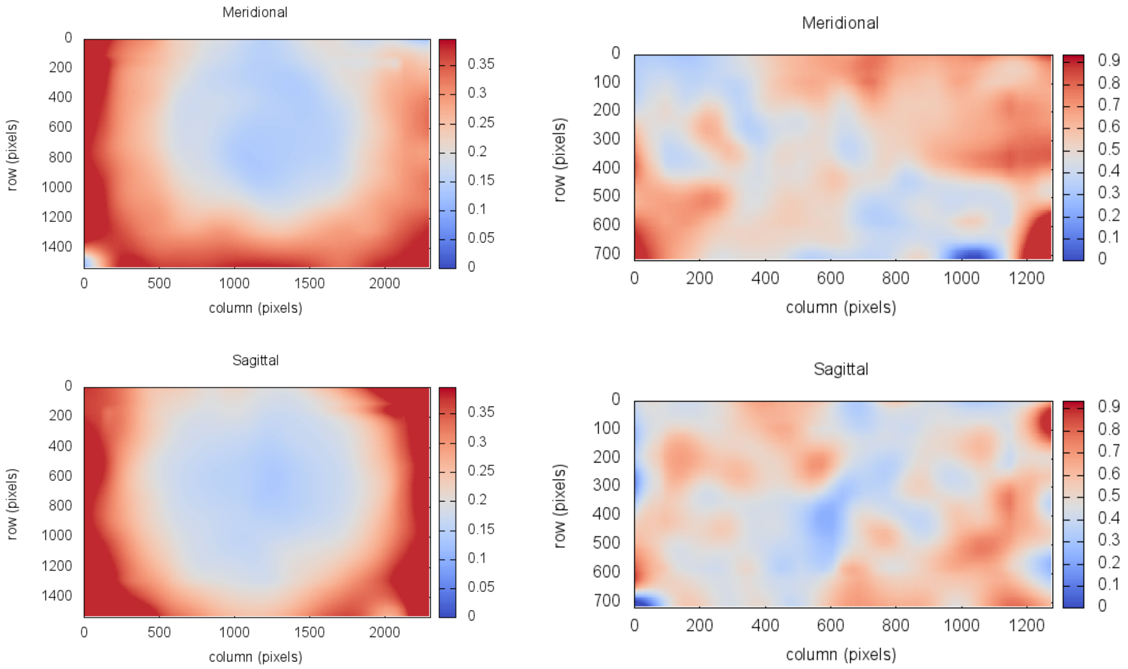

(a) MTF50 values of the See3CAM - Performance test I

(b) MTF50 values of the ELP - Performance test I

Figure E.1: MTF50 values captured during the first performance test

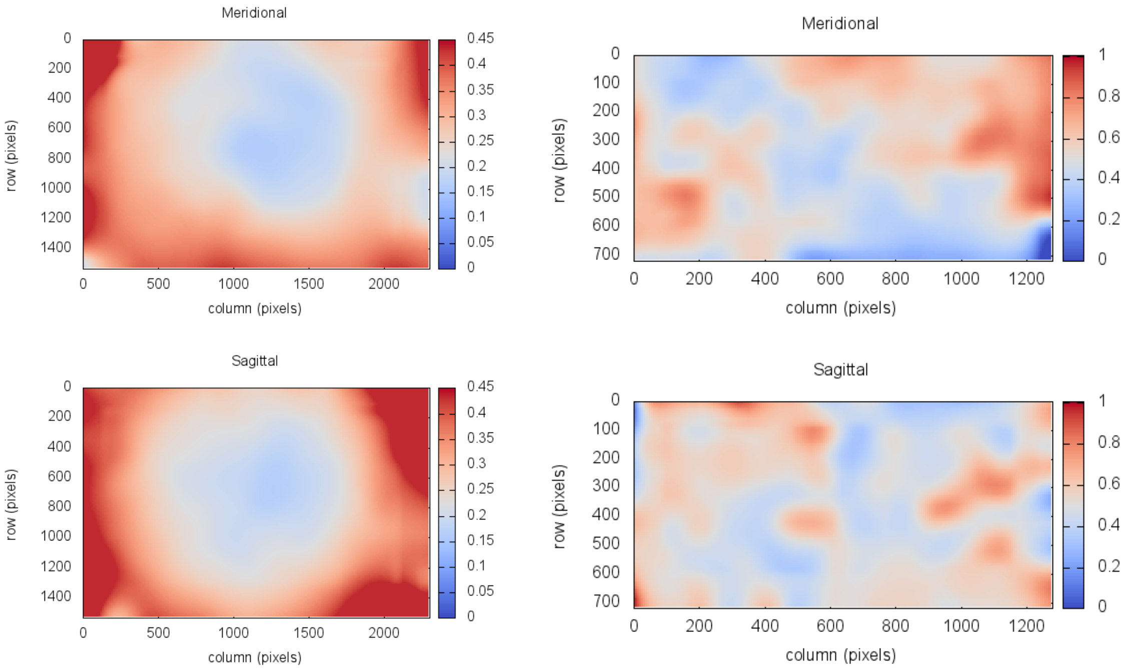

(a) MTF50 values of the See3CAM - Performance test II

(b) MTF50 values of the ELP - Performance test II

Figure E.2: MTF50 values captured during the second performance test

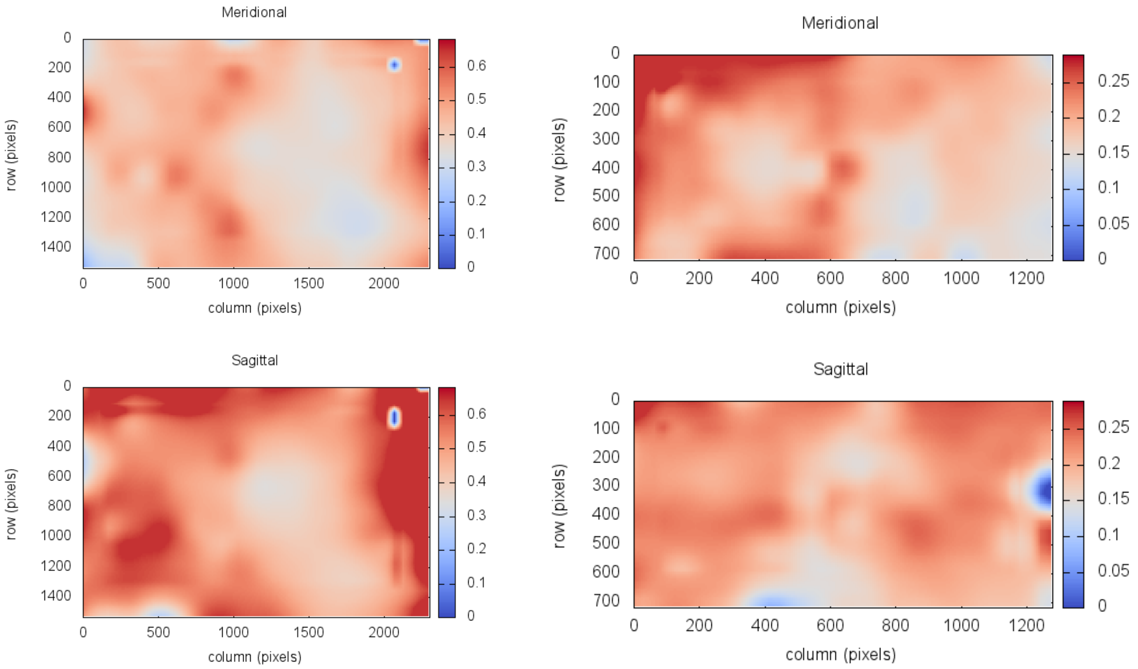

(a) MTF50 values of the See3CAM - Performance test III

(b) MTF50 values of the ELP - Performance test III

Figure E.3: MTF50 values captured during the third performance test

Edge spread functions

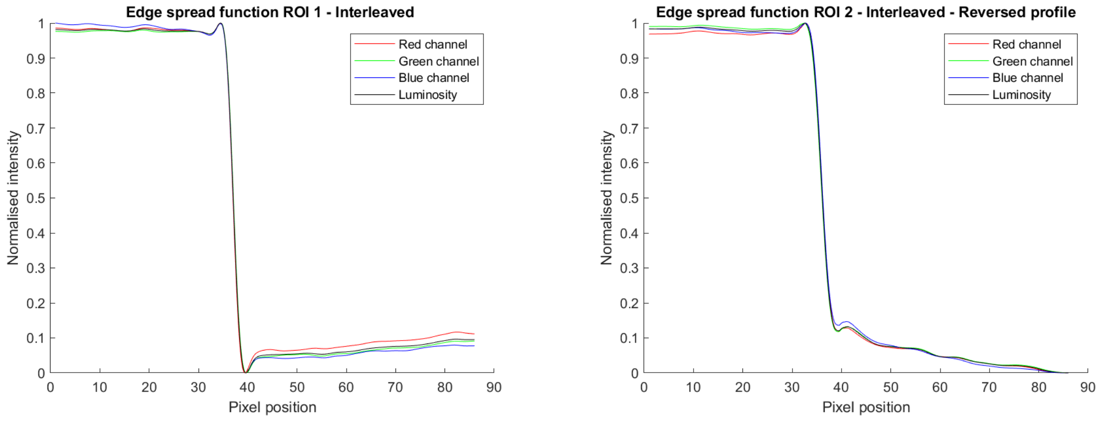

(a) ESF ROI 1 - See3CAM - Performance test I (b) ESF ROI 2 - See3CAM - Performance test I

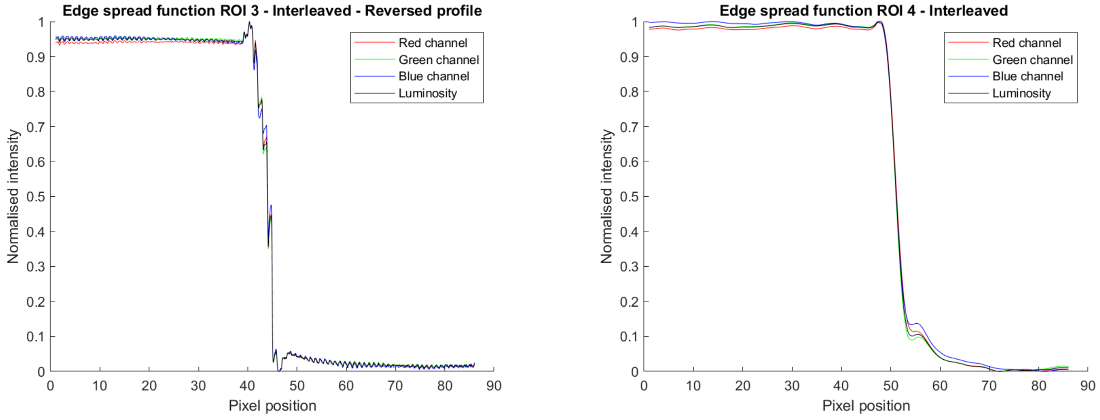

(c) ESF ROI 3 - See3CAM - Performance test I (d) ESF ROI 4 - See3CAM - Performance test I

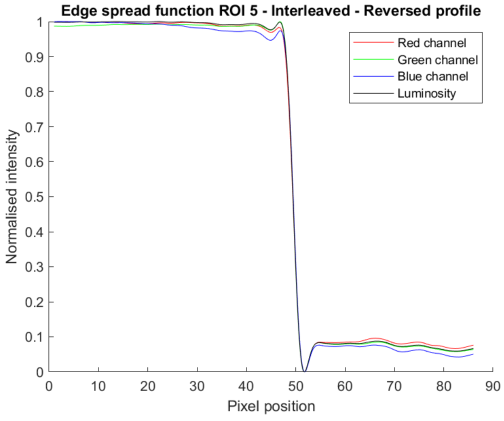

(e) ESF ROI 5 - See3CAM - Performance test I

Figure E.4: Edge spread functions of selected regions of interest (ROI) from the See3CAM - Performance test I

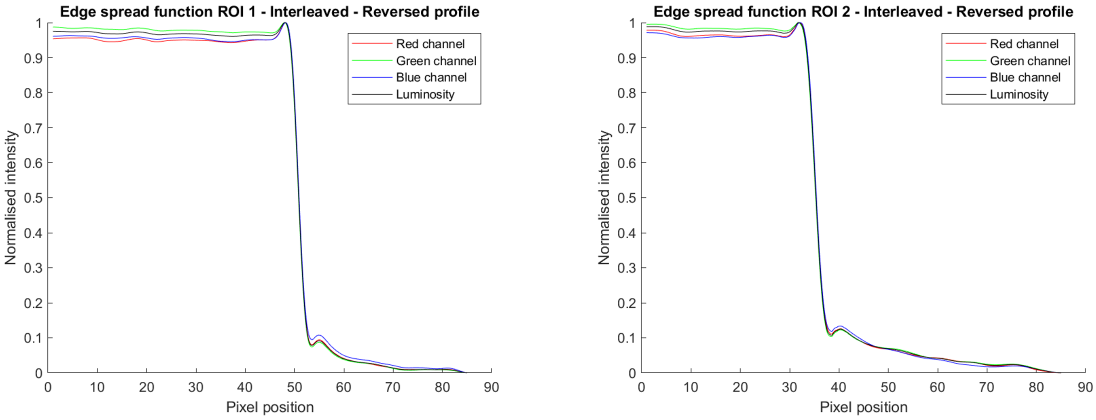

(a) ESF ROI 1 - See3CAM - Performance test II

(b) ESF ROI 2 - See3CAM - Performance test II

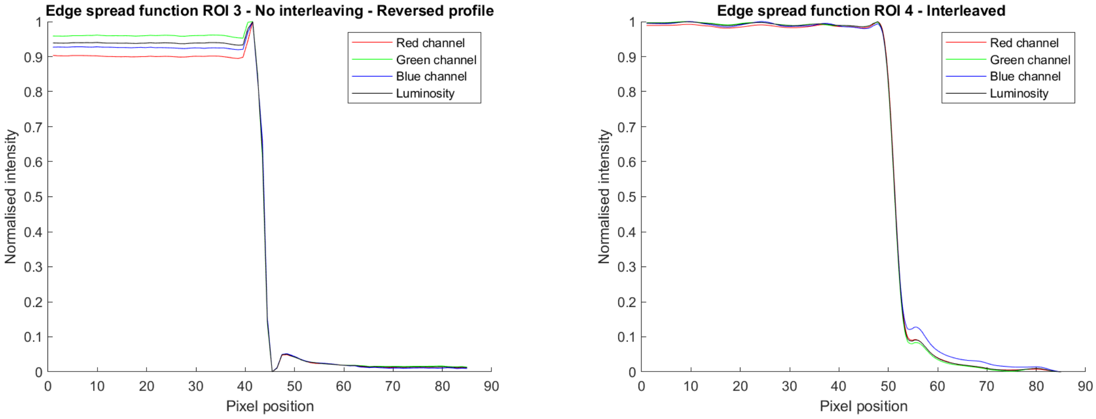

(c) ESF ROI 3 - See3CAM - Performance test II

(d) ESF ROI 4 - See3CAM - Performance test II

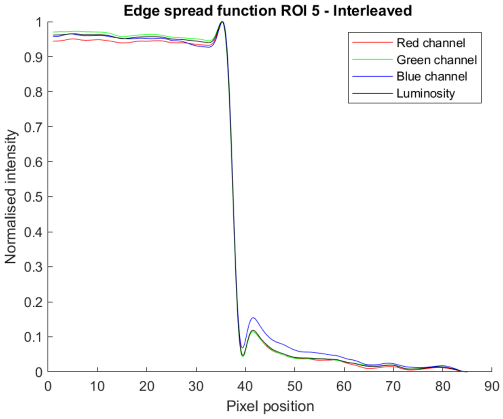

(e) ESF ROI 5 - See3CAM - Performance test II

Figure E.5: Edge spread functions of selected regions of interest (ROI) from the See3CAM - Performance test II

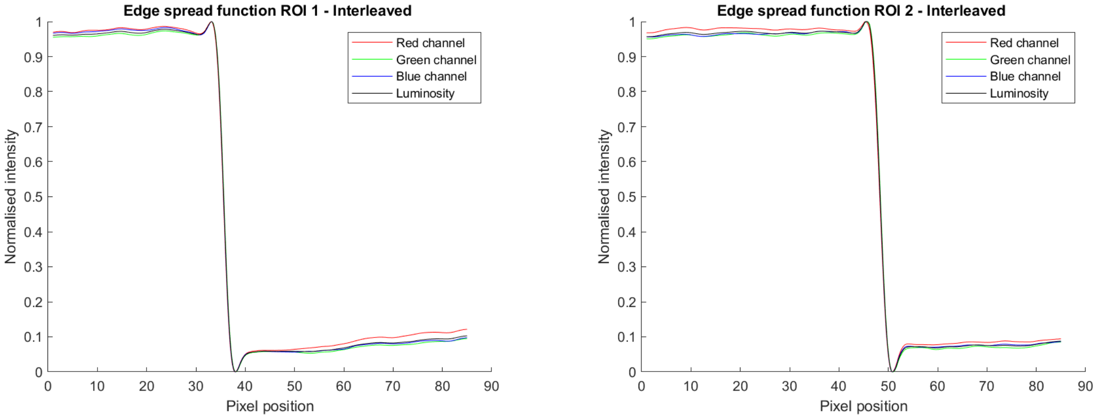

(a) ESF ROI 1 - See3CAM - Performance test III

(b) ESF ROI 2 - See3CAM - Performance test III

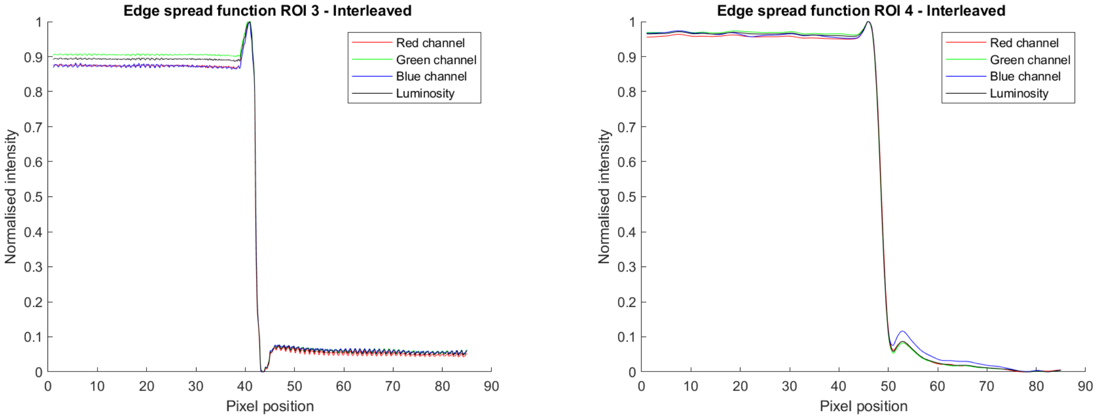

(c) ESF ROI 3 - See3CAM - Performance test III

(d) ESF ROI 4 - See3CAM - Performance test III

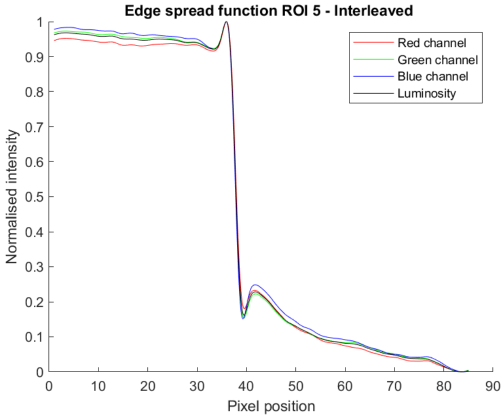

(e) ESF ROI 5 - See3CAM - Performance test III

Figure E.6: Edge spread functions of selected regions of interest (ROI) from the See3CAM - Performance test III

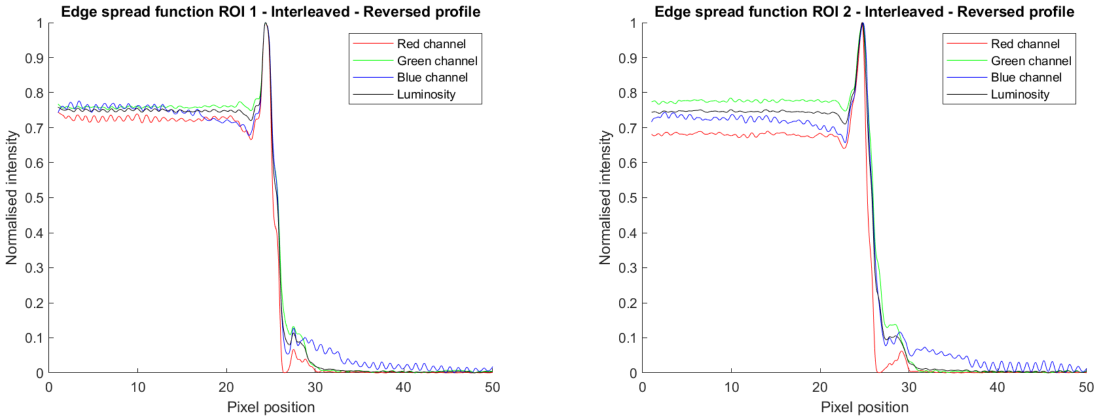
Edge spread function ROI 1 - Interleaved - Reversed profile

Edge spread function ROI 2 - Interleaved - Reversed profile

(a) ESF ROI 1 - ELP - Performance test I

(b) ESF ROI 2 - ELP - Performance test I

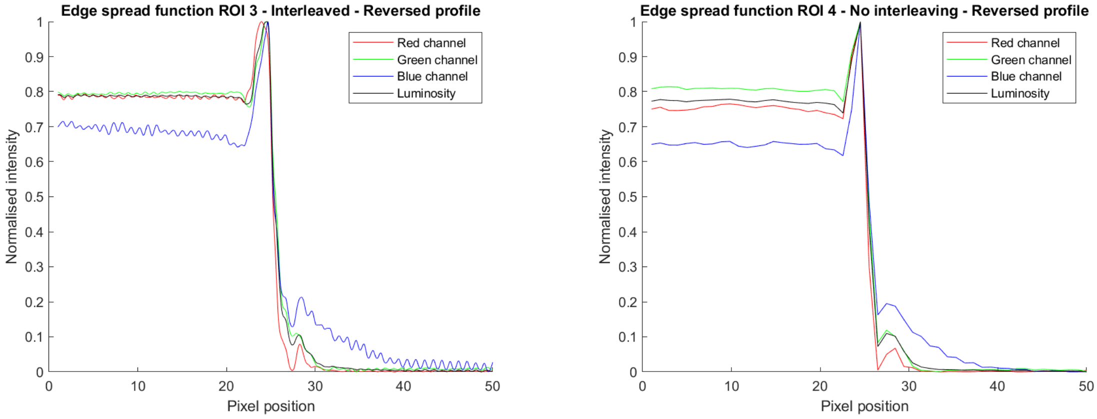
Edge spread function ROI 3 - Interleaved - Reversed profile

Edge spread function ROI 4 - No interleaving - Reversed profile

(c) ESF ROI 3 - ELP - Performance test I

(d) ESF ROI 4 - ELP - Performance test I

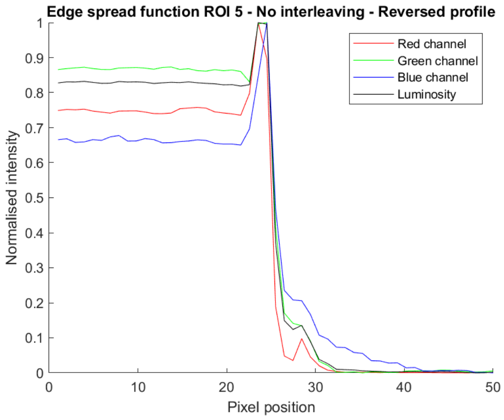
Edge spread function ROI 5 - No interleaving - Reversed profile

(e) ESF ROI 5 - ELP - Performance test I

Figure E.7: Edge spread functions of selected regions of interest (ROI) from the ELP - Performance test I

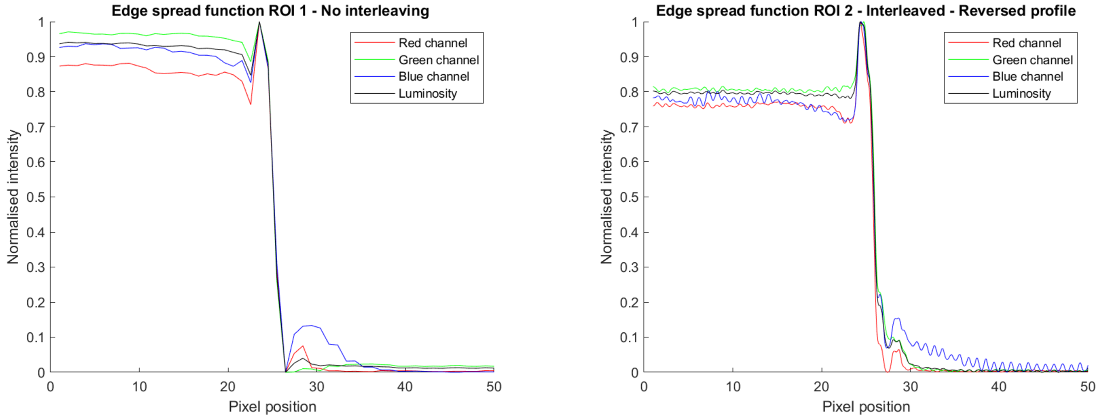

(a) ESF ROI 1 - ELP - Performance test II

(b) ESF ROI 2 - ELP - Performance test II

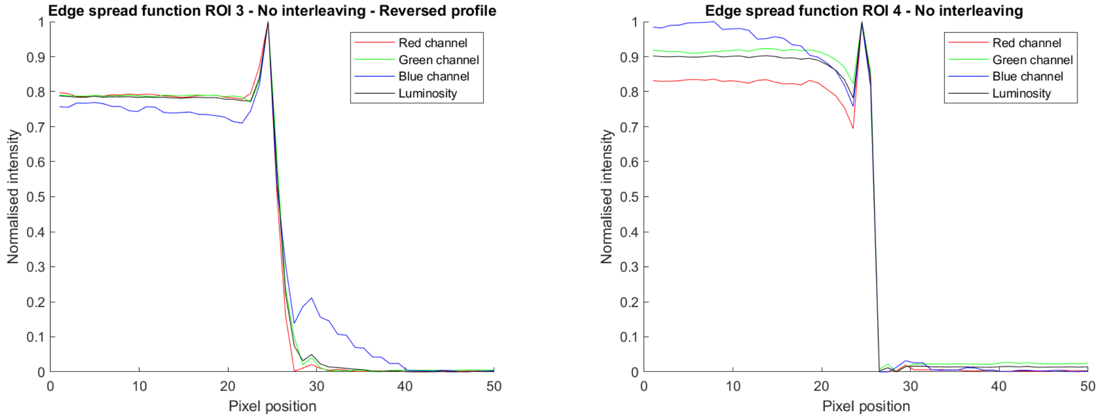

(c) ESF ROI 3 - ELP - Performance test II

(d) ESF ROI 4 - ELP - Performance test II

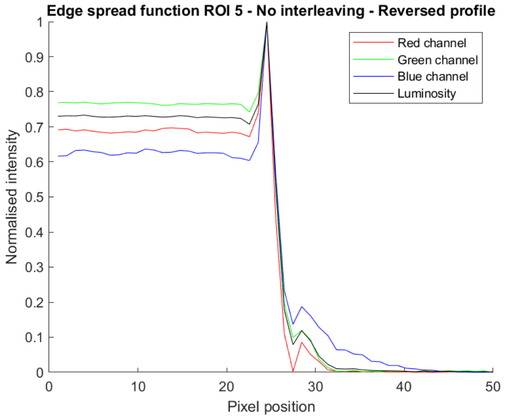

(e) ESF ROI 5 - ELP - Performance test II

Figure E.8: Edge spread functions of selected regions of interest (ROI) from the ELP - Performance test II

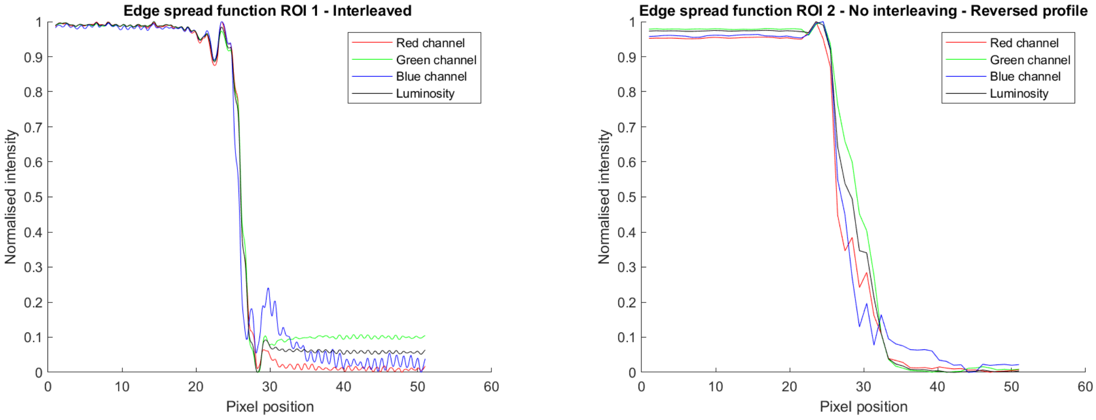

(a) ESF ROI 1 - ELP - Performance test III

(b) ESF ROI 2 - ELP - Performance test III

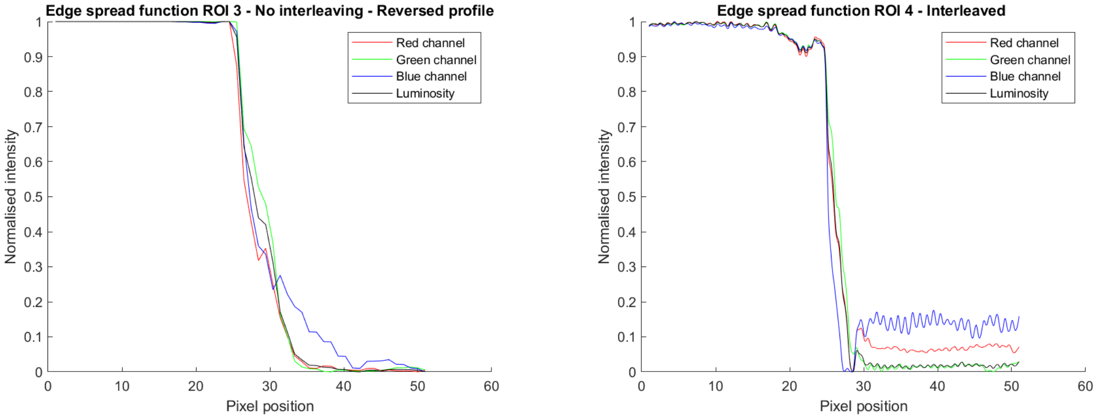

(c) ESF ROI 3 - ELP - Performance test III

(d) ESF ROI 4 - ELP - Performance test III

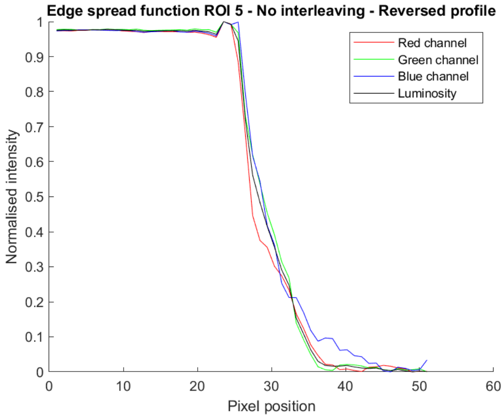

(e) ESF ROI 5 - ELP - Performance test III

Figure E.9: Edge spread functions of selected regions of interest (ROI) from the See3CAM - Performance test III